Technische Universität München

Fakultät für Medizin

Nuklearmedizinische Klinik und Poliklinik, Klinikum rechts der Isar

Establishment of *in vivo* imaging strategies for tracking of TCR-transgenic T cells

Nahid Yusufi

Vollständiger Abdruck der von der Fakultät für Medizin der Technischen Universität München zur Erlangung des akademischen Grades eines

Doktors der Naturwissenschaften (Dr. rer. nat.)

genehmigten Dissertation.

Vorsitzender:	Prof. Dr. Percy Knolle
Prüfer der Dissertation:	1. Prof. Dr. Markus Schwaiger
	2. Prof. Dr. Gabriele Multhoff
	3. Prof. Dr. Peter Bartenstein

Die Dissertation wurde am 14.03.2018 bei der Technischen Universität München eingereicht und durch die Fakultät für Medizin am 20.02.2019 angenommen.

TABLE OF CONTENT

FIGURE INDEX

TABLE INDEX

SUMMARY

Since T-cell based immunotherapy revealed promising clinical outcomes in the context of cancer treatment, for a better understanding of the efficacy and intravital behavior of the adoptively transferred T-cell receptor (TCR) transgenic T-cells sensitive and non-invasive monitoring technologies are required. To date, some approaches have been presented to monitor *in vivo* the distribution of gene-modified T cells. However, most technologies are accompanied by disadvantages in the practical application, being obstructing for a clinical translation. We developed a specific method to track *in vivo* engineered human T cells at the targeted tumor site by positron emission tomography (PET) using the Zirconium-89 radiolabeled F(ab')$_2$ fragment of the monoclonal anti-murine antibody (aTCRmu), which targets the murinized domain in the constant TCRβ chain of the introduced human TCR. We could perform further in-depth characterization studies regarding tracer quality for a potential clinical translation as well as sensitivity, image correlation and accuracy to *ex vivo* quantified T cells.

^{89}Zr-Df-aTCRmu-F(ab')$_2$ showed suitable properties in antigen affinity, immunoreactivity, influence on T-cell functionality and stability *in vitro* and *in vivo*. For assessing the sensitivity of this approach, local application of ^{89}Zr-Df-aTCRmu-F(ab')$_2$-labeled T cells in the animals showed specific signal detection to approximately 1.8 x 10^4 cells. This detection limit range was confirmed in the clinically relevant animal model, where different T-cell numbers and tracer were applied i.v. followed by PET imaging and *ex vivo* cell quantification. Even after different engraftment rates in several studies, the acquired PET images correlated well to the actual amount of T cells quantified *ex vivo*.

These findings confirm the high sensitivity and accuracy of our novel PET/CT T-cell tracking method and provide critical information about the quantity of transgenic T cells in the tumor environment suggesting this technology being highly suitable for clinical translation.

ZUSAMMENFASSUNG

Nachdem die T-Zell basierte Immuntherapie bei Krebserkrankungen bisher vielversprechende Ergebnisse in der klinischen Anwendung zeigte, sind für das verbesserte Verständnis der Wirksamkeit und dem intravitalen Verhalten der verabreichten T-Zell-Rezeptor (TZR) modifizierten T-Zellen sensitive und nicht-invasive Bildgebungsverfahren unerlässlich. Bis jetzt wurden einige Verfahren zur Bildgebung der Gen-modifizierten T-Zellen *in vivo* vorgestellt, jedoch sind viele dieser Anwendungen mit nachteiligen Eigenschaften in der praktischen Anwendung verbunden, welche eine klinische Translation erschweren. Wir haben eine Methode entwickelt, in der *in vivo* über Positron-Emissions-Tomographie (PET) humane modifizierte T-Zellen am anvisierten Tumor detektiert werden können unter Anwendung des Zirkonium-89 markiertem F(ab‘)$_2$-Fragments eines monoklonalen anti-murinen Antikörper, welches in der Lage ist die murine Sequenz in der TZRβ-Kette des eingeführten TZRs zu erkennen. Dadurch war es uns möglich weitere tiefgreifende Studien durchzuführen bezüglich der Tracer-Qualität für eine potenzielle klinische Anwendung, sowie zur Sensitivität, Genauigkeit und Korrelation der Bilder zu der quantifizierten T-Zellzahl *ex vivo*. ^{89}Zr-Df-aTCRmu-F(ab’)$_2$ wies gute Eigenschaften bezüglich Antigenaffinität, Immunoreaktivität, dem Einfluss auf T-Zell-Funktionalität und Stabilität *in vitro* und *in vitro* auf. Um die Sensitivität der Methode zu untersuchen, wurden ^{89}Zr-Df-aTCRmu-F(ab’)$_2$ markierte T-Zellen lokal in die Tiere appliziert und ergaben noch ein spezifisches Signal bei ungefähr 1.8×10^4 Zellen. Dieses Detektionslimit wurde in einem klinisch relevanten Tiermodell bestätigt, bei dem verschiedenen T-Zellkonzentrationen und der Tracer i.v. verabreicht wurden, gefolgt von PET-Bildgebung und *ex vivo* T-Zellquantifizierung. Selbst nach unterschiedlichen Engraftments in mehreren Studien korrelierten die PET-Bilder mit der tatsächlichen *ex vivo* quantifizierten T-Zellzahl. Diese Ergebnisse bestätigen die hohe Sensitivität und Genauigkeit dieses neuartigen PET/CT Zell-Tracking-Ansatzes und geben Aufschluss über die Quantität der im Tumormilieu befindlichen T-Zellen, was sehr für die Eignung einer klinischen Translation dieser Methode spricht.

1 INTRODUCTION

1.1 IMMUNOTHERAPY IN CANCER DISEASES

Cancer predominantly occurs in lung, liver, breast, stomach or colorectal tissues and is one of the major causes of death globally according to the world health organization (WHO) (Ferlay et al. 2015). For an effective treatment, adequate diagnosis and regimen are essential, which include conservative interventions, such as surgery, radiotherapy or chemotherapy. With the aid of existing therapies and early diagnosis some of the most common cancers, such as breast cancer, cervical cancer or oral cancer, display high curing rates (Steward 2014). However, many cancer entities remain difficult to treat with available techniques to achieve full recovery, or at least prolongation of the patient's life-span and improving quality of life.

The progressive growth of cancers originating from malignant single cell transformations is subjected to the immune system and its active survey for malignant transformations to induce recognition as "non-self" antigen and elimination (Beatty and Gladney 2015). The principle of the immune surveillance describing the role of the immune system controlling the development and outgrowth of transformed cells to cancer diseases has been already proposed in 1957 by Thomas and Burnet (Thomas 1982; Burnet 1970). Since then, the knowledge evolved, that cancer cells developed mechanisms to escape and suppress the immune system, facilitating tumor survival and progression by the failure of initiating and maintaining anti-tumoral immune response (Pinzon-Charry, Maxwell, and Lopez 2005; Schreiber, Old, and Smyth 2011; Blankenstein et al. 2012). This strategy of cancerous diseases also known as "tumor escape" include strategies, like tumor antigens being only weakly immunogenic or downregulating the antigen expression for evading recognition by the immune system. Furthermore, immune suppression by the tumors is conducted by the release of immunosuppressive cytokines, such as TGF-β and IL-10 or involving T cells with

immunosuppressive activities (i.e. regulatory T cells) (Sakaguchi et al. 2001; Khong and Restifo 2002).

The understanding of the dual effect of the immune system on emerging tumors prompted to develop innovative therapy approaches, where compounds of the immune system are manipulated to overcome the immune tolerance of tumors as summarized in Figure 1.

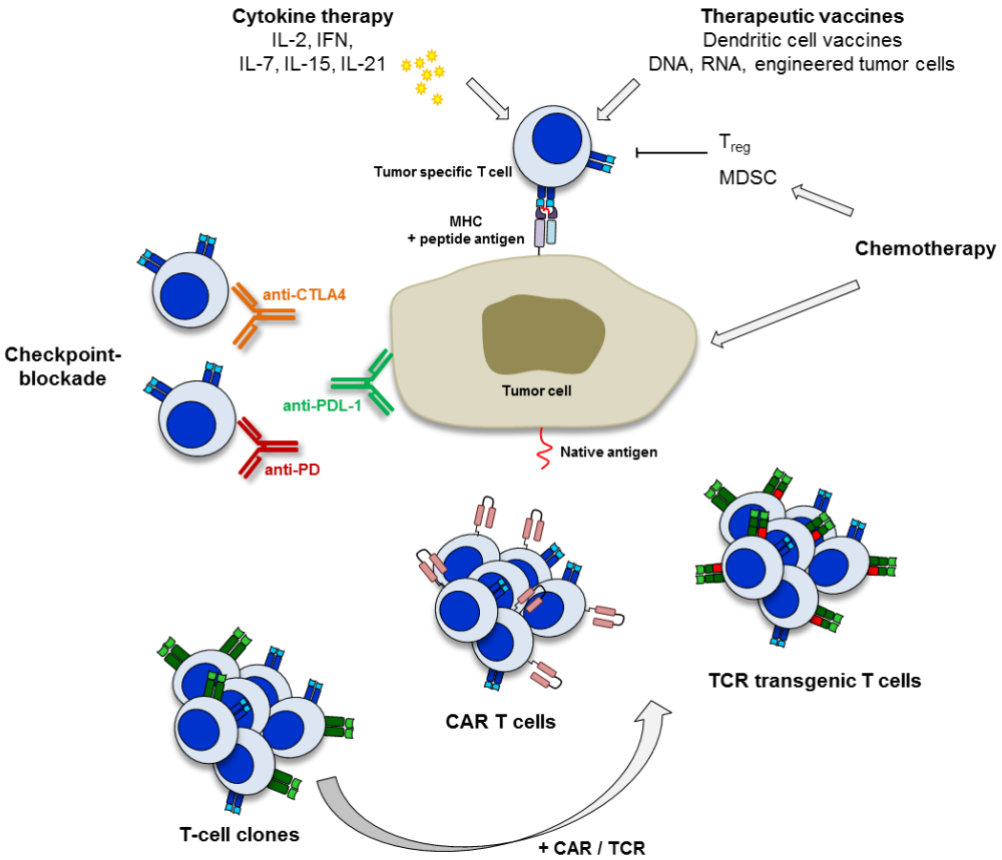

Figure 1. Therapeutic strategies to overcome immune tolerance of tumors.

Native T-cell responses to tumors can be boosted using cytokines and therapeutic vaccines. Chemotherapeutical treatment can reduce the impact of immunosuppressive cells, such as T_{reg} or myeloid-derived suppressor cells (MDSC) and has an additional effect on the tumor cell itself. Antibodies directed against negative regulatory receptors, such as cytotoxic T-lymphocyte antigen-4 (CTLA-4), anti-programmed cell death 1 protein (PD-1) or its ligand PD-L1, block inhibitory signals on natural T-cell responses to tumors. Tumor antigens can be targeted directly via adoptive T-cell transfer of transgenic T cells deriving from expanded T-cell clones, which are modified by chimeric antigen receptors (CARs) or tumor antigen specific T-cell receptors (TCRs) [modified from Maus et al., 2014 (Maus et al. 2014)].

1.2. T-CELL IMMUNOTHERAPY

Particularly therapeutic strategies involving adoptive T-cell transfer got the last years in intensive focus, as T cells are the final effectors in the immune-mediated cancer regression resulting in development of strategies using tumor-directed T cells (Rosenberg and Restifo 2015). During adoptive T-cell transfer, tumor-specific T cells are expanded *in vitro* and reinfused in large numbers into the cancer patient. For that approach either natural host cells or genetically engineered T cells modified with anti-tumor T-cell receptors (TCRs) or chimeric antigen receptors (CARs) can be used (Restifo, Dudley, and Rosenberg 2012).

Early experiences with adoptive T-cell transfer were made using autologous tumor infiltrating lymphocytes (TILs) from patients with metastatic melanoma (Rosenberg et al. 1988). Since then they could show in various studies objective cancer regression after infusion of *in vitro* expanded autologous TILs and increased survival of melanoma patients (Rosenberg et al. 2011; Dudley et al. 2010; Dudley et al. 2008). However, the efficacy of natural occurring TILs seems to be restricted to melanoma cancer diseases for reasons, which are not fully understood and due to the fact, that other tumors, such as those occurring in breast or colon tissues, contain T cells with unclear functions and specificities (Restifo, Dudley, and Rosenberg 2012; Ogino et al. 2011; Ruffell et al. 2012). This prompted to develop adoptive T-cell therapies using T-cell populations, which are genetically engineered to specific receptor expression against different tumor entities. This approach helps to broaden possibilities to direct tumors, while overcoming the limitations associated with the immune tolerance of the tumors.

1.2.1 CAR and TCR transgenic T cells

One possibility to conduct this approach is the modification by chimeric antigen receptor (CARs), combining antibody-like recognition with T-cell activating function (Maher 2012). The extracellular portions of these receptors consist of single chain variable fragments deriving

from antibody heavy and light chain variable domains combined with a transmembrane activation domain and are targeting surface antigens in an MHC-independent manner, unlike for T cell receptors. Clinical trials with promising efficacy using CAR-transgenic T cells were performed mainly in cases of B-cell malignancies by targeting CD19 and CD20 (Porter et al. 2011; Kochenderfer et al. 2012; Kalos et al. 2011; Lee et al. 2015; Maude et al. 2014). Furthermore, several studies were additionally performed on other hematologic malignancies and solid tumors in various tissues (Fesnak, June, and Levine 2016). However, this approach hasn't been effective for solid tumors so far (Kakarla and Gottschalk 2014; Park et al. 2007; Lamers et al. 2013), being the cause of the local immunosuppressive environment observed in many solid tumors and likely due to suboptimal signaling domains within the CAR construct (Harris and Kranz 2016; Rabinovich, Gabrilovich, and Sotomayor 2007).

In contrast, clinical trials using tumor-directed T-cell receptor transgenic T cells (TCR T cells) showed promising outcomes in both hematological malignancies and solid tumors. The targeted peptides mainly derive from extracellular and intracellular antigens being a marked advantage for the antigen selection. Particularly TCR-transgenic T cells targeting the antigens gp100, MAGE-A3, NY-ESO1 and MART-1 in melanoma as well as sarcoma associated diseases showed positive clinical responses (Morgan et al. 2006; Johnson et al. 2009; Robbins et al. 2015; Chapuis et al. 2013; Morgan et al. 2013).

A crucial factor for the success of adoptive transfer of transgenic T cells is also the differentiation state of the T-cell population used for the introduction of tumor-specific receptors (Sallusto and Lanzavecchia 2011). In general, CD8+ T cells pass a pathway of differentiation from naïve T cells (T_N) into central memory T cells (T_{CM}) and effector memory T-cell (T_{EM}) populations (Gattinoni et al. 2011; Gattinoni et al. 2006; Klebanoff, Gattinoni, and Restifo 2006). Ideally the transferred T-cell population should engraft and traffic to their cognate tumor site, proliferate and differentiate to memory and effector cells, actively eradicate tumor cells and persist for further immune surveillance. Although T_{EM} are associated with immediate cytolytic activity and cytokine production, however T_{CM} cells show

increased anti-tumor activity compared with T_{EM} within the memory cell pool as shown in studies in mice, primates and humanized mouse models (Klebanoff et al. 2004; Klebanoff, Gattinoni, et al. 2005; Berger et al. 2008; Wang et al. 2011). A focus on the less differentiated T-cell subset of T memory stem cells (T_{SCM}) revealed recently their resemblance to the naïve T-cell subset, but also a superior anti-tumoral activity, effective proliferation and potential of long persistence in humans, being promising for future studies in combination with tumor-specific CAR or TCR receptors (Biasco et al. 2015; Klebanoff, Gattinoni, and Restifo 2012; Gattinoni et al. 2009).

1.2.2 Efficacy and safety influencing factors of therapies based on adoptive T-cell transfer

After transferring genetically modified T cells, in clinical responses variabilities in effectiveness and toxicity have been observed, which can depend from various factors. The efficacy of such a treatment is related mostly to the extent of T-cell survival and persistence, which was described in reports, where particularly patients with complete response or prolonged survival displayed greater T-cell survival and persistence (Pule et al. 2008; Rosenberg et al. 2011; Tawara et al. 2017; Robbins et al. 2004). Engraftment and persistence of the transferred T cells can be influenced by pre-conditioning regimes, such as prior radiation or chemotherapy with fludarabine or cyclophosphamide (Dudley et al. 2008; Klebanoff, Khong, et al. 2005; Uttenthal et al. 2012). The resulting depletion of circulating T cells is supposed to promote *in vivo* expansion of the introduced transgenic T cells by preventing competition for cytokines and reduces the number of regulatory T cells (T_{reg}), which are in case of presence involved in the inhibition of the anti-tumoral effect of transgene T cells (Paulos et al. 2007; Gattinoni et al. 2005; Schmitt, Ragnarsson, and Greenberg 2009).

As “living drug” doses of transgenic T cells engraft and expand after the transfer *in vivo*, however the extent of these procedures are individual in all patients, thus the number of

administered cells is not predictive for the actual amount of effector and persistent cells and doesn't seem to correlate to defined clinical outcomes (Davila and Brentjens 2013). This remains dependent at least from conditioning regimes, the volume of tumor burden, the engineered T-cell population and the patient himself. Although the initial administered cell dose is less revealing, clinical studies with complete responses and cell persistence for longer than 6 month of anti-CD19 CAR T-cells, indicate the more important role of cell proliferation and persistence (Kalos et al. 2011; Porter et al. 2011).

Despite of the promising results in clinical trials using CAR and TCR engineered T cells for adoptive T cell therapy, potential safety risks are related to this therapy method. Activities described as "on-target, off-tumor" or "off-target, off-tumor" toxicities and cytokine release syndrome (CRS) have been observed in past clinical trials (Casucci et al. 2015). "On-target, off-tumor" toxicities are resulting from expression of the targeted tumor-associated antigen in healthy tissues. For instance, this effect was observed in a study using T cells expressing MART-1 directed TCRs, destructing melanocyte rich tissues, such as skin, eyes and in the inner ear (Johnson et al. 2009). In another trial the application of carcinoembryonic antigen (CEA) targeting TCR transgenic T cells resulted in transient severe and inflammatory colitis, which was related to reactivity of the T cells to the colonic mucosa expressing CEA (Parkhurst et al. 2011). Also in study cases with CAR transgenic T cells "on-target, off-tumor" activities were reported, as for the trial using CAR T cells targeting carboxy-anhydrase-IX (CAIX) in metastatic renal cell carcinoma, where cholestasis occurred in patients due to CAIX expression around the bile ducts and resulting T-cell infiltration (Lamers et al. 2006). Clinical therapy attempts with CD19 directed CAR-T cells for acute lymphoid leukemia showed this type of toxicity in continuous depletion of normal B cells, however this has been successfully manageable by gamma-globulin replacement (Brentjens et al. 2013; Grupp et al. 2013). However, in trials involving CD19 directed CAR-T cells the more severe and unpredictable cytokine release syndrome was observed, which are manifested as rapid immune reaction driven by an excessive release of inflammatory cytokines, such as INF-γ

and IL-6 (Brentjens et al. 2011). Particularly the increased release of IL-6 is likely related to a macrophage activation syndrome (MAS), manifested by the life-threatening clinical symptoms of fever, hypotension and haemophagocytic syndrome (Casucci et al. 2015). Interventions with positive effects to forestall the consequences of CRS are reported as the administration of the IL-6 receptor antagonist Tocilizumab and splitting the dose of CAR transgenic T cells over several days accompanied by strict monitoring of the patient (Ertl et al. 2011; Barrett, Teachey, and Grupp 2014; Teachey et al. 2013). Nevertheless, treatment and monitoring strategies need to be optimized or predictive biomarkers need to be evaluated as recently reported (Teachey et al. 2016), as CRS remains a significant matter for the safety of CAR T-cell treatment.

“Off-target, off-tumor” toxicities of TCR modified T cells are driven by cross-antigen recognition or generation of unpredicted specificities cross-reactivity arises from the ability of TCRs to recognize presented short epitopes, which likely resemble to antigens expressed in non-cancerious tissues. For instance, such activities have been observed in a study for melanoma and myeloma patients using HLA-A1-restricted and *ex vivo* affinity enhanced MAGE-A3 directed TCR transgenic T cells resulting in lethal cardiac toxicity in two cases, being related to the recognition of the HLA-A1 restricted peptide deriving from the contractile protein titin (Linette et al. 2013; Cameron et al. 2013). Despite lacking incidences in clinical trials, the risk of building unpredicted specificities by TCR-mispairing with native TCRs is present and has been demonstrated at least in a pre-clinical setting in mice (Bendle et al. 2010). This potential issue is proposed to be prevented for example by including codon optimization, introduction of disulfide bridges (S-S) between constant regions or introduction of a murine sequence in the constant region for preferred pairing of the introduced TCR chains (Cohen et al. 2006; Kuball et al. 2007; Scholten et al. 2006).

1.3 T-CELL IMAGING

Adoptive T-cell therapy provide until now promising outcomes in pre-clinical and clinical studies leading very likely to future drug approvals. However, the unpredictable and individual findings in terms of efficacy and safety prove that surveillance tools for measuring several factors, such as T-cell engraftment, proliferation, trafficking and final therapeutic outcome, are missing and urgently needed.

To date response to T cell-based therapies was determined by tumor growth and size a long period after completion of treatment. The response manifest either in a decrease in size, clinically stable disease, new or enlarging tumor not being associated with disease progression, but preceding a later decrease of tumor burden, or immune-mediated toxic effects, which may be misdiagnosed as non-treatment-related process leading to delayed appropriate clinical management (Hoos 2012; Wolchok et al. 2009). Due to these variations of responses and the need to improve treatment management, the therapeutic T cells require a real-time and prompt *in vivo* visualization after administration, particularly in form of clinically applicable non-invasive tracking methods for complementing conservative monitoring methods, such as blood sampling and invasive biopsies. In recent years, several approaches with different modalities evolved from the challenging demand to track non-invasively the presence, distribution, viability and quantity of therapeutic T cells. Therefore, techniques for the modalities optical imaging [Bioluminescence (BLI) and fluorescence imaging (FLI)], magnetic resonance imaging (MRI) and positron-emission tomography (PET) imaging are of particular interest and have inherent advantages and disadvantages regarding various aspects for the potential clinical application in T-cell based immunotherapy (table 1).

Sensitivity	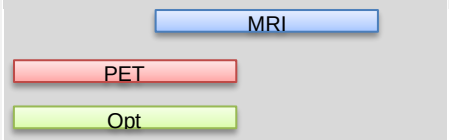	10^{-3} to 10^{-5} M 10^{-11} to 10^{-12} M 10^{-9} to 10^{-12} M (FLI); 10^{-15} to 10^{-17} M (BLI)
Tissue penetration	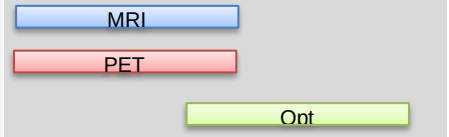	Unlimited Unlimited > 2 cm
Spatial resolution	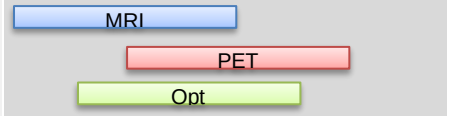	~ 1 mm (clinical), <0.1 mm (preclinical) ~ 5-10 mm (clinical), 1-2 mm (preclinical) ~ 2-5 mm
Potential for clinical tranlation	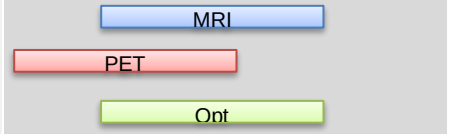	Yes Yes Limited for *in vivo* T-cell imaging [however fluorescence-guided surgery provides great advantages (Nguyen and Tsien 2013)]
Throughput (*in vitro*)	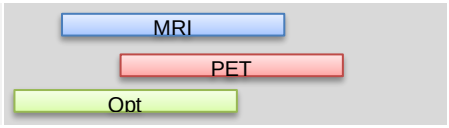	
Throughput (*in vivo*)	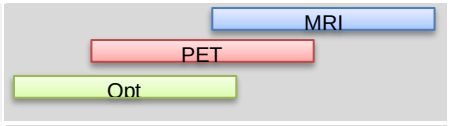	
Cost	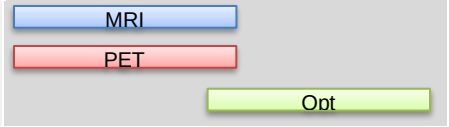	
		

Table 1. Characteristics of molecular imaging modalities for T-cell tracking.
Opt = optical imaging, including bioluminescence and fluorescence imaging [modified from Kircher et al., 2011 (Kircher, Gambhir, and Grimm 2011) and Liu and Li, 2014 (Liu and Li 2014)].

1.4 IN VIVO T-CELL IMAGING BY PET

So far, most approaches to evaluate immune responses were conducted in the clinic by PET or single-photon emission computed tomography (SPECT) (Hildebrandt and Gambhir 2004; Kircher, Gambhir, and Grimm 2011), while preclinical studies utilize beside of the adapted clinical modalities PET, SPECT and MRI also fluorescent and bioluminescence imaging. As

indicated in table 1, advantages of optical imaging techniques are their high sensitivities beneath picomolar ranges and their instant applicability in *in vitro* and preclinical *in vivo* studies to affordable conditions. Although several studies proved sensitive intravital T-cell imaging in animal models (Perez et al. 2015; Rabinovich et al. 2008; Mezzanotte et al. 2014; Charo et al. 2011; Prins et al. 2008; Chewning et al. 2009), the implementation of optical imaging remains reserved for small animal studies due to its poor tissue penetration representing the criterion of exclusion for clinical translation.

Imaging with MR is accompanied by exceptional spatial resolution, unlimited tissue penetration and a potential for clinical translation due to its extensive use in the clinic for tissue imaging. To date, most preclinical MRI studies on tracking T cells *in vivo* are based on direct cell labeling with modified superparamagnetic iron oxide nanoparticles (SPION) and imaging for various pathological conditions, such as brain ischemia, rheumatoid arthritis and in tumors (Chen et al. 2017; Li et al. 2016; Jin et al. 2016; Kircher et al. 2003; Leech et al. 2013). Also, the multi-modal application of PET/MR came into consideration by labeling CAR transgenic T cells with SPION-Copper-64, which has been however tested only in an *in vitro* B-cell lymphoma model (Bhatnagar et al. 2014). Furthermore, 19F-MRI after direct labeling with perfluorocarbon (PFC) or self-assembling nanocomplexes with ferumoxytol, heparin and protamine were employed for T-cell tracking *in vivo* (Gonzales et al. 2016; Hitchens et al. 2015; Thu et al. 2012). The studies resulted in promising images, particularly in combination with additional anatomical information. However, the tracking strategies are limited to pre-labeled T cells and do not take account of T cells deriving from proliferation, thus quantitative evaluation of MRI methods remains difficult.

Beside of the high sensitivity and unlimited tissue penetration, the greatest advantage of PET is that technologies developed preclinically can be applied directly to clinical situations, which allows quick translation of the methods (Phelps 2000). Monitoring immune responses and T-cells in the context of immunotherapy were conducted so far by different approaches using

PET, such as direct labeling of immune cells with radionuclides, reporter-gene imaging, using radioactive metabolite probes and immuno-PET.

1.4.1 Direct radiolabeling of T cells for tracking in vivo

One of the earliest approaches to visualize leukocytes by scintigraphy was to radiolabel the cells *ex vivo* with gamma-emitting radionuclides, such as ^{99m}Tc or ^{111}In, to visualize them after infusion in the context of infections and inflammations (Peters 1994; Roddie et al. 1988; Hughes 2003; Datz 1994). This approach was broadened to PET compatible radionuclides, particularly F-18, Cu-64 and Zr-89, as some clinical applications required the enhanced sensitivity and resolutions of clinical PET scanners (Rahmim and Zaidi 2008). The *ex vivo* radiolabeling methods were applied for various immune cells for different purposes *in vivo* and are summarized with their advantages or limitations in table 2. However, the major drawback of this method for tracking immune cells *in vivo*, is that longitudinal studies post transfer cannot be performed due to dilution of the related signal and that quantitative evaluations are not possible, as proliferating cells are not included in the imaging.

Labeling agent	Labeled cell type & Purpose	Advantage/ Limitation	Reference
^{99m}Tc-HMPAO	Leukocytes for infection and inflammation imaging	- still in clinical use - not suitable for detection of small cell numbers - low sensitivity of clinical SPECT	(Roddie et al. 1988) (Peters 1994) (Hughes 2003)
^{111}In-oxine	- Leukocytes for infection and inflammation imaging - Tumor-specific CTLs after adoptive transfer therapy - Tumor-specific CAR T cells	- reduced cell viability - low sensitivity and resolution of clinical SPECT	(Datz 1994) (Bhargava et al. 2009) (Hughes 2003) (Pittet et al. 2007) (Parente-Pereira et al. 2011)
^{18}F-FDG	Leukocytes for infection and inflammation imaging	- rapid efflux - low radiolabeling efficiency in cells with low glucose metabolism	(Botti et al. 1997) (Forstrom et al. 2000) (Bhargava et al. 2009)

		- too short half-life - reduced cell functionality and viability	
^{18}F-FBEM	T lymphocytes for tracking homing	- better labeling efficiency than ^{18}F-FDG - no impairment of T-cell functionality - too short half-life	(Lacroix et al. 2013)
^{64}Cu-PTSM	- Lymphocytes for tracking cell trafficking - OVA-Th1 cells for tracking cell trafficking	-longer cell-tracking periods due to longer half-life - no impairment of T-cell viability and proliferation - induction of increased DNA damage	(Adonai et al. 2002) (Griessinger et al. 2014)
^{89}Zr-Oxine **^{89}Zr-DBN** **^{89}Zr/^{64}Cu-chitosan nanoparticles**	- CTLs, NK cells, DCs, - Leukocytes	- high retention efficiency - high efflux rates (esp. in NK cells) - reduced cell viability - released ^{89}Zr accumulates in the bone	(Charoenphun et al. 2015) (Sato et al. 2015) (Bansal et al. 2015) (Fairclough et al. 2016)

Table 2. Approaches for direct radiolabeling of immune cells for imaging *in vivo* by SPECT/ PET.

1.4.2 Small molecule metabolite probes

PET probes based on metabolite substrates, being modified with radionuclides, such as F-18, are already widely used in the clinic. Among other small molecule drugs, these probes include mostly analogs of glucose, nucleosides or amino acids, which are accumulating after injection at increased levels in tissues, where metabolic activity is elevated compared to other tissues (Serdons, Verbruggen, and Bormans 2009). Applications and experiences with probes used for the detection of immune-cell accumulation *in vivo* are summarized in table 3. The major limitation of metabolite PET probes for imaging T cells in the tumor environment is, that most tumor cells show enhanced metabolic activity, resulting in simultaneous probe uptake, which makes the evaluation of immune cell infiltration difficult (Gambhir 2002). Furthermore, the uptake of the probes is not restricted only to T cells and not all T cells bear the same metabolic demands, which are dependent for instance from their location or differentiation and activation state.

Probe	Application type	Advantage/ Limitation	Reference
^{18}F-FDG	Glucose analog for measuring enhanced glucose accumulation in inflammatory lesions, due to increased T-cell infiltration	- ^{18}F-FDG already in clinical use and widely available - Restricted to inflammation imaging. Most tumors are highly glycolytic: difficulty to distinguish signals	(Radu et al. 2007) (Matsui et al. 2009) (Irmler et al. 2010)
^{18}F-FLT	Substrate analog for TK1 for measuring cell proliferation *in vivo*	- Difficult to distinguish T-cell proliferation from other cells - high endogenous thymidine amount in humans may hamper sensitivity - suitable for measurements of hematopoietic tissues, but not for tumor tissues (see ^{18}F-FDG)	(Wagner et al. 2003) (Ribas et al. 2010)
^{18}F-FAC	Analog for dCK (enzyme in nucleoside salvage pathway, highly expressed in activated lymphocytes)	- more specific than ^{18}F-FDG/-FLT - poor discrimination from tumor-infiltrating T-cells	(Radu et al. 2008) (Toy et al. 2010) (Nair-Gill et al. 2010) (Antonios et al. 2017)

Table 3. Metabolite analogs as PET probes for imaging T-cell infiltration and function *in vivo.*

1.4.3 Reporter gene imaging

A further strategy to track T cells *in vivo* is the introduction of reporter genes functioning as transporters or enzymes by the use of their radioactive probes (Herschman 2004). In comparison to direct labeling and the use of metabolic probes the expression of PET reporter genes overcome challenges regarding long-run imaging studies of expanding cells and accuracy, as probes are actively transported and accumulated in every functional and living cell. To date, most studies are conducted by the reporter gene herpes simplex virus thymidine kinase 1 (HSV1-tk), which has been also translated into clinical use (Yaghoubi et al. 2009). Table 4 summarizes all reporter genes used for T-cell imaging so far, particularly in the context of adoptive transfer *in vivo*, and points out advantages and limitations of the systems. The major disadvantage of this approach is the genetic modification of the cells, additionally to the insertion of tumor-specific TCRs or CARs, bearing the risk of immunogenicity from the expression of the foreign protein, which originates from virus particles (Berger et al. 2006; Traversari et al. 2007). Using reporter genes deriving from the

human system, such as the human sodium iodine symporter (hNIS), human norepinephrine transporter (hNET) or the human deoxycytidine kinase triple mutant (hdCK3mut), immunogenicity can be prevented, however non-specific signals may be related due to expression in other tissues.

Reporter gene	Modified cell type & purpose	Advantage/ Limitation	Reference
HSV1-tk	T lymphocytes TCR transgenic T cells/ CTLs/ hematopoietic stem cells (HSC) after adoptive transfer	- additional safety feature as suicide gene - experience in the clinic - immunogenic - risk of insertional mutagenesis	(Koehne et al. 2003) (Dubey et al. 2003) (Dobrenkov et al. 2008) (Shu et al. 2009) (Vatakis et al. 2011) (Gschweng et al. 2014)
hNIS	T cells after s.c. injection	- human origin, non-immunogenic - gene expression in other tissues resulting in background signals - non-specific uptake of reporter probes resulting in background signals - mutant variants of reporter genes bear risk of immunogenicity - risk of insertional mutagenesis	(Moroz et al. 2015)
hNET	(EBV-specific) T cells after adoptive transfer or s.c. injection		(Doubrovin et al. 2007) (Moroz et al. 2015)
hdCKDM	CAR transgenic T cells TCR transgenic HSCs and PBMCs after adoptive transfer		(Likar et al. 2010) (McCracken et al. 2013) (McCracken et al. 2015)

Table 4. Reporter genes inserted in immune cells and used for PET imaging *in vivo*.

1.4.4 Immuno-PET

A further method for *in vivo* T-cell detection is the targeting of T-cell epitopes by radiolabeled biomolecules, particularly antibody derived vectors. This approach is based on the strategy applied in radioimmunotherapy (RIT), where radiolabeled antibodies are used for cytotoxic radiation of the target cell, which has proven successfully in the clinic (Milenic, Brady, and Brechbiel 2004). The validated use of antibodies for targeting cell epitopes *in vivo* led to the utilization for the diagnostic purpose as surrogate markers in PET. The advantage of this technique compared to reporter gene imaging is the avoidance of further genetic manipulation of the T cells, being a crucial factor for the clinical translation due to technical

and regulatory terms. With advances in the field of antibody engineering, availability of various radionuclides and PET devices in preclinic and clinic, the translational potential of this approach is promising and yielded in the last years first approaches towards T-cell imaging in the context of immunotherapy. Table 5 describes studies conducted with different radiotracer types for T-cell imaging in the preclinical setting so far. By developing protein-based radiotracer, in the first place T-cell targeting whole antibodies can be used as shown in the studies of Griessinger et al. (Griessinger et al. 2015) and England et al. (England et al. 2017). Full antibodies are with about 150 kDa quite big in size, thus having a quite long plasma half-life, which requires positron-emitters with appropriate half-lives until image acquisition is performed. For this purpose longer-lived radionuclides, such as ^{64}Cu, ^{124}I and ^{89}Zr are good candidates and showed suitable properties in clinical immuno-PET (van Dongen et al. 2007). To overcome the delay time of several days between administration and imaging of full antibody based radiotracer due to their long plasma half-life, enzymatically generated or engineered antibody fragments represent valuable alternatives, as they are reduced in size, while specificity and affinity are retained (Wu 2014). For that, Fab and F(ab')$_2$ fragments (~50 and 110 kDa) come into question or engineered fragments, such as single chain variable fragments (scFv; ~25 kDa), minibodies (Mb, ~80 kDa) or diabodies (Db, ~50 kDa). The application of different biomolecules for targeting entails optimization procedures related to chelator and radionuclide selection based on half-life, as well as the evaluation of various characteristics *in vitro* and *in vivo*, among others like affinity, internalization, stability and impact on T-cell functionality before imaging data are further evaluated.

Radiotracer	Targeted cell type	Advantage/ Limitation	Reference
^{64}Cu-DOTA-mAb	TCR transgenic Th1 cells	- internalization of the radiotracer, low efflux rate - specific homing shown in two models - missing information about	(Griessinger et al. 2015)

		radiotracer quality *in vitro*/ *in vivo* - mAb is supposed to induce activation of the T cells - only direct labeling of the cells and no injection of the tracer - DSB expression and cell death at low activities and early time points - study refers only to murine T cells	
^{89}Zr-Df-mAb (Nivolumab)	PD-1 expressing T cells	- usage of humanized mouse model - low specific activity reported (0.018 µCi/µg) - imaging with high radiotracer activity doses (5-10 MBq) - high background signals and late optimal tumor contrast (168 h)	(England et al. 2017)
^{64}Cu-NOTA-minibody	CD8+ lymphocytes	- retained specificity, but low affinity - non-specific uptake in the liver due to trans-chelation of ^{64}Cu to enzymes - supposed aggregation/multimerization - study refers only to murine T cells	(Tavare et al. 2014)
^{89}Zr-Df-cys-diabody	CD8+ and CD4+ lymphocytes	- suitable radiotracer quality and retained affinity in nanomolar range - imaging at low activity dose in different immunotherapeutic models -aggregation/multimerization - Db decreases CD4 expression and cytokine release - dose dependent proliferation impairment of T cells - studies refer only to murine T cells	(Tavare et al. 2015) (Tavare et al. 2016) (Freise et al. 2017)

Table 5. Immuno-PET tracer used in preclinical studies for *in vivo* T-cell imaging.

2 AIM OF THIS STUDY

The adoptive transfer of tumor-directed T-cell receptor (TCR) transgenic T cells in the context of cancer immunotherapy is currently becoming an increasingly promising treatment option. TCR-transgenic T cells targeting tumor-associated antigens showed positive clinical outcomes, particularly in patients with melanoma and synovial sarcoma (Morgan et al. 2006; Johnson et al. 2009; Rapoport et al. 2015; Robbins et al. 2015). However various transgenic T cell based clinical trials revealed beside of the therapeutic response adverse effects resulting in few cases even in fatal events (Linette et al. 2013; Parkhurst et al. 2011; Morgan et al. 2013). On the one hand the understanding of the efficacy of T-cell based immunotherapy regarding T-cell behavior *in vivo* needs to be explored for further development and optimization of this therapeutic approach, on the other side the potential risk of this therapy requires monitoring tools for appropriate clinical surveillance. For these issues non-invasive *in vivo* imaging technologies for transgenic therapeutic T cells are required with the potential for customization and clinical implementation. In this study we aimed to establish a tracking method for TCR transgenic T cells using the PET modality and to characterize the used radiotracer for the *in vivo* application as well as the accuracy and sensitivity of this technique. The developed radiotracer was characterized for antigen affinity, immunoreactivity, influence on T-cell functionality and stability *in vitro* and *in vivo* as well as for its impact on T-cell function and viability. The evaluated radiotracer was applied in a clinical relevant animal model for proving specific recognition and tracking of the TCR transgenic T cells by PET. Furthermore, the developed technique was evaluated for its sensitivity regarding engrafted T-cell number and associated PET image. The gained data were evaluated in several studies for reliability and allowed first calculations of correlations of different parameters deriving from the animal imaging experiments in the presented model.

3 MATERIAL

3.1 TECHNICAL EQUIPMENT

Device	Company
8-channel pipette 30-300 µl	Eppendorf AG, Hamburg, Germany
Analytical balance 440-35N	Denver Instrument, Göttingen, Germany
Analytical balance AC210S	Sartorius, Göttingen, Germany
Analytical balance SI-64	Denver Instrument, Göttingen, Germany
Aperio AT2 scanner	Leica Biosystems, Nussloch, Germany
Axiovert 40C microscope	Carl Zeiss Microscopy, Oberkochen, Germany
Ball mill Micro-Dismembrator II	B. Braun, Melsungen, Germany
CelloShaker Variospeed	Chemetron, Milan, Italy
Centrifuge 5417R	Eppendorf AG, Hamburg, Germany
Centrifuge 5810R	Eppendorf AG, Hamburg, Germany
Centrifuge Biofuge 13	Heraeus, Hanau, Germany
Centrifuge J2-HS	Beckman Coulter, Brea, USA
Centrifuge Megafuge 1.0R	Heraeus, Hanau, Germany
Combitips 5/10 ml	Eppendorf AG, Hamburg, Germany
Cryotome CM1950	Leica Biosystems, Nussloch, Germany
DAKO Autostainer	Dako, Agilent Technologies, Glostrup, Denmark
Freezer (-20 °C)	Liebherr-International AG, Bulle, Switzerland
Freezer (-80 °C)	Buchner Labortechnik, Pfaffenhofen, Germany
Gamma counter 1480Wizard3	Wallac, PerkinElmer, Waltham, USA
Gamma counter 2480Wizard2	PerkinElmer, Waltham, USA
Gilson Pipette PIPETMAN Classic 0.2-2/ 1-10/20-100/200-1000 µl	Gilson, Middleton, Germany
Imaging plate scanner HDCR35 Bio	Dürr NDT, Bietigheim-Bissingen, Germany
Incubator BBD6220	Heraeus Holding, Hanau, Germany
Inveon small animal PET/CT scanner	Siemens, Knoxville, USA

Irradiation Cabinet	Gulmay, Byfleet, UK
Laminar Flow	BDK, Sonnenbühl-Genkigen, Germany
Laminar Flow HERAsafe	Heraeus Holding, Hanau, Germany
LC-20A Prominenc HPLC system	Shimadzu, Nakagyo-ku, Kyōto, Japan
LSRII cytometer	BD bioscience, Franklin Lakes, USA
MACS MultiStand	Miltenyi Biotec, Bergisch Gladbach, Germany
MACSmix Tube Rotator	Miltenyi Biotec, Bergisch Gladbach, Germany
Magnet agitator	Janke & Kunkel, Staufen, Germany
Magnetic stirrer and heater RCT basic	IKA, Staufen im Breisgau, Germany
Microplate reader (Sunrise)	Tecan, Männnedorf, Switzerland
Microscope BX53	Olympus, Tokio, Japan
MidiMACSTM Separator	Miltenyi Biotec, Bergisch Gladbach, Germany
Mini-PROTEAN® Tetra Vertical Electrophoresis Cell	Bio-Rad Laboratories, Hercules, USA
Nanophotometer	Implen GmbH, Munich, Germany
Neubauer Counting Chamber	Karl Hech, Sondheim/Röhn, Germany
Odyssey Infrared Imaging system	LI-COR Biosciences, Lincoln, USA
Pipetboy	INTEGRA Biosciences, Fernwald, Germany
Pipetus	Hirschmann, Eberstadt, Germany
Radio-TLC-scanner	Eckert & Ziegler, Berlin, Germany
Repeater pipette 4780	Eppendorf AG, Hamburg, Germany
Rotary microtome HM 325	Thermo Fischer Scientific, Waltham, USA
SE-HPLC BioSep™ (SEC-s3000 LC Column)	Phenomenex, Aschaffenburg, Germany
Shaking-hybridization oven OV3	Biometra, Göttingen, Germany
Single-channel pipettes 0.1-2.5/2-20/ 20-100/100-1000 µl	Eppendorf AG, Hamburg, Germany
Temperature control ETS-D4 fuzzy	IKA, Staufen im Breisgau, Germany
Thermomixer comfort	Eppendorf AG, Hamburg, Germany
Vortexer	Bender & Hobe, Switzerland
Vortexer Vibrofix VF1	IKA, Staufen im Breisgau, Germany

X-Ray cassette	Rego X-ray GmbH, Augsburg, Germany

Table 6. Technical equipment

3.2 CONSUMABLE SUPPLIES

Consumable	**Company**
50 ml/15 ml tube	BD bioscience, Franklin Lakes, USA
Polystyrene tubes 4.5 ml	Sarstedt, Nümbrecht, Germany
Aspiration pipette (2 ml)	Sarstedt, Nümbrecht, Germany
Cell culture flask	Greiner Bio-One, Frickenhausen, Germany
Cell culture treated 6/12/24/96 well plates	TPP Techno Plastic products, Trasadingen, Switzerland
Cell culture treated 96 well U-bottom plates	TPP Techno Plastic products, Trasadingen, Switzerland
Cell strainer (40 µm)	BD bioscience, Franklin Lakes, USA
Chromatography paper (iTLC-SA)	Agilent Technologies, Santa Clara, USA
CryoPure tube (1,6 ml)	Sarstedt, Nümbrecht, Germany
Filter tips (10 µl, 200 µl, 1000 µl)	Sarstedt, Nümbrecht, Germany
Freezing Container	Nunc, Roskilde, Denmark
Gloves latex	Sempermed, Wien, Austria
Gloves nitrile	KCL, Eichenzell, Germany
Gloves nitrile	Sempermed, Wien, Austria
ImmunoPlates	Nunc, Roskilde, Denmark
Inoculating loops	VWR, Darmstadt, Germany
MACS cell separation Columns (LD, LS, MS)	Miltenyi Biotec, Bergisch Gladbach, Germany
Microtubes (1.2 ml)	Alpha laboratories, Hampshire, UK
Non-treated 6/24/96 well F-bottom plates	Greiner Bio-One, Frickenhausen, Germany
Nunc MaxiSorp ELISA plate	Nunc, Roskilde, Denmark
Object slides SuperFrost Plus	Thermo Fischer Scientific, Waltham, USA
Parafilm	Pechiney Plastic Packaging, Chicago, USA
Phosphor imaging plate	Fujifilm, Tokyo, Japan
Pipette tips (10 µl, 200 µl, 1000 µl)	Sarstedt, Nümbrecht, Germany

Protein LoBind Tubes	Eppendorf AG, Hamburg, Germany
Reaction tubes (0.5 µl)	Peqlab Biotechnologie, Erlangen, Germany
Reaction tubes (1.5 µl and 2 ml)	Sarstedt, Nümbrecht, Germany
Round bottom flow cytometry tubes	BD bioscience, Franklin Lakes, USA
Sealing foil	Alpha laboratories, Hampshire, UK
Sephadex G-25 M, PD10 column	GE Healthcare, Buckinghamshire, UK
Serological pipettes (2/5/10/25/50 ml)	Sarstedt, Nümbrecht, Germany
Stericup 0,22 µm Vacuum Filter Units	Merck Millipore, Darmstadt, Germany
Sub-Q syringes (1 ml)	BD bioscience, Franklin Lakes, USA
Syringe filter (0.22 µm)	Merck, Darmstadt, Germany
Syringe filter (0.45 µm)	TPP Techno Plastic products, Trasadingen, Switzerland
Single-use syringes, Injekt-F 1 ml	B. Braun, Melsungen, Germany
Disposal hypodermic needles 26 G/30 G	B. Braun, Melsungen, Germany

Table 7. Consumable supplies

3.3 REAGENTS AND CHEMICALS

Reagent	**Company**
1,4 Dithiothreitol (DTT)	Sigma-Aldrich, Taufkirchen, Germany
10 % Neutral buffered formalin	Leica Biosystems, Nussloch, Germany
7-Aminoactinomycine D (7-AAD)	Sigma-Aldrich, Taufkirchen, Germany
AccuCheck Counting beads	Invitrogen, Carlsbad, USA
Agarose	Roth, Karlsruhe, Germany
AIM-V	Invitrogen, Carlsbad, USA
Ammonium persulfate (APS)	Sigma-Aldrich, Taufkirchen, Germany
Bovine serum albumine (BSA)	Sigma-Aldrich, Taufkirchen, Germany
Citric acid	Sigma-Aldrich, Taufkirchen, Germany
Coomassie Brilliant Blue	Bio-Rad Laboratories, Hercules, USA
Desferrioxamine (DFO-Bz-NCS)	Macrocyclics, Inc, Dallas, USA
Diaminobenzidine (DAB)	Medac Diagnostica, Wedel, Germany
Disodium phosphate	Sigma-Aldrich, Taufkirchen, Germany
DMEM	Invitrogen, Carlsbad, USA
DMSO	Sigma-Aldrich, Taufkirchen, Germany

D-PBS	Invitrogen, Carlsbad, USA
EDTA	Invitrogen, Carlsbad, USA
EnVision+ System- HRP labelled Polymer	Dako, Agilent Technologies, Glostrup, Denmark
Eosin	Merck, Darmstadt, Germany
Ethanol	Merck, Darmstadt, Germany
Ethidium Bromide	Roth, Karlsruhe, Germany
Ethidium monoazide (EMA)	Thermo Fischer Scientific, Waltham, USA
Fetal bovine Serum (FCS)	Invitrogen, Carlsbad, USA
Ficoll	Biochrom, Berlin, Germany
Gentisic acid	Sigma-Aldrich, Taufkirchen, Germany
Glacial acetic acid	Sigma-Aldrich, Taufkirchen, Germany
Glycine	Sigma-Aldrich, Taufkirchen, Germany
Goat serum	Abcam, Cambridge; UK
H_2SO_4 (1 M)	Roth, Karlsruhe, Germany
Haematoxylin	Merck, Darmstadt, Germany
Hanks' Balanced Salt Solution (HBSS)	Invitrogen, Carlsbad, USA
HCl 37 %	Sigma-Aldrich, Taufkirchen, Germany
HEPES	Invitrogen, Carlsbad, USA
Human IFN-γ ELISA Standard	Thermo Fischer Scientific, Waltham, USA
Human serum	TU Munich, München Germany
Isoflurane	CP Pharma, Burgendorf, Germany
Isopropyl alcohol	Merck, Darmstadt, Germany
L-Glutamine	Invitrogen, Carlsbad, USA
Methanol	Sigma-Aldrich, Taufkirchen, Germany
Milk powder	Sigma-Aldrich, Taufkirchen, Germany
Monosodium phosphate	Sigma-Aldrich, Taufkirchen, Germany
Mycophenolic acid (MPA)	Sigma-Aldrich, Taufkirchen, Germany
Na_2CO_3	Sigma-Aldrich, Taufkirchen, Germany
NaCl	Sigma-Aldrich, Taufkirchen, Germany
$NaHCO_3$	Sigma-Aldrich, Taufkirchen, Germany
NaN_3	Sigma-Aldrich, Taufkirchen, Germany
NaOH	Sigma-Aldrich, Taufkirchen, Germany
Non-essential amino acids	Invitrogen, Carlsbad, USA
Oxalic acid	Sigma-Aldrich, Taufkirchen, Germany
Paraformaldehyde (PFA)	Sigma-Aldrich, Taufkirchen, Germany

Penicilline/Streptomycine	Invitrogen, Carlsbad, USA
peqGOLD Protein Marker V	VWR, Radnor, USA
Pertex mounting medium	Histolab Products AB, Västra Frölunda, Sweden
Protamine sulfate	MP Biomedicals, Illkirch, France
RetroNectin	Takara, Japan
Roti®-Load 1 reducing protein loading buffer	Carl Roth, Karlsruhe, Germany
Roti®-Load 2 non-reducing protein loading buffer	Carl Roth, Karlsruhe, Germany
Rotiphorese® Gel 40	Carl Roth, Karlsruhe, Germany
RPMI	Invitrogen, Carlsbad, USA
Sodium acetate	Sigma-Aldrich, Taufkirchen, Germany
Sodium Dodecyl Sulfate (SDS)	Bio-Rad Laboratories, Hercules, USA
Sodium Pyruvate	Invitrogen, Carlsbad, USA
Target retrieval solution, citrate pH 6	Dako, Agilent Technologies, Glostrup, Denmark
TEMED	Sigma-Aldrich, Taufkirchen, Germany
TransIT Transfection Reagent	Mirus, Madison, USA
TRIS	Sigma-Aldrich, Taufkirchen, Germany
Trypsine EDTA (0.5 %)	PAA laboratories, Pasching, Austria
Tween20	Sigma Aldrich, Taufkirchen, Germany
Typan blue	Invitrogen, Carlsbad, USA
Ultra-low IgG Fetal Bovine Serum	BIO&SELL, Feucht bei Nürnberg, Germany
Xylene	Sigma Aldrich, Taufkirchen, Germany
Zirconium-89	BV Cyclotron VU, Amsterdam, Netherlands

Table 8. Reagents and chemicals

3.4 KITS

Reagent	**Company**
Anti-PE/Anti-APC/Anti-FITC Microbeads	Miltenyi Biotec, Bergisch Gladbach, Germany
Pierce™ BCA Protein Assay Kit	Thermo Fischer Scientific, Waltham, USA

Dynabeads human T activator CD3/CD28	Invitrogen, Carlsbad, USA
FIX & PERM® Cell Fixation & Cell Permeabilization Kit	Thermo Fischer Scientific, Waltham, USA
Human IFNγ ELISA Set	BD Bioscience, Franklin Lakes, USA
Pierce™ F(ab')$_2$ Preparation Kit	Thermo Fischer Scientific, Waltham, USA

Table 9. Kits

3.5 BUFFERS, SOLUTIONS AND MEDIA

3.5.1 Buffers and solutions

Buffer/solution	Composition	Application
Blocking buffer	1 % (m/m) milk powder in PBS	ELISA
Coating buffer	100 mM $NaHCO_3$ 30 mM Na_2CO_3, pH 9.5	ELISA
Coomassie staining solution	1 g/L Coomassie Brilliant Blue in Methanol 50 % (v/v), glacial acetic acid 10 % (v/v)	After SDS-PAGE
Elution buffer	25 mM $C_2H_3NaO_2$ 5 mg/ml gentisic acid pH 5.5	^{89}Zr-labeling/ Tracer storage
FACS buffer	1 % (v/v) ΔFCS in PBS	Flow cytometry
Fixation buffer	1 % (v/v) PFA in PBS	Flow cytometry
HEPES buffer	500 mM HEPES pH 7.1-7.3	^{89}Zr-labeling
Isolation buffer	0.2 % (v/v) ΔFCS 2 mM EDTA in PBS	Cell purification (MACS Isolation)
Mobile phase HPLC	0.1 M phosphate buffer 0.15 M NaCl 0.05 % (m/m) NaN_3 pH 6.2-7.0	HPLC
Mobile phase ITLC	20 mM citric acid	ITLC
Oxalic acid solution	1 M oxalic acid	^{89}Zr-labeling
Peroxidase blocking solution	3 % (v/v) hydrogen peroxide and 3 % (v/v) goat serum	IHC

Retronectin-solution	12 µg/ml RetroNectin in PBS	Retroviral transduction
Running buffer	25 mM TRIS, 192 mM Glycine, 0.1 % (v/v) SDS, pH 8.3	SDS-PAGE
Sodium acetate buffer	250 mM $C_2H_3NaO_2$ pH 4.9-5.5	DFO-conjugation / ^{89}Zr-labeling
Sodium bicarbonate buffer	100 mM $NaHCO_3$ pH 9	DFO-conjugation
Sodium carbonate solution	2 M Na_2CO_3	^{89}Zr-labeling
0.5 M HEPES pH 7		
Washing buffer	0,02 % (v/v) Tween20 in PBS	ELISA
ΔFCS	Inactivated FCS (20 min at 58 °C)	Media preparation, freezing of cells
ΔHS	Inactivated HS (20 min at 58 °C)	Flow cytometry, media preparation

Table 10. Buffers and solutions

3.5.2 Media

Medium	**Composition**
AIM-V	AIM-V (Invitrogen)
Binding medium	PBS supplemented with 1 % Bovine serum albumine (BSA)
cDMEM	DMEM supplemented with 10 % (v/v) FCS, sodium pyruvate (1 mM), L-glutamine (2 mM), non-essential amino-acids (10 mM) and penicilline/streptomycine (100 IU/ml)
cRPMI	RPMI supplemented with 10 % (v/v) FCS, sodium pyruvate (1 mM), L-glutamine (2 mM), non-essential amino-acids (10 mM) and penicilline/streptomycine (100 IU/ml)
Freezing medium	FCS supplemented with 10 % (v/v) DMSO
H57-597-hybridoma cell medium	RPMI supplemented with 10 % (v/v) ultra-low IgG FCS, sodium pyruvate (1 mM), L-glutamine (2 mM), non-essential amino-acids (10 mM) and penicilline/streptomycine (100 IU/ml)
NSO-cell medium	DMEM supplemented with 5 % (v/v) FCS, sodium pyruvate (1 mM), L-glutamine (2 mM), non-essential amino-acids

	(10 mM), penicilline/streptomycine (100 IU/ml) and 2 µl MPA per 25 ml DMEM
T-cell medium	RPMI supplemented with 5 % (v/v) ΔFCS, 5 % (v/v) ΔHS, sodium pyruvate (1 mM), L-glutamine (2 mM), non-essential amino-acids (10 mM), HEPES (10 mM), penicilline/streptomycine (100 IU/ml) and gentamycine (16 µg/ml).

Table 11. Media

3.6 ANTIBODIES

3.6.1 Antibodies used for flow cytometry

Antibody	Clone	Isotype	Company
Isotype control	MOPC-21	mIgG1	BD Bioscience, Franklin Lakes, USA
α-hCD16	3 G8	mIgG1κ	BD Bioscience, Franklin Lakes, USA
α-hCD3	UCHT-1	mIgG1κ	BD Bioscience, Franklin Lakes, USA
α-hCD32	FLI8.26	mIgG2bκ	BD Bioscience, Franklin Lakes, USA
α-hCD4	RPA-T4	mIgG1κ	BD Bioscience, Franklin Lakes, USA
α-hCD45	J.33	mIgG1	Beckman Coulter, Brea, USA
α-hCD45RA	HI100	mIgG2bκ	BD Bioscience, Franklin Lakes, USA
α-hCD45RO	UCHL1	mIgG2κ	BD Bioscience, Franklin Lakes, USA
α-hCD5	BL1a	mIgG2a	Beckman Coulter, Brea, USA
α-hCD62L	DREG-56	mIgG1κ	BD Bioscience, Franklin Lakes, USA
α-hCD64	10.1	mIgG1κ	BD Bioscience, Franklin Lakes, USA
α-hCD8	RPA-T8	mIgG1κ	BD Bioscience, Franklin Lakes, USA
α-mTCRb (TCRmu)	H57-597	hIgG2κ	BD Bioscience, Franklin Lakes, USA
α-γH2AX [p Ser139]	2F3	IgG1κ	Novus Biologicals, Littleton, USA

Table 12. Antibodies used for flow cytometry

3.6.2 Antibodies used for immunohistochemistry

Antibody	Clone	Isotype	Dilution	Company
α-CD3	SP7	rIgG	1:150	DCS, Hamburg, Germany
α-cleaved Caspase 3	Asp175	rIgG	1:200	Cell Signaling Technology, Danvers, USA
α-γH2AX	20E3	rIgG	1:480	Cell Signaling Technology, Danvers, USA

Table 13. Antibodies used for immunohistochemistry

3.7 CYTOKINES

Cytokine	Company
Human IL-2	PeproTech, London, UK
Human IL-7	PeproTech, London, UK
Human IL-15	PeproTech, London, UK

Table 14. Cytokines

3.8 PRIMARY CELLS AND CELL LINES

Cells	Application	Origin
CD8+central memory T cells (T_{CM})	Human primary cells used for transduction of TCR	Isolation from PBMCs by microbead-technology (Miltenyi)
Jurkat76	Human T-lymphoma cell line containing CD8+	Kind gift from M.Heemskerk (Heemskerk et al. 2003)
ML2 cells	Human acute myeloid leukemia (AML) cell line	The CABRI consortium
Murine B cell hybridoma H57-597	Production of TCRmu antibody	ATCC (HB-218)

NSO-IL15	Mouse myeloma cells transfected with the gene for human IL-15	Kind gift from S.R.Riddell (Wang, Berger et al. 2011)
Peripheral blood mononuclear cells (PBMC)	Human primary cells used for transduction of TCR	Isolation from the blood of healthy donors by density gradient centrifugation
T293 hamster embryonal kidney cells	Producer cell line for viral particles	ATCC

Table 15. Primary cells and cell lines

3.9 MOUSE MODEL

Mouse strain	**Purchased from**
NOD.Cg-*Prkdc*^{scid} *Il2rg*^{tm1Wjl}/SzJ (NSG)	Jackson Laboratory (Bar Harbor, Maine, USA)

3.10 SOFTWARE

AIDA Image analyzer software version 4.21
Bio-Chrom Lite
Chromatography Data System (CDS) Software Chromeleon version 6.8
Flow Jo version 7.6.5
Graph Pad prism version 5.01
Inveon Research Workplace
Leica Aperio ImageScope version 12.3.1.5011
Leica e-slide Manager
Microsoft Office (Word, Excel, Powerpoint) 2010
Windows EndNote X8

Table 16. Software

4 METHODS

4.1 CELL CULTURE METHODS

4.1.1 Freezing and thawing of cells

Cells were centrifuged before freezing at 500 g for 5 min, resuspended in 1 ml of freezing medium (table 11) and transferred to a cryotube. For gentle and controlled cooling of the samples, the tubes were put in specific freezing containers filled with isopropyl alcohol for one day at -80 °C. For long term storage, the vials were transferred in liquid nitrogen.

For thawing the tubes were put for a short time in warm water and cells were added to 10 ml of medium. The suspension was centrifuged at 500 g for 5 min and the cell pellet was resuspended in respective medium (table 11) and transferred in an appropriate cell culture flask.

4.1.2 Counting of cells

For counting cell suspensions were mixed with 4 % trypan blue solution dying dead cells. 10-20 µl of the cell mixture was counted using a Neubauer counting chamber in a light microscope. Dying cells were excluded during counting and cell concentration per ml was calculated by following formula:

$$c\left(\frac{\text{viable cells}}{\text{ml}}\right) = \frac{\text{total number of alive cells in chamber squares}}{\text{number of chamber squares}} \cdot \text{dilution factor} \cdot 10^4$$

4.1.3 Cultivation of cell lines

Suspension cells were cultured in appropriate medium (table 11) at 37 °C in 5 % CO_2/humidified air atmosphere and were split after every third or fourth day of cultivation.

Semi-adherent T293 cells were split by loosening the cells without the use of trypsin/EDTA or PBS wash and were diluted in the appropriate amount of medium before seeding in new culture flasks.

4.2 PURIFICATION OF PRIMARY CELLS

4.2.1 Isolation of peripheral blood mononuclear cells (PBMC)

Peripheral blood mononuclear cells (PBMC) were isolated from blood of healthy and consenting donors and according to requirements of the local ethical board and principles of the Helsinki Declaration. 15 ml of Ficoll in a 50 ml tube was overlayed with the heparinized whole blood being diluted 1:2 with serum-free RPMI medium for subsequent densitiy-gradient centrifugation for 20 min at 880 g without break. The PBMC containing interface was collected, washed twice in RPMI and transferred in medium for counting and further isolation of CD8+ T_{CM} cells (section 4.4.2).

4.2.2 Purification of CD8+ CD62L+ CD45RA- T_{CM} cells

The CD8+ T_{CM} cells were isolated from freshly obtained PBMC (section 4.4.1) by first depleting CD4+ and CD45RA+ cells and subsequent enrichment of CD62L+ cells. For the depletion 3 x 10^8 of freshly isolated PBMC were resuspended in 800 µl of isolation buffer and 100 µl of anti-CD4-FITC and 100 µl anti-CD45RA-APC were added before incubation for 15 min at 4 °C while rotating. After that cells were rinsed with isolation buffer, resuspended in 80 µl isolation buffer and 20 µl of anti-APC and 10 µl of anti-FITC beads were added per 10^7 cells. Then cells were rinsed and resuspended in 80 µl isolation buffer per 10^7 cells before loading 500 µl (3 x 10^8 cells in 1 ml isolation buffer) in one LD column according to manufactures instructions. The flow through consisting of the CD45RA-/CD4- fraction was counted and resuspended in 80 µl isolation buffer and 20 µl anti-CD62L-PE per 10^7 cells.

The cells were incubated at 4 °C for 15 min while rotating, before rinsing and resuspension in 80 µl isolation buffer and 20 µl anti-PE microbeads per 10^7 cells. After repeated incubation at 4 °C for 15 min while rotating, cells were washed, resuspended in 500 µl isolation buffer and loaded on a MS column following the manufactures instructions. The eluate consisting of CD45RA-/CD4-/CD62L+ cells were counted and activated for retroviral transduction (section 4.5.2). The purity and phenotype of the cells were analyzed in all steps by flow cytometry (section 4.6.1).

4.2.3 Activation of T_{CM}

Isolated T_{CM} were activated by the addition of CD3/CD28 beads (table 9) in a bead to cell ratio of 1:1 and 30 IU/ml hIL-2 (table 14). For 1 x 10^6 T_{CM} in 1 ml T-cell medium, 25 µl of the CD3/CD28 beads were rinsed with isolation buffer and were added to the T_{CM} cell suspension. The cells were seeded in a 12-well plate and were incubated for 2 to 3 days at 37 °C for subsequent retroviral transduction (section 4.5.2).

4.3 GENE TRANSFER TECHNIQUES

4.3.1 Production of retroviral particles

For the generation of retroviral particles, the T293 cell line (table 15) was applied as production host. Therefore, 2 x 10^5 to 3 x 10^5 cells in 3 ml cDMEM were seeded in a treated 6-well plate 24 h prior transfection. At the next day, 9 µl of TransIT-293 transfection reagent was mixed, added to 200 µl serum-free DMEM and incubated for 20 min at room temperature. 1 µg of the DNA vectors pcDNA3.1-MLV ("gag-pol"), pALF10A1-GALV ("env") and pMP71 coding for the gene of interest was added, mixed by pipetting and incubated for further 30 min at room temperature. The medium of the T293 cells was changed and the transfection mixture was added dropwise to the cells in the wells. After incubation for 48 h at

37 °C, the virus containing supernatant was harvested and removed from cells by centrifugation and filtering through a 0.45 µm syringe filter.

4.3.2 Transduction of activated T_{CM}

Transduction of activated T_{CM} was performed in RetroNectin coated non-treated 24-well plates. For that, 400 µl RetroNectin solution (table 10) was added in every well and the plate was sealed with parafilm for overnight incubation at 4 °C. At the next day, for blocking the RetroNectin solution was removed and 500 µl 2 %BSA in PBS was added in each well for 30 min at 37 °C. Afterwards the wells were rinsed twice with PBS 2.5 % HEPES and were stored for subsequent transduction at 4 °C. For transduction 1×10^6 activated T_{CM} were harvested and supplemented in 1 ml T-cell medium with 50 IU/ml hIL-2, 1 % HEPES and 4 µg/ml protamine sulfate (concentrations in final volume of 2 ml) for seeding in RetroNectin coated plates. 1 ml of filtered virus supernatant (4.5.1) was added to the T_{CM} and the plate was centrifuged for 90 min at 880 g and 32 °C. The plate was incubated at 37 °C for 24 h, followed by harvesting and splitting the cells 1:2 in a new RetroNectin coated plate for a repetitive transduction with 1 ml of virus supernatant per well. At the next day, the cells were harvested, rinsed and transferred in T75 cell culture flasks at a concentration of 1×10^6 cells/ml in T-cell medium supplemented with hIL-7 and hIL-15 (both 5 ng/ml). After 3 to 4 days of cultivation, the transduction efficiency was assessed by flow cytometry (section 4.6.1).

4.3.3 Transduction of cell lines

For transduction of cell lines, 3×10^5 cells in 1 ml of respective medium were seeded in a well of a RetroNectin coated 24-well plate. 1 ml of filtered virus supernatant and protamine sulfate (4 µg/ml) and 1 % HEPES were added followed by centrifugation for 90 min at 880 g and 32 °C. After incubation at 37 °C, cells were rinsed and transferred in T25 cell culture flasks in

respective medium for cultivation. The transduction efficiency was analyzed by flow cytometry (section 4.6.1).

4.4 FLOW CYTOMETRY AND FLOW CYTOMETRY BASED ASSAYS

4.4.1 Staining of surface molecules

To analyze molecules expressed on the surface of cells, 1×10^5 to 1×10^6 cells were centrifuged and rinsed with FACS buffer (table 10). To block Fc-receptors on the surface, the cells were incubated for 10 min at 4 °C with 100 µl of ΔHS (table 10). Afterwards cells were rinsed with FACS buffer and incubated with 1.5 µl of the respective antibody (table 11) in a total volume of 50 µl FACS buffer for 20 min at 4 °C in the dark. For dead cell discrimination, the samples were co-incubated with 7-AAD at a final concentration of 5 ng/µl. Before analysis, the cells were rinsed and resuspended in 200 µl fixation buffer (table 11). After measurement, data were analyzed by FlowJo Software version 7.6.5.

4.4.2 Determination of the binding affinity of aTCRmu-IgG/F(ab')$_2$

For the determination of the dissociation constant (K_d) of unmodified aTCRmu-IgG/F(ab')$_2$, 3×10^5 TCR2.5D6 expressing Jk76 were incubated with different final working concentrations of the proteins (table 17) for 1 h at 4 °C. Afterwards, the cells were rinsed with FACS buffer and were incubated with 1.5 µl aTCRmuβ-FITC antibody and 7-AAD in FACS buffer at a total volume of 50 µl for 20 min at 4 °C in the dark. The cells were rinsed again with FACS buffer and resuspended in fixation buffer for measurement. As the TCR2.5D6 receptors were blocked by aTCRmu-IgG/F(ab')$_2$ before competitive staining with aTCRmuβ-FITC, the mean fluorescence intensity (MFI) values were decreasing with increasing protein concentration. Subtraction of the MFI values from the total MFI value in the control sample with no protein

yielded theoretical MFI values of the single concentrations. The dissociation constants were calculated by plotting the theoretical MFI values versus protein concentrations and non-linear regression analysis using the GraphPad Prism 5.01 software.

	Working concentrations aTCRmu-IgG/F(ab')$_2$
WC1	1 x 10^{-8} M
WC2	5 x 10^{-8} M
WC3	1 x 10^{-9} M
WC4	5 x 10^{-9} M
WC5	1 x 10^{-10} M
WC6	5 x 10^{-10} M
WC7	1 x 10^{-11} M
WC8	5 x 10^{-11} M
WC9	1 x 10^{-12} M

Table 17. Working concentrations of aTCRmu-IgG/F(ab')$_2$ for the determination of the binding affinities via flow cytometry.

4.4.3 T-cell quantification via counting beads

In order to estimate the absolute number of infiltrated and visualized TCR2.5D6 iRFP T_{CM}, cell suspensions of the dissected ML2-B7/ML2-B15 tumors were prepared by tissue homogenization using 40 µm cell strainer. Identification of engrafted TCR2.5D6 iRFP T_{CM} in the tissues was performed via flow cytometry analysis by staining the cell suspensions for the human leukocyte marker hCD45 and the T-cell marker hCD5 (table 12) and final gating for iRFP positive cells. The quantification of TCR2.5D6 iRFP T_{CM} was carried out by adding 100 µl AccuCheck Counting Beads to 100 µl of pre-stained cell suspension. The samples were mixed well and measured by flow cytometry. The absolute number of iRFP positive cells in the measured samples was calculated based on the cell counts of iRFP positive cells and the counts of the quantification beads according to the formula provided by the manufactures protocol:

$$\text{Absolute count } \left(\frac{\text{cells}}{\mu\text{l}}\right) = \frac{\text{number of cells counted}}{\text{total number of beads counted}} \cdot \text{number of AccuCheck counting beads per µl}$$

The counted number was extrapolated to the total volume of the whole cell sample.

4.5 FUNCTIONAL ANALYSIS OF T CELLS AFTER TRACER BINDING

4.5.1 Co-incubation and IFN-γ enzyme linked immunosorbent assay (ELISA)

TCR-transgenic T_{CM} were first labeled in two groups with ^{89}Zr-Df-aTCRmu-F(ab')$_2$ and non-radioactive aTCRmu-F(ab')$_2$ for 1 h at 4 °C in binding medium (table 11) at the final working concentrations listed in table 18. Then the cells were centrifuged and rinsed with binding medium before stimulation of both groups in triplicates in 96-U-bottom well plates with ML2-B7 or ML2-B15 (control) tumor cells at a target to effector ratio of 1:1 in 200 µl T-cell medium. After co-incubation for 24 h at 37 °C, the supernatant was collected and stored at -20 °C. For assessment of IFN-γ release of the T_{CM} after 48 h, fresh T-cell medium was added to the cells for co-incubation for further 24 h and subsequent supernatant collection. The quantitative level of IFN-γ release by T_{CM} was measured by the human IFN-γ ELISA set with slight modifications in the protocol. IFN-γ capture antibody was diluted 1:250 in ELISA coating buffer (table 11) and a Nunc MaxiSorp ELISA plate was coated with the solution before sealing and incubation overnight at 4 °C. Then the plate was rinsed 3 times and unspecific binding sites were blocked for 1 h at room temperature by the addition of blocking buffer (table 11). After rinsing the plate 3 times with washing buffer (table 11), for the standard curve 50 µl of 1:2 serially diluted IFN-γ standard (1000 pg/ml to 31.25 ng/ml) was pipetted in duplicates. 50 µl of the samples were added in triplicates and the plate was incubated for 1 h at room temperature. After washing the wells 5 times, 50 µl of the detection solution (1:250 diluted biotinylated detection antibody and Streptavidin-horseradish peroxidase (HRP) conjugate in blocking buffer) was given for further incubation for 1 h at

room temperature. The plates were rinsed 7 times before adding 100 µl of the substrate solution (TMB substrate Reagent Set, BD) per well and incubation for 10-15 min in the dark at room temperature. The reaction was stopped by addition of 50 µl 1 M H_2SO_4. The extinction was measured at 450 nm and 570 nm as reference wavelength with an ELISA reader.

Working concentrations ^{89}Zr-Df-aTCRmu-F(ab')$_2$/aTCRmu-F(ab')$_2$	
WC1	1 x 10^{-7} M
WC2	5 x 10^{-8} M
WC3	1 x 10^{-8} M
WC4	5 x 10^{-9} M
WC5	1 x 10^{-9} M
WC6	5 x 10^{-10} M
WC7	1 x 10^{-10} M

Table 18. Working concentrations of ^{89}Zr-Df-aTCRmu-F(ab')$_2$/aTCRmu-F(ab')$_2$ for the IFN-γ ELISA.

4.5.2 γH2AX staining after tracer co-incubation in vitro

To evaluate viability via the impact of the radioactive tracer on DNA level of TCR2.5D6 iRFP T_{CM}, DNA double-strand break (DSB) induction was assessed after exposure of the T cells to the radioactive tracer by measuring the expression of nuclear DSB-marker γH2AX. Two groups of TCR2.5D6 iRFP T_{CM} (3 x 10^4 cells/ml each sample) were incubated in triplicates with tracer activities ranging from 0 to 1000 µCi (0.0-37.0 MBq) for 1 h at 4 °C. One group was immediately rinsed with FACS buffer (table 11) and stained for dead cells using Ethidium Monoazide at a final concentration of 0.5 µg/mL (EMA; table 8). Therefore, the cells were first incubated in the dark for 10 min and for additional 10 min under fluorescent light. After rinsing, cells were fixed and permeabilized using FIX & PERM kit followed by staining with anti-γH2AX-AlexaFluor488® antibody (table 12). The other group was rinsed and resuspended in T-cell medium before incubation for further 48 h at 37 °C for investigating the long-term effects of tracer exposure. The stained cells of both groups were rinsed with FACS

buffer and analyzed by the LSR II Flow Cytometer system. TCR2.5D6 iRFP T_{CM} cells being not exposed to any tracer served as control group.

4.5.3 γH2AX staining after tracer exposure in vivo

For assessing radiation damage of *in vivo* infiltrated T cells after being exposed to i.v. transferred ^{89}Zr-Df-aTCRmu-F(ab')$_2$, the infiltrated and dissected ML2-B7 tumors were assessed for γH2AX and cleaved Caspase 3 expression as markers for radiation damage and viability. NSG mice were inoculated on the right and left flank subcoutaneously (s.c.) with 1 x 10^7 ML2-B7 tumor cells. After 8 days 20 x 10^6 TCR2.5D6 iRFP T_{CM} were transferred intravenously and additionally 15 x 10^6 hIL-15 producing NSO cells were injected intraperitoneally to support T_{CM} expansion and engraftment (previously irradiated with 80 Gray (Gy)). 3 days after adoptive T-cell transfer one group of animals received 2.2 MBq of the radiotracer ^{89}Zr-Df-aTCRmu-F(ab')$_2$ i.v., while the other group (control group) did not receive the radiotracer. After 48 h animals were sacrificed and tumors of both flanks were taken for further immunohistochemical (IHC) analysis for CD3, γH2AX and cleaved Caspase 3 (section 4.11.4).

4.6 PROTEINBIOCHEMISTRY

4.6.1 Antibody purification and F(ab')$_2$ digestion

The murine B cell hybridoma cell line H57-597 (ATCC HB-218), producing the Armenian Hamster anti-murine TCR β chain antibody (aTCRmu-IgG), was cultured in hybridoma medium supplemented with bovine IgG free serum (table 11) at 37 °C. The cells were cultured and expanded over 2 weeks for supernatant production and harvesting. The purification of aTCRmu-IgG in the supernatant was performed by the Monoclonal Antibody Core Facility at the Helmholtz Zentrum München. Briefly, aTCRmu-IgG was affinity purified

using Protein A Sepharose and was dialyzed over night against PBS. The functionality of the purified fraction was confirmed by ELISA. F(ab')$_2$ fragments of aTCRmu-IgG were generated by Pepsin digestion followed by Protein A purification using a F(ab')$_2$ preparation kit. aTCRmu-IgG and aTCRmu-F(ab')$_2$ were stored in 0.05 % sodium azide in PBS at 4 °C and were stable over several months.

4.6.2 Protein concentration and buffer exchange

The antibody fragment was concentrated after pepsin digestion (section 4.8.1) for the subsequent chelator conjugation (section 4.9.1) in Amicon Ultra-15 Centrifugal Filter Units. Therefore, the respective buffer was added to the diluted protein in the filter and the unit was centrifuged at 4000 g for 15 min at room temperature. The concentrated protein was diluted in the desired volume of respective buffer. A buffer exchange was performed as described for the protein concentration.

4.6.3 Determination of protein concentration

The concentration of the aTCRmu-IgG or aTCRmu-F(ab')$_2$ was determined by a NanoPhotometer at an absorbance of 280 nm using an extinction coefficient of 1.4.

4.6.4 SDS polyacrylamide gel electrophoresis (PAGE) and Coomassie staining

The preparations were analyzed by SDS-PAGE gel electrophoresis in the Mini-PROTEAN® Tetra cell system (Bio-Rad) under reducing conditions using 4 % Tris-HCl Polyacrylamide as stacking gel and 10 % Tris-HCl Polyacrylamide for separation (table 19).

	Stacking gel 4 %	Separating gel 10 %
H_2O	3 ml	4.1 ml
1.5 M Tris/HCl pH 8.6	-	2.5 ml
0.5 M Tris/HCl pH 6.6	1.2 ml	-
30 % Acrylamid-Bisacrylamid	0.7 ml	3.3 ml
10 % SDS	50 µl	100 µl
10 % APS	50 µl	100 µl
TEMED	5 µl	10 µl

Table 19. Composition of polyacrylamide separating and stacking gels for SDS PAGE.

The separation gel was poured and layered with isopropyl alcohol and was left for polymerization at room temperature for 30 min. The isopropyl alcohol was removed before the stacking gel solution and a comb were added on the top of the separation gel for polymerization for further 30 min at room temperature. The gel was placed in the electrophoresis chamber and 1 x running buffer was added. About 30 µg of the protein samples were denaturated by addition of reducing or non-reducing loading buffer and heating at 90 °C for 2 min. The samples as well as a protein reference marker (Protein marker V) were loaded in the wells of the stacking gel and electrophoresis was performed at 100 V for 1 h. To visualize the protein bands the gel was rinsed after separation with ddH_2O and stained with Coomassie solution (table 10) for at least 3 h. After staining the gel was repeatedly rinsed with ddH_2O and stored in ddH_2O at 4 °C.

4.7 CHELATOR CONJUGATION AND RADIO-LABELING OF ATCRMU-IGG AND ATCRMU-F(AB`)$_2$

4.7.1 DFO-conjugation of aTCRmu-IgG and aTCRmu-F(ab')$_2$

The aTCRmu-IgG and aTCRmu-F(ab')$_2$ functionalization by conjugation of the p-isothiocanatobenzyl derivate of desferrioxamine (DFO-Bz-NCS) for the formation of a tracer complex with the radionuclide zirconium-89 (section 4.9.2) was performed according to the

protocol described by Perk et al. (Perk et al. 2010) with slight modifications. 2-3 mg of aTCRmu-IgG and aTCRmu-F(ab')$_2$ were concentrated and buffer exchanged in $NaHCO_3$ 0.1 M pH 9 to a total volume of 500 µl. DFO-Bz-NCS was dissolved in DMSO to a final concentration of 5 mM and a 3-fold molar excess was added to the protein solution followed by incubation at 37 °C for 30 min. Unbound chelator was purified from the sample by size exclusion using a PD10 column and NaOAc 0.25 M pH 5.5 as elution and storage buffer for the immunoconjugate.

4.7.2 ^{89}Zr-radiolabeling of aTCRmu-IgG and aTCRmu-F(ab')$_2$

The radionuclide zirconium-89 (^{89}Zr; $t_{1/2}$= 78.41 h; E_{max} β+=0.9 MeV) was purchased from the cyclotron BV Cyclotron VU Amsterdam and the radiolabeling of the DFO-conjugate of aTCRmu-IgG and aTCRmu-F(ab')$_2$ was performed based on the protocol of Vosjan et al. (Vosjan et al. 2010) with slight modifications. Briefly, 37.0 to 74.0 MBq of ^{89}Zr in 100 µl 1 M oxalic acid was adjusted to pH 7.0-7.2 with 45 µl 2 M Na_2CO_3 and 150 µl 0.5 M HEPES pH 7.0 followed by addition of 100 to 250 µg DFO- aTCRmu-IgG/ aTCRmu-F(ab')$_2$ in 355 µl NaOAc 0.25 M pH 5.5 and 350 µl 0.5 M HEPES pH 7.0. After incubation for 30 min at 37 °C, the ^{89}Zr-Df-immunocomplex was purified from free activity by size exclusion in a PD-10 column using 0.25 M sodium acetate/gentisic acid 5 mg/ml pH 5.5 as elution and storage buffer. The quality control in terms of radiochemical purity (RCP) was assessed by Instant thin layer chromatography (ITLC) and radio-high performance liquid chromatography (HPLC) (section 4.10).

4.8 ANALYTICAL METHODS

4.8.1 Instant thin layer chromatography (ITLC)

ITLC was performed on glass microfiber chromatography paper impregnated with silic acid using 0.1 M sodium citrate pH 5 as mobile phase. Therefore 2.5 µl of the radiolabeled sample was spotted on the baseline of the TLC strip (R_f 0.0) and the solvent was run up to 10 cm. The read-out was performed by a radio-TLC-scanner and data were analyzed by the Bio-Chrom Lite software. Radiolabeled protein appeared at R_f 0.0-0.2, while unbound free ^{89}Zr revealed a peak at R_f 0.4-1.0.

4.8.2 Size exclusion high performance liquid chromatography (SE-HPLC)

(Radio)-SE-HPLC was performed in the LC-20A Prominence HPLC system using a Yarra™ 3 µm SEC-3000 LC column and 0.15 M NaCl 0.05 M phosphate buffer pH 7.0 as mobile phase at an isocratic flow rate of 1.0 ml·min-1. UV-VIS profiles of the proteins were acquired at 280 nm and the radioactive detection was performed by a GABI Star γ-detector. Data acquisition and analyze were performed with the Chromeleon 6.8 chromatography data system software.

4.9 IN VITRO AND IN VIVO CHARACTERIZATION OF ^{89}ZR-DF-ATCRMU-IGG AND ^{89}ZR-DF-ATCRMU-F(AB')$_2$

4.9.1 Determination of the binding affinity of ^{89}Zr-Df-aTCRmu-IgG and ^{89}Zr-Df-aTCRmu-F(ab')$_2$ to 2.5D6 transduced T cells

For the determination of the dissociation constant (K_d) of the tracer, 3 x 10^5 TCR2.5D6 iRFP T_{CM} were incubated in triplicates with different concentrations of ^{89}Zr-Df-aTCRmu-IgG or ^{89}Zr-

Df-aTCRmu-F(ab')$_2$. (table 20). To assess non-specific binding for each tracer concentration, one group was additionally incubated with a 100-fold molar excess of non-labeled aTCRmu-IgG or aTCRmu-F(ab')$_2$. After incubation for 1 h on ice and rinsing with PBS/1 %BSA, the cell pellets were measured in a gamma counter. Specific binding of the tracer was obtained by subtraction of non-specific binding from total tracer binding to the cells. The dissociation constant was calculated by plotting counts per minute values (cpm) versus tracer concentrations and non-linear regression analysis using the GraphPad Prism 5.01 software.

	Working concentrations ^{89}**Zr-Df-aTCRmu-IgG/F(ab')$_2$**
WC1	5 x 10^{-7} M
WC2	1 x 10^{-8} M
WC3	5 x 10^{-8} M
WC4	1 x 10^{-9} M
WC5	5 x 10^{-9} M
WC6	1 x 10^{-10} M
WC7	5 x 10^{-10} M
WC8	1 x 10^{-11} M
WC9	5 x 10^{-11} M
WC10	1 x 10^{-12} M

Table 20. Working concentrations of ^{89}Zr-Df-aTCRmu-IgG/F(ab')$_2$ for the determination of the binding affinities.

4.9.2 Determination of the immunoreactivity of ^{89}Zr-Df-aTCRmu-IgG and ^{89}Zr-Df-aTCRmu-F(ab')$_2$

The immunoreactivity of the ^{89}Zr-labeled aTCRmu-IgG and aTCRmu-F(ab')$_2$ was determined by the approach described by Lindmo et al. (Lindmo et al. 1984), determining the fraction of immunoreactive tracer by linear extrapolation of tracer binding to conditions representing infinite antigen excess. Serial dilutions of TCR2.5D6 transduced Jurkat76-CD8α cells were prepared in triplicates containing 2.6 x 10^6 to 8.13 x 10^4 cells/well and were incubated for 1 h on ice in human serum to block unspecific binding. Cell samples were incubated with 20 ng of ^{89}Zr-Df-aTCRmu-IgG or ^{89}Zr-Df-aTCRmu-F(ab')$_2$ for 2 h on ice, while a 1000-fold excess of

unlabeled aTCRmu-F(ab')$_2$ was additionally added to the control group for determination of non-specific binding. The cells were rinsed twice with PBS/1 % BSA and associated radioactivity was measured in a γ-counter. The obtained data were plotted as the quotient of background corrected total bound and specific bound activity versus the reciprocal of the cell concentrations. Linear regression analysis has been performed using GraphPad Prism 5.01 software. The Y-intercept resulted in the reciprocal of the percentage of the immunoreactive fraction.

4.9.3 In vitro stability analysis of ^{89}Zr-Df-aTCRmu-IgG and ^{89}Zr-Df-aTCRmu-F(ab')$_2$

The stability of ^{89}Zr-Df-aTCRmu-IgG or ^{89}Zr-Df-aTCRmu-F(ab')$_2$ was investigated *in vitro* in different test media: human serum, PBS buffer solution (pH 7.0), 0.25 M sodium acetate/gentisic acid 5 mg/ml buffer solution (pH 5.5) and 50 mM Diethylenetriaminepentaacetic acid (DTPA) solution. Therefore, 3.7 MBq of the tracer was added to a total volume of 1 mL of test medium and incubated for up to 96 h at 37 °C. Samples from each test medium were spotted every 24 h on ITLC silica gel strips, which were separated using 0.1 M sodium citrate pH 5.0 as mobile phase. After the read-out of the strips, the Bio-Chrom Lite software was calculating the percentage of protein-bound activity at the retardation factor (R_f) 0.0-0.2 versus free ^{89}Zr at $R_f \geq 0.8$.

4.9.4 In vivo stability analysis of ^{89}Zr-Df-aTCRmu-IgG and ^{89}Zr-Df-aTCRmu-F(ab')$_2$

The *in vivo* stability of ^{89}Zr-Df-aTCRmu-F(ab')$_2$ was investigated in mice by assessing the presence of intact tracer in the blood pool, kidneys and liver. Therefore, 8.5-9.0 MBq of ^{89}Zr-Df-aTCRmu-F(ab')$_2$ was injected i.v. in 3 groups of NOD.Cg-Prkdc^{scid} Il2rg^{tm1Wjl}/SzJ (NSG) mice. The mice were sacrificed 6, 24 and 48 h after the tracer injection and blood, kidney and liver were taken. Liver and kidney were quick-freezed in liquid nitrogen for homogenization in a ball mill. The homogenizates were extracted with PBS and centrifuged in ultrafiltration units

(MWCO 300 000 Da). The blood samples were centrifuged for separation of the plasma from blood cells and plasma proteins were precipitated by addition of acetonitrile (50 % v/v) for 10 min at 4 °C and subsequent centrifugation. Samples were loaded on SDS-PAGE gels and separation was performed as described in section 4.8.4. Afterwards phosphorimaging plates were exposed to the gels for 24 h followed by read-out with a Phosphor-imager. The signal intensity in regions of interest (ROI) associated with intact tracer in respective organ samples was analyzed by AIDA Image analyzer software.

4.9.5 Internalization of ^{89}Zr-Df-aTCRmu-IgG and ^{89}Zr-Df-aTCRmu-F(ab')$_2$ in 2.5D6 transduced T cells

For assessing the interaction of the radio-tracer with TCR2.5D6 iRFP T_{CM} ratios of internalized and cell membrane bound radio-tracer at different time points were determined. Two groups of 1×10^6 T cells/sample in triplicates were pre-incubated in binding medium (table 11) for 1 h on ice, followed by incubation with 20 nM ^{89}Zr-Df-aTCRmu-IgG or ^{89}Zr-Df-aTCRmu-F(ab')$_2$ for further 1 h on ice. One group was additionally incubated with a 100-fold molar excess of unlabeled aTCRmu-IgG for determining non-specific binding. Excessive tracer was removed by centrifugation at 500 g for 5 min and the cells were resuspended in serum-free T-cell medium for incubation at 37 °C. At defined time points (5, 15, 30, 60, 120 and 240 min), the cells were centrifuged and the supernatant (unbound fraction) and the fraction obtained after rinsing with serum-free T-cell medium were collected and pooled. The membrane-bound fraction was obtained by pooling the acid wash using 0.05 M NaOAc in NaCl pH 2.0 and the rinsing fraction with the acid wash buffer. The pelleted T cells were lysed in 1 M NaOH and activity of the three fractions was measured in a gamma-counter.

4.10 ANIMAL EXPERIMENTS

The animal experiments were conducted in accordance with the German Animal Welfare Act (Deutsches Tierschutzgesetz, approval # 55.2-1-54-2532-52-14) and mice were maintained in the animal facility of Klinikum rechts der Isar according to institutional guidelines. The animals were used for the described experiments at the age of 8 to 12 weeks. The elaboration of the animal model and the injections of tumor and T cells were performed by Dr. Sabine Mall, III. Medical Department, Klinikum rechts der Isar.

4.10.1 ML2 Tumor model

The ML2-B7 GFP or ML2-B15 GFP tumor cells were harvested and resuspended in PBS at a cell concentration of 1×10^7 in 200 µl. ML2-B7 GFP cell were injected subcutaneously into the right flank and ML2-B15 GFP into the left flank of NSG mice. The tumor growth was observed by caliper measurement and the animals were ready for further treatments 8 to 9 days after injection.

4.10.2 Adoptive T-cell transfer

For the adoptive T-cell transfer different numbers of TCR2.5D6 iRFP T_{CM} or non-transduced T_{CM} in a total volume of 200 µl PBS were injected i.v. into the tail vein of NSG mice. To support the proliferation and engraftment of the T cells, *in vivo* irradiated (80 Gy) hIL-15 producing NSO cells were injected 2 to 3 times intraperitoneally in the week before T-cell transfer (Wang et al. 2011).

4.10.3 Total body irradiation (TBI) of mice

To support the engraftment of the adoptively transferred T_{CM} the day before injection the animals were irradiated in a Gulmay irradiation cabinet. The irradiation was performed with 1 Gy in a specific cage holding the mice plane allowing consistent irradiation of all animals.

4.11 PET/CT IMAGING

4.11.1 Small animal imaging

All the imaging studies were performed at an Inveon small animal PET/CT device. Before imaging the animals were anesthetized with 1.5 % isoflurane followed by tracer injection into the tail vein (10-20 µg corresponding to 0.7-1.5 MBq). The animals were placed in the device in prone position under constant anesthesia with 1.5 % isoflurane. After CT acquisition, static PET emission imaging was performed for an acquisition time of 30 min in the range of 400-650 keV. The image reconstruction was conducted by a 3-dimensional ordered subsets maximum a posteriori algorithm (OSEM3D/MAP) applying 16 subsets and 18 iterations. The matrix resulted in 128 x 128 pixels with 159 transverse slices (voxel size 0.78 x 0.78 x 0.80 mm^3). The data were finally normalized and corrected for randoms, dead time and decay.

4.11.2 Image analysis by Siemens INVEON Research Workplace

For image-based signal quantification, the images were further processed using the Inveon Research Workplace software. The tracer uptake was displayed as percentage of injected dose per gram (%ID/g) and images were shown as 3D-maximal intensity projection (MIP) of co-registered PET/CT images. For the quantification of the activity in a defined volume, regions of interest (ROI) were drawn along the contours of the CT images-and activities in

that area were expressed in the PET image as mean values of 50-100 % of maximum uptake (Bq/ml).

4.12 EX VIVO ANALYSIS

4.12.1 Biodistribution analysis

The biodistribution analysis of the animals were performed 48 h after ^{89}Zr-Df-aTCRmu-F(ab')$_2$ injection and PET/CT imaging. The uptake of the radiotracer was examined in blood and diverse tissues (tumors, lung, liver, spleen, kidneys and muscle) after sacrificing the animals. The tissues were taken, weighted and were quantified in a gamma-counter. 5 replicates of standard containing 1 % of injected activity were measured additionally to every set. The uptake was expressed as percentage of injected dose per gram of tissue (%ID/g) and allowed tissue to blood or tissue to muscle ratio calculations.

4.12.2 Autoradiography

For determining the activity accumulation of ^{89}Zr-TCRmu-Df-F(ab`)$_2$ on tissue level after PET/CT imaging, chosen organs were taken and flash freezed in nitrogen. The organs were cut in a cryotome in several 20 µm slices, which were instantly attached on object slides. The slides were placed on phosphor imaging plates, which were exposed to the radioactive tissue samples for 48 h. The signal intensities on the plates deriving from the radioactive tissues were measured by an imaging plate reader and images were analyzed using AIDA Image analyzer software.

4.12.3 Preparation of tissues to single cell suspensions

Single cell suspension preparations of selected tissues were produced after dissection using 40 µm cell strainers. The preparations were suspended in 20 %BSA PBS buffer and were used for flow cytometric analysis (section 4.6).

4.12.4 Histology and Immunohistochemistry (IHC)

Immunohistochemical stainings were performed in collaboration with Dr. Katja Steiger, Institute of Pathology, comparative experimental pathology (CeP), Klinikum rechts der Isar. Selected tissues were fixed in 10 % neutral-buffered formalin solution for at least 24 h, dehydrated and embedded in paraffin. For histological and IHC analyses, serial sections of 2 µm were cut using a rotary microtome. Before Hematoxylin-Eosin (H.-E.) staining, the sections were deparaffinized with xylene and were rehydrated. For IHC, the slides underwent additionally heat induced antigen retrieval using target retrieval solution pH 6.0 and unspecific protein and peroxidase blocking (3 % hydrogen peroxide and 3 % goat serum). IHC was performed with an autostainer using antibodies against CD3, γH2AX and cleaved Caspase 3 (table 13). Antibody detection was performed using Envision-HRP rabbit labeled polymer and visualization with diaminobenzidine (DAB). Counterstaining was performed using hematoxylin and slides were dehydrated and coverslipped with mounting medium. Slides were scanned with a Leica AT2 system to an e-slide manager database and were analyzed with the Imagescope software. For the co-localization of double-strand breaks and apoptosis in infiltrated T cells, consecutive slides depicting γH2AX, cleaved Caspase 3 and CD3 expression were compared simultaneously. The number of positive pixels was evaluated with the positive pixel count algorithm after immunohistochemical staining for CD3.

4.13 STATISTICS

The data are presented as mean ± standard deviations (SD). Statistical data analysis was calculated by GraphPad Prism 5.01 software applying a two tailed non-parametric test (Mann-Whitney test) as shown in the figure legends.

5 RESULTS

5.1 TRACKING STRATEGY OF TCR2.5D6 TRANSDUCED T_{CM} BY PET/CT

It has been shown that after genetic transfer, mouse T-cell receptors are highly expressed at the surface of human T cells and have potential to replace human TCR on the surface (Sommermeyer et al. 2006; Voss et al. 2006). This observation led to several studies working with human-murine hybrid TCR indicating reduced mispairing of introduced and endogenous TCR (Voss et al. 2006; Cohen et al. 2006; Hart et al. 2008; Thomas et al. 2007). For the studies, the antigen-specific human TCR2.5D6 harboring a murinized constant domain in the TCRβ chain was used, which has been extensively characterized by Richard Klar et al. (Klar et al. 2014). This murinized domain allows the hamster anti-murine TCR antibody (H57-597; aTCRmu) to be specifically recognized (Kuball et al. 2009; Kubo et al. 1989) providing the tracking principle for the presented work. This approach was further developed for the application in PET/CT by fragmentation, functionalizing and radiolabeling of the aTCRmu antibody. An overview of the genetic engineering of human T_{CM} and the tracking of these cells using the modified aTCRmu antibody is shown in Figure 2.

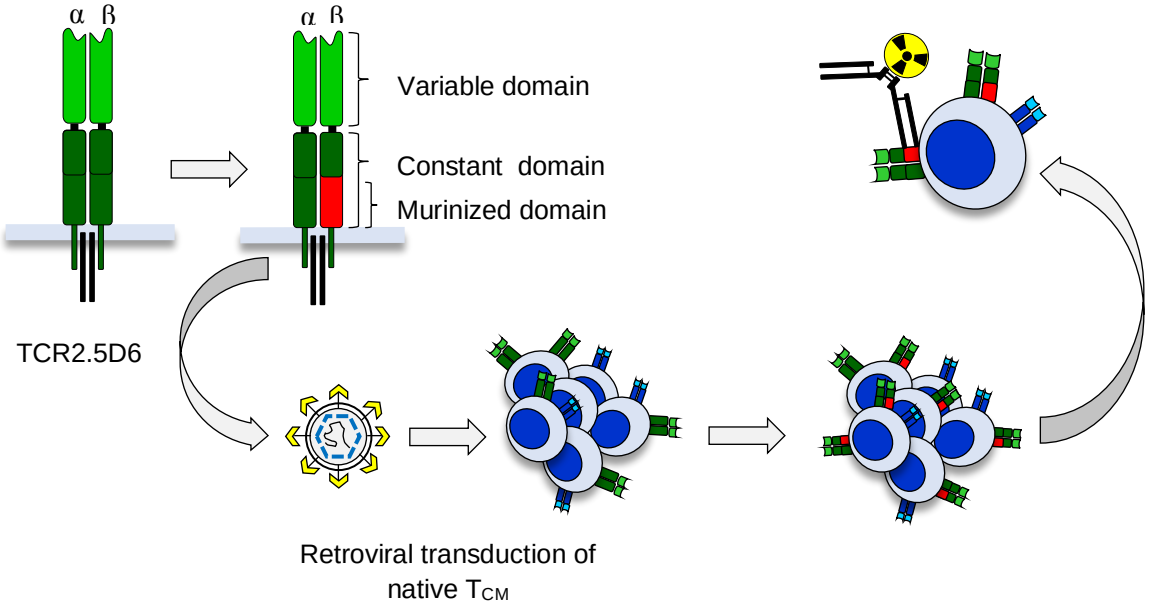

Figure 2. Tracking strategy of TCR2.5D6 T_{CM}.
The TCR2.5D6 harbors a murinized domain in the constant region of the TCRβ chain and was expressed in T_{CM} after retroviral transduction of native cells. The anti-TCRmu antibody or its fragments bind specifically to the introduced murine β domain. In order to use this approach in studies using Positron emission tomography (PET) as imaging modality, the aTCRmu-antibody or F(ab')$_2$ fragment was functionalized by chelator conjugation and radiolabeling.

5.2 GENERATION OF ^{89}ZR-DF-ATCRMU-IGG AND OF ^{89}ZR-DF-ATCRMU-F(AB')$_2$

For the visualization of transgene T cells *in vivo* we chose the imaging modality PET/CT for that the aTCRmu-antibody needed to be modified to serve as appropriate surrogate marker. The quality control (section 5.3) will be shown for both aTCRmu-IgG and aTCRmu-F(ab')$_2$ in comparison, however only aTCRmu-F(ab')$_2$ came into consideration for the application *in vivo*, as Mall et al. showed functional impact of aTCRmu-IgG on TCR2.5D6 T_{CM} *in vitro* as well as *in vivo* compared to its F(ab')$_2$ fragment (Mall et al. 2016). After the isolation of the aTCRmu-IgG from the hybridoma supernatant, the full antibody was digested to its F(ab')$_2$ fragment by Pepsin and purified via Protein A. The digest was confirmed by SDS-PAGE showing bands of 70 kDa (non-reducing conditions) and 20-25 kDa (reducing conditions) (Figure 3A) and SE-HPLC revealing a protein peak at later retention time (8.9 min) than the aTCRmu-IgG (8.1 min) (Figure 3B).

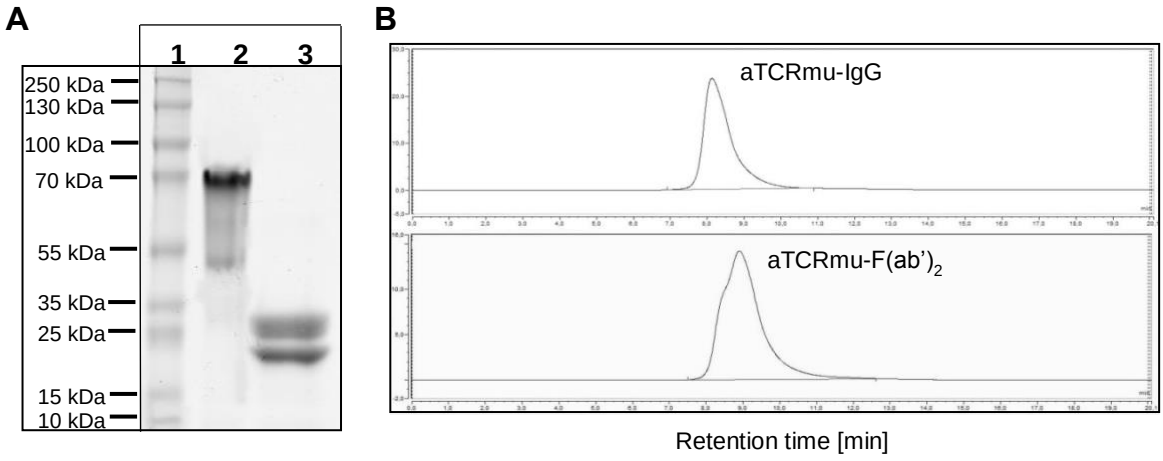

Figure 3. Quality control of the aTCRmu digestion to aTCRmu-F(ab')$_2$.

(A) SDS-PAGE and Coomassie staining of the aTCRmu-F(ab')$_2$ digest. Lane 1: protein marker from 10-250 kDa, lane 2: aTCRmu-F(ab')$_2$ under non-reducing conditions and lane 3 aTCRmu-F(ab')$_2$ fragments under reducing condition. (B) UV-profiles in SE-HPLC are depicted of the full aTCRmu antibody (upper graph) and the digested F(ab')$_2$ fragment (lower graph). UV signals are shown as mAU.

aTCRmu-IgG and F(ab')$_2$ were functionalized by attaching the bifunctional chelator p-Isothiocyanatobenzyl-desferrioxamine (Df-Bz-NCS) to lysine-NH_2 groups of the proteins followed by labeling with the radionuclide Zirconium-89 via trans-chelation from ^{89}Zr-oxalate according to the protocol of Vosjan et al. (Vosjan et al. 2010). An overview of the 2-step procedure is depicted in Figure 4.

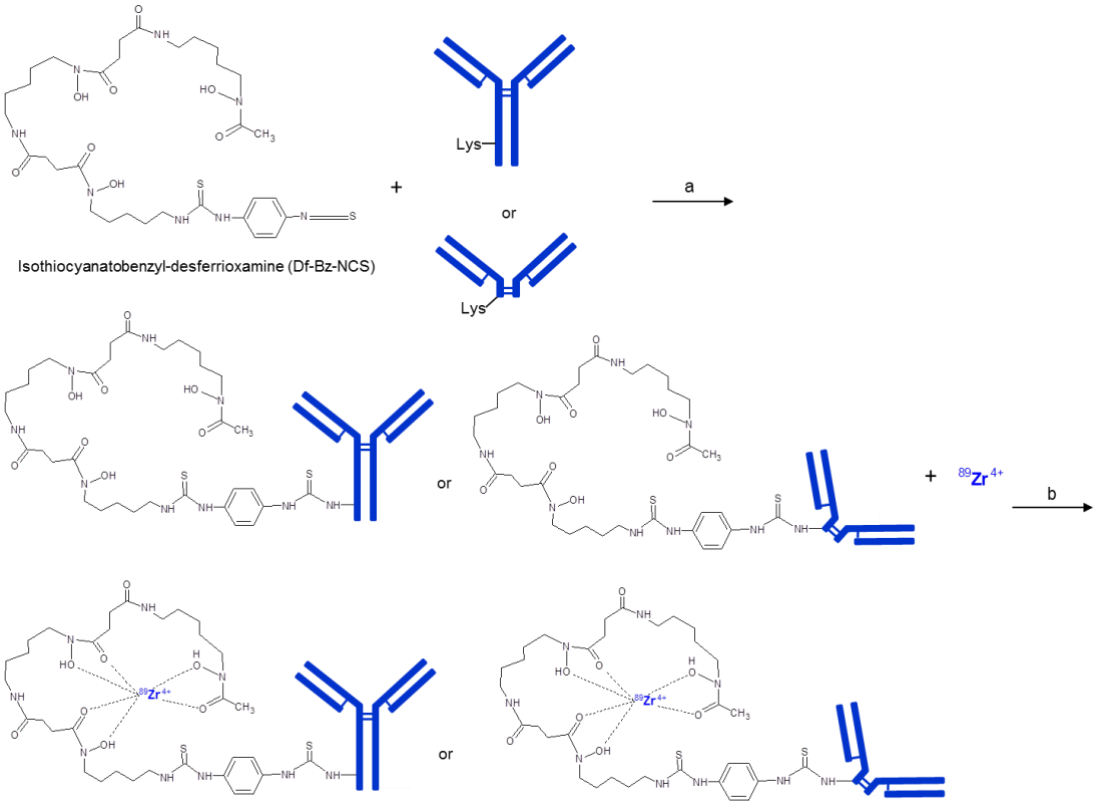

Figure 4. Functionalization and radiolabeling of aTCRmu-IgG or F(ab')$_2$.

Schematic overview of the 2-step radiotracer production, where aTCRmu-IgG or F(ab')$_2$ are conjugated with the bifunctional chelator Isothiocyanatobenzyl-desferrioxamine (Df-Bz-NCS) (a) with subsequent complexation of Zirconium-89 (b) (modified from Perk et al., 2010 (Perk et al. 2010)).

5.3 RADIOLABELING EFFICIENCY OF ^{89}ZR-DF-ATCRMU-IGG AND ^{89}ZR-DF-ATCRMU-F(AB')$_2$

After DFO-conjugation, the functionalized antibody or its fragment was labeled with ^{89}Zr to the radioimmunocomplexes ^{89}Zr-Df-aTCRmu-IgG or ^{89}Zr-Df-aTCRmu-F(ab')$_2$, which were investigated by radio-ITLC directly after reaction (Figure 5). Both DFO-conjugated proteins efficiently incorporated the radionuclide showing a distinct peak at R_f 0.0-0.2, while non-chelated free activity was absent (R_f > 0.4).

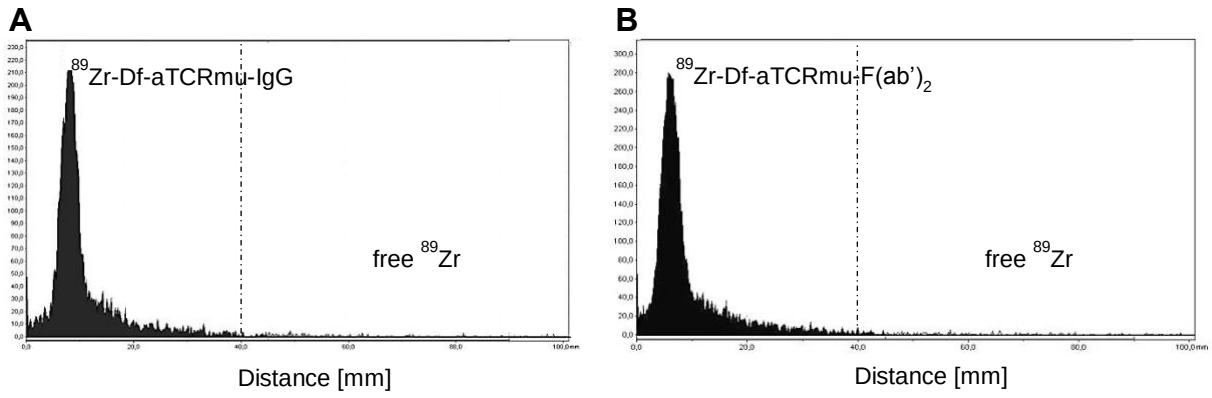

Figure 5. ITLC profiles of ^{89}Zr-Df-aTCRmu-IgG and ^{89}Zr-Df-aTCRmu-F(ab')$_2$ for quality control.

Profiles of ^{89}Zr-labeled Df-aTCRmu-IgG (A) and Df-aTCRmu-F(ab')$_2$ (B) analyzed by radio-ITLC.

Table 21 summarizes the radiolabeling yield, radiochemical purity (RCP) and specific activity (SA) of ^{89}Zr-Df-aTCRmu-IgG (n=15) and ^{89}Zr-Df-aTCRmu-F(ab')$_2$ (n=19) and indicate similar characteristics of both radiotracers.

	^{89}Zr-Df-aTCRmu-F(ab')$_2$	**^{89}Zr-Df-aTCRmu-IgG**
Radiolabeling yield	97.0 ± 2.1 %	97.9 – 0.6 %
Radiochemical purity	96.9 ± 2.1 %	97.6 – 0.9 %
Specific activity	7.0 ± 0.9 µCi/µg (259 ± 33.3 kBq/µg)	7.2 - 1.3 µCi/µg (266.4 ± 48.1 kBq/µg)

Table 21. Radiolabeling characteristics of ^{89}Zr-Df-aTCRmu-IgG/-F(ab')$_2$

5.4 IN VITRO CHARACTERIZATION OF ^{89}ZR-DF-ATCRMU-IGG AND ^{89}ZR-DF-ATCRMU-F(AB')$_2$

5.4.1 Immunoreactive fractions of ^{89}Zr-Df-aTCRmu-IgG and ^{89}Zr-Df-aTCRmu-F(ab')$_2$

As the modification of aTCRmu-IgG and F(ab')$_2$ by the chelator and the nuclide complexation may affect binding properties, hence appropriate antigen targeting, the immunoreactive fraction of both immunocomplexes were determined by *in vitro* tracer binding to cells in conditions representing infinite antigen excess according to the method described by Lindmo et al. (Lindmo et al. 1984). For the calculation, a double inverse plot of total bound activity applied over specific binding ([TB]/[SB]) as function of the inverse cell concentration (1/[cells]) was employed. Performing linear regression analysis, the intercept at the ordinate represented 1/r with r corresponding to the immunoreactive fraction of the total amount of radiotracer (Figure 6). After the radiolabeling procedure ^{89}Zr-Df-aTCRmu-IgG revealed an immunoreactive fraction of 88.3 ± 11.7 % (n=3) and ^{89}Zr-Df-aTCRmu-F(ab')$_2$ 93.7 ± 2.6 % (n=3).

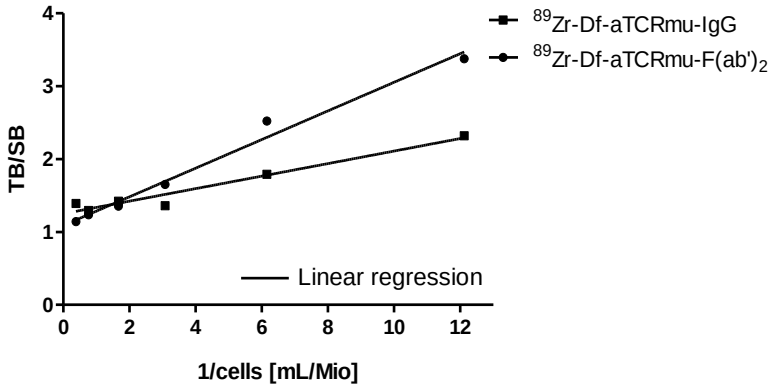

Figure 6. Determination of the immunoreactive fraction of ^{89}Zr-Df-aTCRmu-IgG and ^{89}Zr-Df-aTCRmu-F(ab')$_2$.

Representative graphs for the determination of the immunoreactive fractions for ^{89}Zr-Df-aTCRmu-IgG and ^{89}Zr-Df-aTCRmu-F(ab')$_2$. The linear regression analysis was applied in the double inverse plot of total bound activity to specific binding ([TB]/[SB]) as function of the inverse cell concentration (1/[cells]). The intercepts at the ordinate represent 1/r, where r=immunoreactive fraction.

5.4.2 Binding affinity ^{89}Zr-Df-aTCRmu-IgG and ^{89}Zr-Df-aTCRmu-F(ab')$_2$

A further hallmark for appropriate antigen targeting and unrestricted binding in contempt of chelator modification and radionuclide labeling, is the determination of the dissociation constant (K_d). Therefore, the affinity of the native markers aTCRmu-IgG/(F(ab')$_2$ to TCR2.5D6 transduced Jurkat76 cells were assessed by flow cytometry and the K_d values were obtained via non-linear regression of the Mean fluorescence intensity values (MFI) at the protein concentrations 1×10^{-12} – 5×10^{-7} M. aTCRmu-IgG revealed a K_d of 5.86×10^{-9} M and for aTCRmu-F(ab')$_2$ a K_d of 4.57×10^{-9} M was determined (Figure 7A). For the K_d evaluation of the ^{89}Zr labeled counterparts a TCR2.5D6 T_{CM} cell based binding test was applied in the radiotracer concentration range of 1×10^{-12} - 5×10^{-7} M. The obtained cpm values representing the bound radiotracer activity at each tracer concentration were analyses as well by non-linear regression and revealed K_d values in the nanomolar range of $4.04 \times 10^{-9} \pm 6.28 \times 10^{-10}$ M (n=3) for ^{89}Zr-Df-aTCRmu-IgG and $4.64 \pm 2.54 \times 10^{-9}$ M (n=3) for ^{89}Zr-Df-aTCRmu-F(ab')$_2$ (Figure 7B).

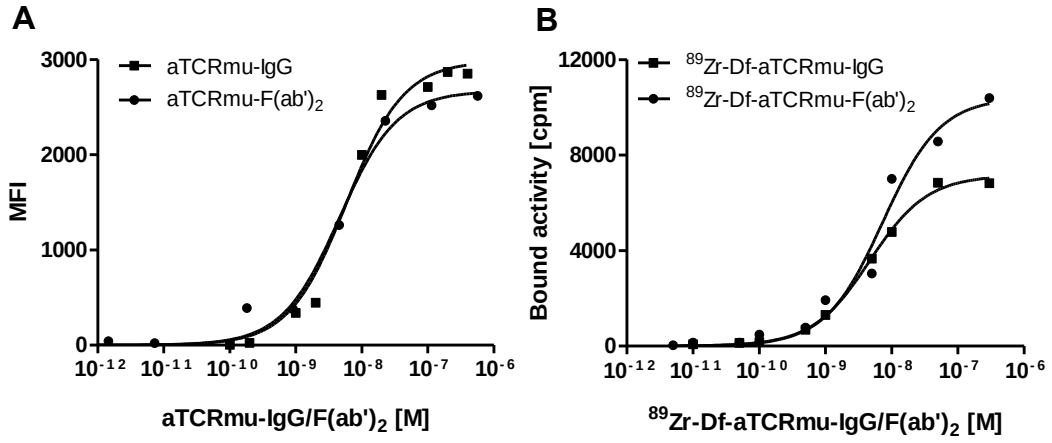

Figure 7. Binding affinity of aTCRmu-IgG/F(ab')$_2$ and ^{89}Zr-Df-aTCRmu-IgG/F(ab')$_2$ to TCR.2.5D6.
Representative logarithmic plots of affinity assays of aTCRmu-IgG/F(ab')$_2$ to TCR2.5D6 Jk76 cells via flow cytometry (A) and of ^{89}Zr-Df-aTCRmu-IgG/F(ab')$_2$ to TCR2.5D6 T_{CM} cells via gamma counting of bound radioactivity (B). The K_d values were determined by non-linear regression analysis.

5.4.3 Internalization of ^{89}Zr-Df-aTCRmu-IgG and ^{89}Zr-Df-aTCRmu-F(ab')$_2$ in TCR2.5D6 T_{CM}

After evaluating the binding abilities of the radiotracers, the cellular uptake was investigated in TCR2.5D6 T_{CM} cells. The internalization of the radiotracer may be crucial for the diagnostic purpose, where the retention of the compound may prolong residence time in the cells and allows accurate imaging. For the assessment of internalization, TCR2.5D6 T_{CM} cells were first incubated with the radiotracers for 1 h at 4 °C and after removal of excessive tracer for up to 240 min at 37 °C. In respective experiments and second group was additionally incubated with a 100-fold molar excess of unmodified aTCRmu-IgG for exclusion of non-specific binding. At indicated time points (5, 15, 30, 60, 120, 240 min) fractions of non-bound tracer (not shown), membrane bound and internalized activities were collected and measured. ^{89}Zr-Df-aTCRmu-IgG showed in the early time point of 5 min already internalized activity of 7.46 ± 2.23 % of initially bound tracer, while membrane bound activity reveals at that time highest membrane bound activity of 20.77 ± 3.63 % (Figure 8A). During the period of 240 min, the potion of internalized activity almost doubles to 12.07 ± 0.54 % while membrane bound activity drops over this time course to 12.1 ± 0.32 % of initial activity. Considering the total cell associated activity over 240 min, about 6.35 % of the compound was released to the supernatant representing the fraction of non-bound tracer (not shown). ^{89}Zr-Df-aTCRmu-F(ab')$_2$ showed a similar trend of internalization, however at lower levels over the whole time course, as maximal internalization rate totaled up to 7.1 ± 0.13 % of initially bound acitivty (Figure 8B). Likewise the total cell associated activity reached a lower level with maximum 18.08 ± 1.09 % in the initial phase releasing only 3.5 % to the supernatant over the time.

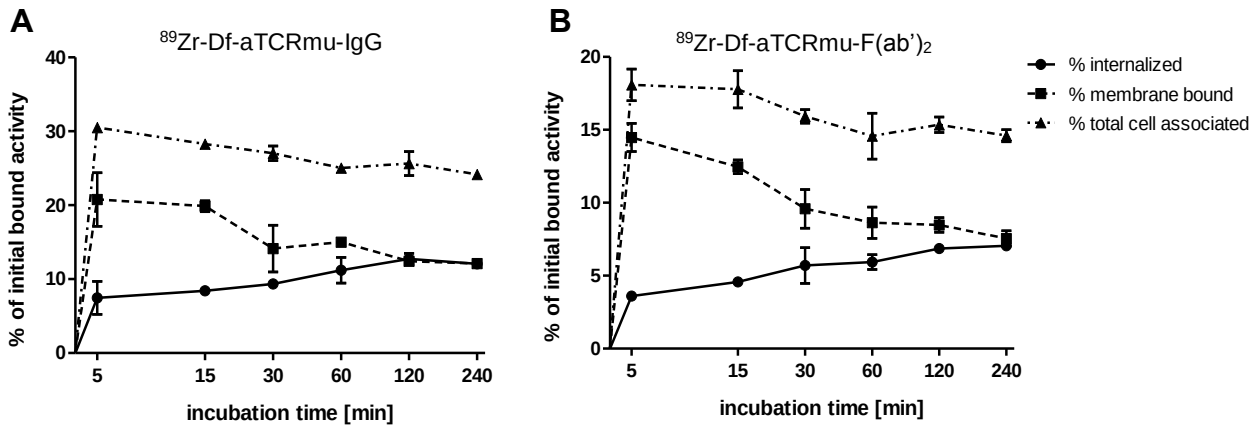

Figure 8. Internalization of ^{89}Zr-Df-aTCRmu-IgG and ^{89}Zr-Df-aTCRmu-F(ab')$_2$ in TCR2.5D6 T_{CM} cells.

Internalization assay of ^{89}Zr-Df-aTCRmu-IgG (A) ^{89}Zr-Df-aTCRmu-F(ab')$_2$ (B) in TCR2.5D6 T_{CM} over 240 min. TCR2.5D6 T_{CM} were incubated with 20 nM ^{89}Zr-Df-aTCRmu-IgG or ^{89}Zr-Df-aTCRmu-F(ab')$_2$ for indicated time points. Fractions representing membrane bound and internalized activity were collected and are shown as percentage (%) of initially bound activity. Total cell associated activity is presented as sum of internalized and membrane bound radiotracer. Mean ± SD of triplicates are shown.

5.4.4 In vitro and in vivo stability of ^{89}Zr-Df-aTCRmu-F(ab')$_2$

As impairment of T_{CM} functionality was observed after binding of aTCRmu-IgG (Mall et al. 2016), in further characterization studies for the application *in vivo* only ^{89}Zr-Df-aTCRmu-F(ab')$_2$ was investigated. *In vitro* stability of ^{89}Zr-Df-aTCRmu-F(ab')$_2$ was tested in human serum, PBS buffer (pH 7.0), the storage buffer sodium acetate/gentisic acid (pH 5.0), and DTPA (50 mM, pH 7.0) via radio-ITLC for up to 96 h at 37 °C (Figure 9A). Tracer incubated in human serum, PBS and sodium acetate/gentisic acid revealed a decrease of lower than 3.5 % in RCP over 4 days, whereas samples incubated in 50 mM DTPA pH 7.0 showed a decrease of protein bound activity to 21 % during the whole course of time due to its ability to competitively chelate $^{89}Zr^{4+}$. The high *in vitro* stability over several days showed suitable preconditions for the further *in vivo* application of ^{89}Zr-Df-aTCRmu-F(ab')$_2$. The *in vivo* stability of the tracer has been investigated after the intravenous application in NSG mice. For *ex vivo* assessment of intact tracer in blood, liver and kidneys, the tissues were taken

and homogenized at defined time points (6, 24 and 48 h) post injection and analyzed by SDS-PAGE and autoradiography with ^{89}Zr-Df-aTCRmu-F(ab')$_2$ solution as reference (Figure 9B). Beside of traces in liver and kidney due to incipient elimination, high levels of stable tracer were found in the blood pool during the first 6 h, which decreased over the next 24 and 48 h. Evaluating the signal intensity in areas of intact tracer in blood, liver and kidney, stability and decreasing presence over time of intact ^{89}Zr-Df-aTCRmu-F(ab')$_2$ could be confirmed (Figure 9C).

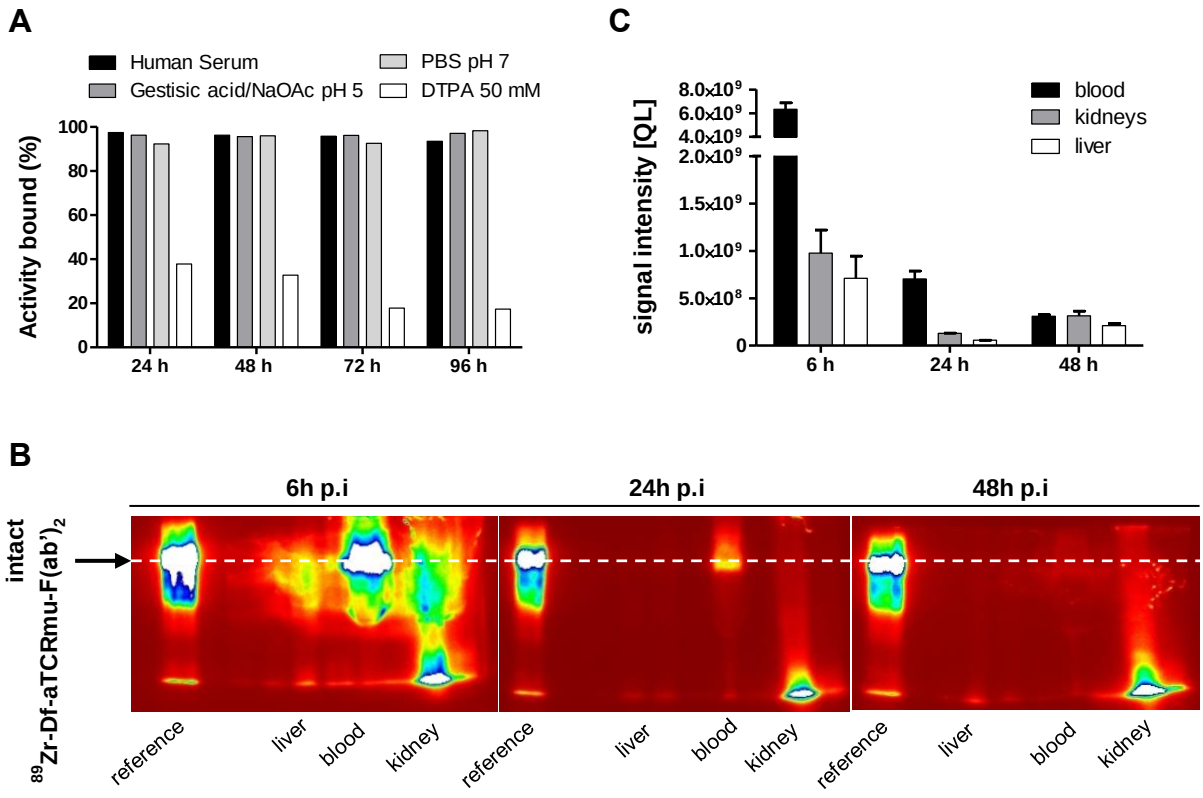

Figure 9. *In vitro* and *in vivo* stability of ^{89}Zr-Df-aTCRmu-F(ab')$_2$.
(A) *In vitro* evaluation of tracer stability in different media at indicated time points shown as percentage of bound activity after incubation. (B) Representative autoradiographs of SDS-PAGE gels of liver, blood and kidney homogenates of NSG mice injected i.v. with ^{89}Zr-Df-aTCRmu-F(ab')$_2$ and sacrificed 6 h, 24 h and 48 h post injection (n=3). Intact ^{89}Zr-Df-aTCRmu-F(ab')$_2$ is presented in the reference lane and areas of probe traces are indicated by the white dashed line. (C) In the autoradiographs signal intensities of ROIs present in areas of intact tracer were calculated and reported as quantum level values (QL).

5.5 FUNCTIONALITY OF T_{CM} AFTER ^{89}ZR-DF-ATCRMU-F(AB')$_2$ BINDING

5.5.1 IFN-γ release of T_{CM} after tracer binding

Using ^{89}Zr-Df-aTCRmu-F(ab')$_2$ *in vitro* or *in vivo* to bind and to track TCR transgenic T_{CM} raises the question, whether the tracer itself has an impact on functionality and viability of the cells. On one hand, direct binding of the antibody may cause altered cellular mechanisms, as shown for instance in case of antibody binding to CD2 or CD3 (Bromberg et al. 1991; Lin et al. 1996; Lin et al. 1995; Latinne et al. 1996). Moreover, some antibodies are even capable to induce apoptosis in terms of T cell depletion (Nizet et al. 1999; Macedo et al. 2012; Lundin et al. 2002). Mall et al. showed that after binding of aTCRmu-IgG at higher concentrations, cells respond with IFN-γ secretion and increased apoptosis (Mall et al. 2016), while these effects were absent for aTCRmu-F(ab')$_2$. Nevertheless, on the other hand the functionalization and radiolabeling with ^{89}Zr may constitute by its radiation a potential risk of functionality impairment, particularly after long-term exposure. Therefore TCR2.5D6 T_{CM} cells were assessed for IFN-γ secretion in presence of their target ML2-B7 directly after ^{89}Zr-Df-aTCRmu-F(ab')$_2$ binding at different concentrations (0 h) and 48 h after the exposure. The IFN-γ secretion in TCR2.5D6 T_{CM} was compared to the groups, where native aTCRmu-F(ab')$_2$ at different concentrations was added and the groups with ML2-B15 as target harboring the irrelevant HLA-molecule B15. The level of INF-γ secretion didn't differ between the groups being activated by ML2-B7 directly after labeling with ^{89}Zr-Df-aTCRmu-F(ab')$_2$ or non-radioactive aTCRmu-F(ab')$_2$ at all concentrations (Figure 10A). This could be also observed when the TCR2.5D6 T_{CM} cells were activated by ML2-B7 48 h after radioactive and non-radioactive tracer exposure (Figure 10B). This indicates, that radiation of ^{89}Zr, coupled at the highest concentration of 100 nM aTCRmu-F(ab')$_2$ (specific activity259 ± 33.3 kBq/µg) is not impairing the functionality of T_{CM} cells in the short term, but also after 48 h. Furthermore, IFN-γ haven't been released after co-incubation with ML2-B15 and tracer binding at both

time points, suggesting that the T_{CM} weren't activated by ^{89}Zr-Df-aTCRmu-F(ab')$_2$ in a non-specific way.

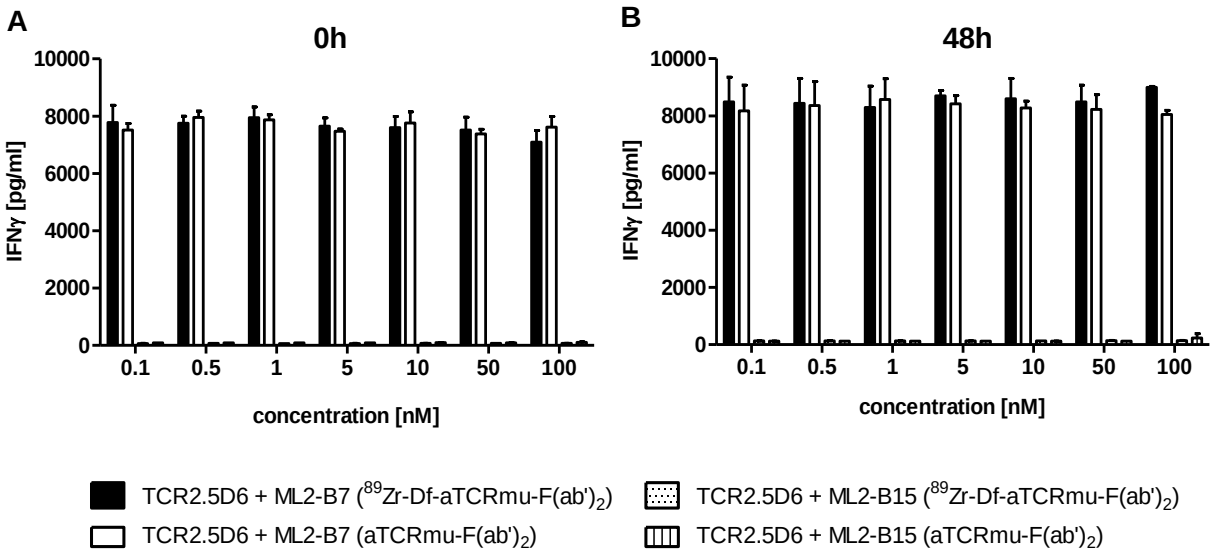

Figure 10. IFN-γ secretion of TCR2.5D6 T_{CM} after ^{89}Zr-Df-aTCRmu-F(ab')$_2$/ aTCRmu-F(ab')$_2$ binding and co-cultivation with ML2-B7/ML2-B15 cells.

Co-incubation of TCR2.5D6 T_{CM} and ML2-B7 or ML2-B15 tumor cells was performed either directly (0 h) (A) or 48 h (B) after binding of ^{89}Zr-Df-aTCRmu-F(ab')$_2$ or non-radioactive aTCRmu-F(ab')$_2$ at indicated concentrations. (A-B) Co-cultivation with ML2-B15 cells harboring an irrelevant HLA-molecule (B15) served as negative control for non-specific activation. Mean ±SD of triplicates is depicted.

5.5.2 γH2AX expression and apoptosis in T_{CM} after tracer binding in vitro and in vivo

In order to further evaluate the impact of radiation deriving from the radiotracer during T_{CM} binding, the cells were investigated on DNA level regarding induced double-strand breaks (DSB), which were characterized by the detection of the phosphorylated form of the histone γH2AX (Rogakou et al. 1998). Cells being viable and functional can repair DSB caused by ionizing radiation within the first 30 to 60 min (Schmid et al. 2010; Lomax, Folkes, and O'Neill 2013), however at high radiation doses a fraction of DSB persist and cause enhanced cell death. To evaluate the γH2AX expression in TCR-transgenic T cells at different activities, 0

to 1000 µCi (0.0 to 37.0 MBq) ^{89}Zr-Df-aTCRmu-F(ab')$_2$ were incubated for 1 h with TCR2.5D6 T_{CM}. The cells were then assessed for γH2AX expression and cell death via EMA staining directly after radiotracer binding and after 48 h of regeneration time to investigate long-term effects of the radiation. Directly after radiotracer co-incubation at 200 µCi, 6.1 ± 4.7 % of the cells expressed γH2AX being at an elevated level compared to the normalized non-radiated control group (0 µCi) and lower activities. The portions of γH2AX expressing cells increased at higher activities (500 and 1000 µCi) with 12.7 ± 3.1 % or 27.7 ± 13.5 %, respectively. In contrast, γH2AX formation couldn't be detected at any activity in the group investigated 48 h post exposure (Figure 11A). Dead cell staining revealed no elevated levels at any activity in the group being investigated directly after radiotracer binding. On the other hand, cells exposed to tracer activities higher than 500 µCi resulted after 48 h in 4 to 5 times more dead cells than the normalized level of the non-radiated sample group (Figure 11B). This indicates that T_{CM} are affected by higher doses of ^{89}Zr deriving radiation and can't repair damages on DNA level resulting in cell death over the long term.

The expression of γH2AX in TCR-transgenic T_{CM} was further assessed *ex vivo* after the i.v. administration of TCR2.5D6 T_{CM} cells and ^{89}Zr-Df-aTCRmu-F(ab')$_2$ (imaging dose 20 µg corresponding to 2.2 MBq) in ML2-B7 tumor bearing NSG mice. The tumors were dissected 48 h post radiotracer injection and IHC analysis was performed on consecutive slices for CD3 to distinguish infiltrated T cells from the tumor tissue, γH2AX for the determination of DSB in these T cells and cleaved Caspase 3 to evaluate apoptosis in potentially damaged T cells. In both animal groups, receiving tracer and no tracer, tumor-infiltrating T cells were detected (CD3; Figure 11C). The areas with detected T cells didn't show any significant γH2AX expression in the animal group injected with activity as shown for the non-radioactive control group. Consequently, these cells weren't positive for cleaved Caspase 3 in both groups, although the surrounding tumor tissue revealed high levels of activated Caspase 3, which is typical for various cancer cell types (Hu et al. 2014; Liu et al. 2017). In conclusion, it

has been shown that ^{89}Zr-Df-aTCRmu-F(ab')$_2$ doesn't have damaging effects on DNA level of T_{CM} in activity ranges used for further *in vivo* applications (2.2 MBq).

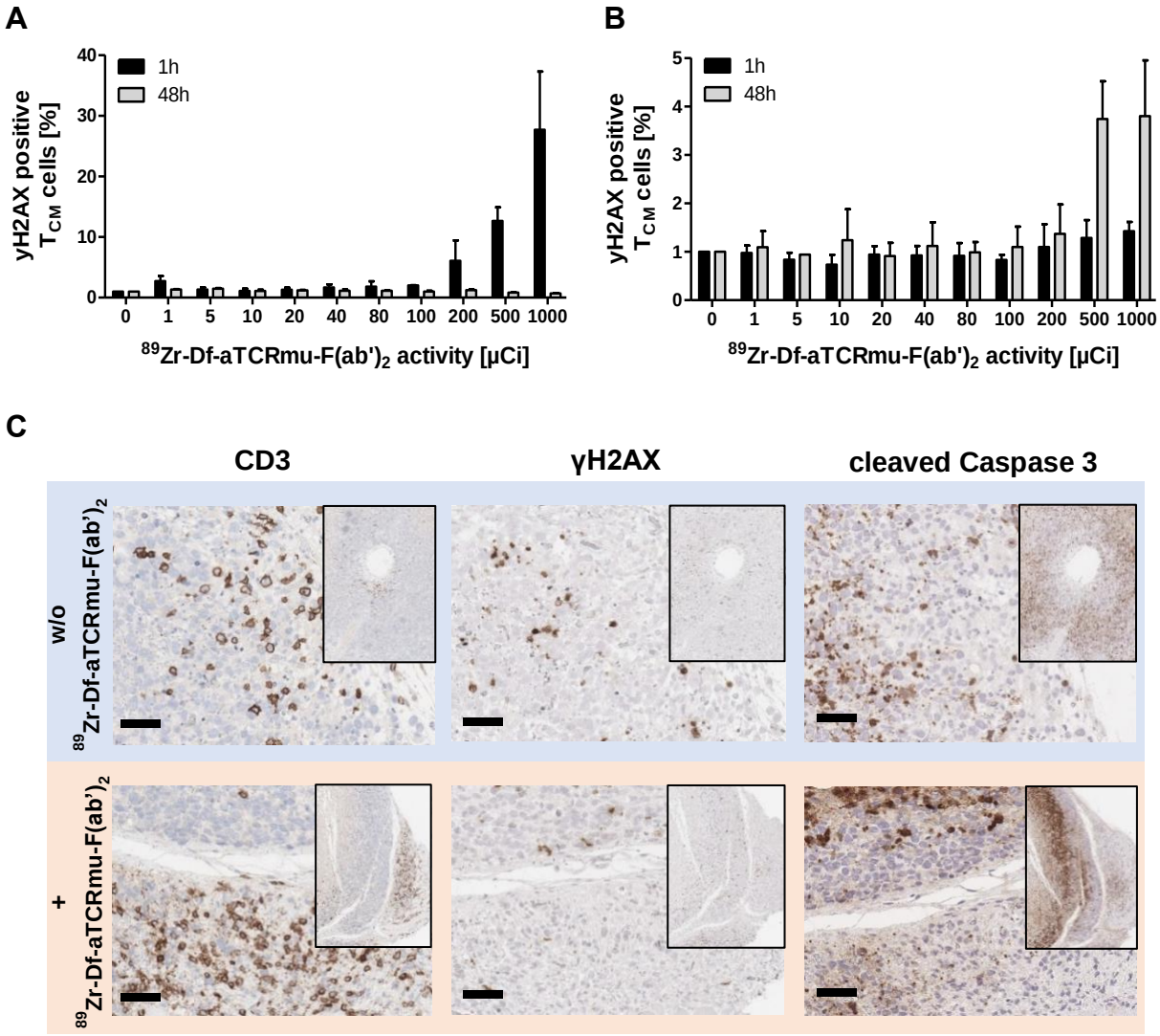

Figure 11. Influence of ^{89}Zr-Df-aTCRmu-F(ab')$_2$ radiation on TCR2.5D6 T_{CM} cells *in vitro* and *in vivo*.

(A) Percentage of γH2AX-positive TCR2.5D6 T_{CM} cells 1 h and 48 h after exposure to 0 to 1000 µCi (0.0 to 37.0 MBq) of ^{89}Zr-Df-aTCRmu-F(ab')$_2$. Mean ± SD of triplicates are shown. (B) Percentage of EMA-positive (dead) TCR2.5D6 T_{CM} cells, measured 1 h and 48 h after radiotracer exposure at activities 0 to 1000 µCi (0.0 to 37.0 MBq). Mean ± SD of triplicates are shown. (C) Consecutive IHC analysis of TCR2.5D6 T_{CM} infiltrated ML2-B7 tumors after 48 h of exposure to 2.2 ± 0.1 MBq i.v. injected ^{89}Zr-Df-aTCRmu-F(ab')$_2$. Representative IHC stainings against anti-human-CD3, γH2AX and cleaved Caspase-3 of T-cell infiltrated ML2-B7 tumor tissues of animals injected with radiotracer (lower panel; n=4) and no activity as control group (upper panel; n=2). Magnification 20X, scale bars equal to 50 µm.

5.6 IN VIVO TRACKING OF TCR-TRANSDUCED HUMAN T CELLS BY ^{89}ZR-DF-ATCRMU-F(AB')$_2$ VIA PET/CT

After evaluating the suitability of ^{89}Zr-Df-aTCRmu-F(ab')$_2$ to bind and track TCR-transgenic T cells *in vitro* and *in vivo*, the tracer was intended for the further application in a pre-clinical setting. Dr. Sabine Mall developed an experimental setting with tumor-bearing NSG mice, where adoptive T-cell transfer and tracer administration is simulated for final PET/CT imaging and *ex vivo* analyses. The setup is shown in Figure 12A, where ML2-B7 (right flank) and ML2-B15 (left flank) tumor bearing NSG mice received TCR2.5D6-transduced or native T_{CM} as described in section 4.12.2. Mall et al. investigated in several experiments the optimal imaging time point after radiotracer application, where the best signal to background ratio was achieved 48 h post injection (Mall et al. 2016). Two days after T-cell transfer, ^{89}Zr-Df-aTCRmu-F(ab')$_2$ was injected and PET/CT was performed 48 h later (Figure 12B). A distinct signal was detectable at the ML2-B7 tumor in mice treated with TCR2.5D6 $T_{CM,}$ while at the ML2-WT tumor site no signal was observed. In the control groups, where non-transduced T_{CM} or only PBS were injected no specific signal was detected on both tumor sites being indicative for lacking non-specific binding to T cells and tissues. Image-based ROI analysis of the signal at ML2-B7 corresponded to the strong PET signal in comparison to ML2-WT and both tumors in groups injected with non-transduced T_{CM} or PBS (Figure 12C). The *ex vivo* biodistribution analysis of diverse organs and the tumor tissues confirmed the elevated activity accumulation as well in ML2-B7 tumors in TCR2.5D6 T_{CM} administered animals, then in the control tumor and tumors of the control groups (Figure 12D). Higher activity accumulation was also observed in spleen and lung of TCR2.5D6 T_{CM} treated animals, while activity levels in other groups and tissues were on similar levels. Autoradiography of tumor tissues and selected organs further supported these findings (Figure 12E). Normalizing the activity enrichment in the biodistribution to the blood level, also the tumor/organ to blood ratio revealed significant differences in ML2-B7 tumors, spleen and liver in TCR2.5D6 T_{CM} injected mice compared to ML2-WT and the control groups (Figure 12F).

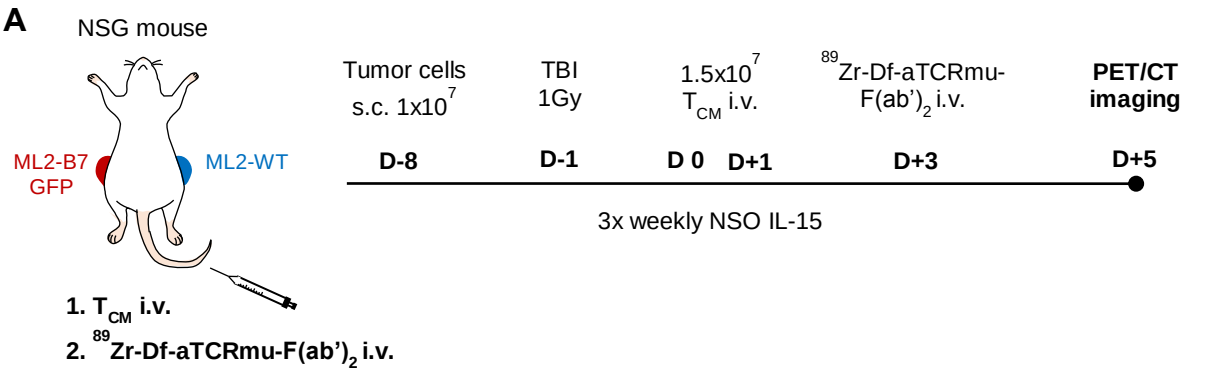
A
NSG mouse
ML2-B7
GFP
ML2-WT
Tumor cells
s.c. 1x10^7
TBI
1Gy
1.5x10^7
T_CM i.v.
89Zr-Df-aTCRmu-
F(ab')2 i.v.
PET/CT
imaging
D-8
D-1
D 0
D+1
D+3
D+5
3x weekly NSO IL-15
1. T_CM i.v.
2. 89Zr-Df-aTCRmu-F(ab')2 i.v.

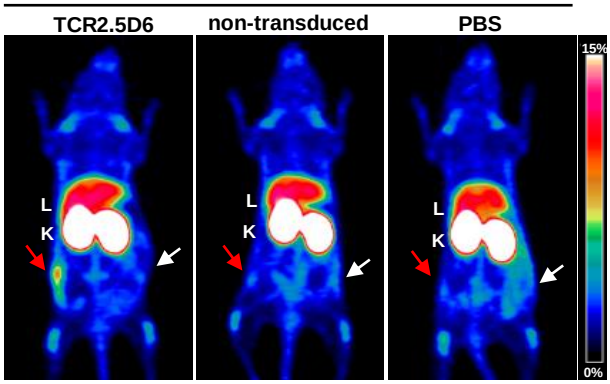
B
TCR2.5D6
non-transduced
PBS
L
K
15%
0%

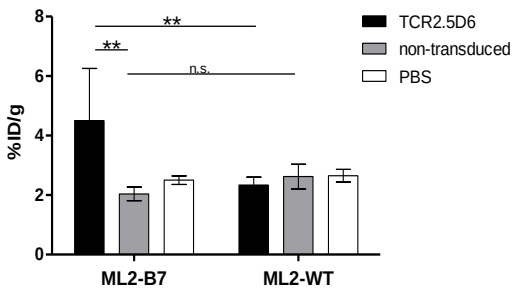
C
%ID/g
ML2-B7
ML2-WT
TCR2.5D6
non-transduced
PBS
**
n.s.

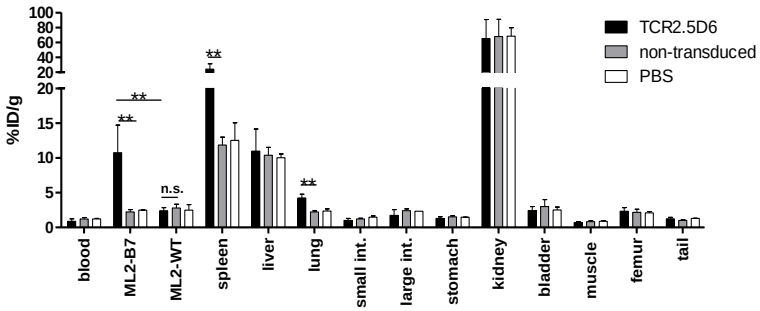
D
%ID/g
blood
ML2-B7
ML2-WT
spleen
liver
lung
small int.
large int.
stomach
kidney
bladder
muscle
femur
tail
TCR2.5D6
non-transduced
PBS

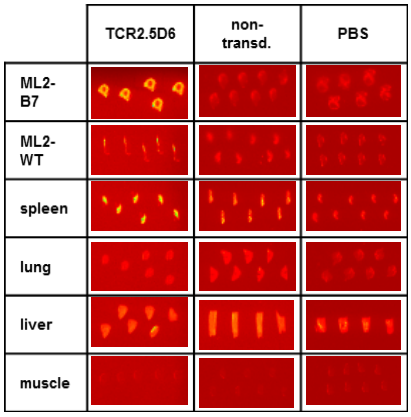
E
TCR2.5D6
non-transd.
PBS
ML2-B7
ML2-WT
spleen
lung
liver
muscle

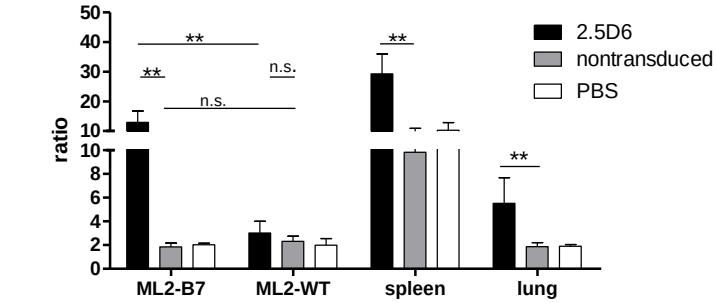
F
ratio
ML2-B7
ML2-WT
spleen
lung
2.5D6
nontransduced
PBS
**
n.s.

Figure 12. PET/CT imaging of i.v. injected TCR2.5D6 T_{CM} in ML2-B7 tumors by ^{89}Zr-Df-aTCRmu-F(ab')$_2$.

(A) Experimental setting: NSG mice were injected s.c. with 1 x 10^7 ML2-B7 (right flank) and ML2-WT tumor cells (left flank) followed by total body irradiation (TBI) with 1 Gy one week later and adoptive transfer of 1.5 x 10^7 TCR2.5D6 T_{CM}, non-transduced T_{CM} or PBS over two subsequent days i.v.. IL-15 producing NSO cells were injected 3 times i.p. during the week to support T-cell engraftment. ^{89}Zr-Df-aTCRmu-F(ab')$_2$ was administered i.v. two days later and PET/CT imaging was performed after further 48 h. (B) Representative 3D PET (MIP) images 48 h post ^{89}Zr-Df-aTCRmu-F(ab')$_2$ injection of the animal groups treated with TCR2.5D6 T_{CM}, non-transduced T_{CM} or PBS. Red arrows show the ML2-B7 tumors, while white arrows indicate the control tumor ML2-WT. Scale bar = 0-15 %ID/g; L=Liver; K=Kidney. (C) Image based quantitative analysis of PET signals of ML2-B7 and ML2-WT tumors in the animal groups treated with TCR2.5D6 T_{CM}, non-transduced T_{CM} or PBS. Mean ± SD of %ID/g of the ROI in the tumor is depicted for n=5 animals treated with T_{CM} and n=2 treated with PBS. Mann-Whitney test: **p<0.01. (D) Biodistribution analysis of activity accumulation in selected organs and tumor tissues 48 h post tracer injection. Mean %ID/g ± SD is depicted for n=5 animals treated with T_{CM} and n=2 treated with PBS. Mann-Whitney test: *p<0.05. (E) Representative slices of selected tissues after autoradiography in the animal groups treated with TCR2.5D6 T_{CM}, non-transduced T_{CM} or PBS. (F) Quantitative evaluation of tumor/organ to blood ratios 48 h post ^{89}Zr-Df-aTCRmu-F(ab')$_2$ injection. Mean ± SD of %ID/g ratio is depicted for n=5 animals treated with T_{CM} and n=2 treated with PBS. Mann-Whitney test: **p<0.01. (B-F) Representative data of one out of three experiments are shown. Data evaluations have been performed by Dr. Sabine Mall, III. Medical department, Klinikum rechts der Isar.

In addition to the demonstration of specific PET signal and tracer uptake in the target tumor as shown in Figure 12B-F, the confirmation of T-cell presence in indicated tissue was of great importance. Therefore, further *ex vivo* analyses (data not shown) were performed by Mall et al. (Mall et al. 2016) proving elevated presence of TCR2.5D6 T_{CM} in tissues, particularly in ML2-B7 tumors, where high activity accumulation was found. These findings were conducted by flow cytometry and immunohistochemistry focusing on specific T-cell marker and qPCR, where genomic DNA of the TCRmu-sequence was analyzed. These *ex vivo* approaches, confirming corresponding tracer uptake and TCR2.5D6 T_{CM} cell presence, support accuracy the PET data providing specific imaging of engrafted T cells *in vivo* in the described animal model. This specific methodology using ^{89}Zr-Df-aTCRmu-F(ab')$_2$ as surrogate marker can be applied for further *in vivo* investigations in the pre-clinical model.

5.7 EVALUATION OF THE DETECTION LIMIT USING IN VITRO LABELED TRANSGENIC T CELLS IN PET/CT

After investigating the accuracy of the developed imaging strategy, the specific *in vivo* detection of transgenic T cells brings up the question of the sensitivity of this method in the presented experimental setting. For a potential clinical translation, this question may help to gauge the potential of this methodology for T-cell tracking in T-cell based immunotherapy in different tissues and stages. Therefore, sensitivity needed to be evaluated in terms of lowest number of transgenic T-cells being detectable by the tracking method in the described setting. Before assessing the detection limit after adoptive T-cell transfer and T-cell engraftment *in vivo*, a pre-model should provide information about the minimum number of ^{89}Zr-Df-aTCRmu-F(ab')$_2$ labeled TCR2.5D6 T_{CM} cells detectable in small animal PET. To this purpose, serial 1:2 dilutions of tracer labeled TCR2.5D6 T_{CM} have been prepared and subcutaneously co-injected with Matrigel™. First, after *in vitro* incubation with an excess of ^{89}Zr-Df-aTCRmu-F(ab')$_2$, the labeled TCR2.5D6 T_{CM} showed blocking of the binding sites by the tracer in comparison to non-labeled TCR2.5D6 T_{CM}, when stained for aTCRmu (Figure 13A). By counting the associated activity of the pellets of labeled TCR2.5D6 T_{CM} cells, the proper dilution was confirmed, while non-transduced cells didn't reveal specifically associated activity, as was expected (Figure 13B).

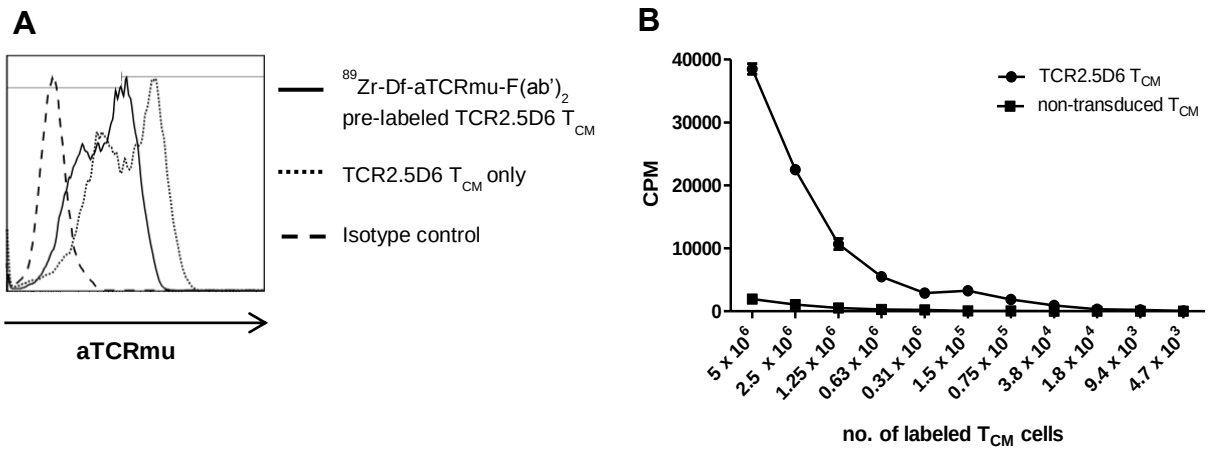

Figure 13. *In vitro* labeling of TCR2.5D6 iRFP TCM by ^{89}Zr-Df- aTCRmu-F(ab')$_2$.
(A) Flow cytometry anti-TCRmu staining of TCR2.5D6 T_{CM} pre-labeled with ^{89}Zr-Df-aTCRmu-F(ab')$_2$ (solid line) and non-labeled TCR2.5D6 T_{CM} (dotted line). Isotype control on TCR2.5D6 T_{CM} (dashed line). (B) Counts per minute (CPM) of ^{89}Zr-Df-aTCRmu-F(ab')$_2$ labeled and serially diluted TCR2.5D6 T_{CM} (n=3) and non-transduced T_{CM} (n=2) being used for s.c. injection of NSG mice and PET/CT imaging. cpm are shown as mean ± SD.

PET/CT images of animals in the first group injected with 5×10^6 to 1.5×10^5 cell spots, showed prominent signals to the lowest dilution of 1.5×10^5 labeled TCR2.5D6 T_{CM} (Figure 14AI). The group injected with labeled non-transduced T_{CM} showed only non-specific background signals due to residual non-specific binding of the radiotracer to the T_{CM}, when higher cell numbers (>1.25×10^6) were inoculated. Furthermore, the visible image noise is associated to the low number of acquired events, being related to the low activities in the pellets. PET images of the second group, receiving further dilutions from 1.5×10^5 to 4.7×10^3 labeled TCR2.5D6 T_{CM}, indicate a detection limit of approximately 1.8×10^4 *in vitro* labeled cells. The control group did not reveal any non-specific signal in this dilution range (Figure 14AII). Image-based activity quantification of the cell spots (ROIs) supported the findings of steady decrease of activity in TCR2.5D6 T_{CM} spots in both dilution groups Figure 14B).

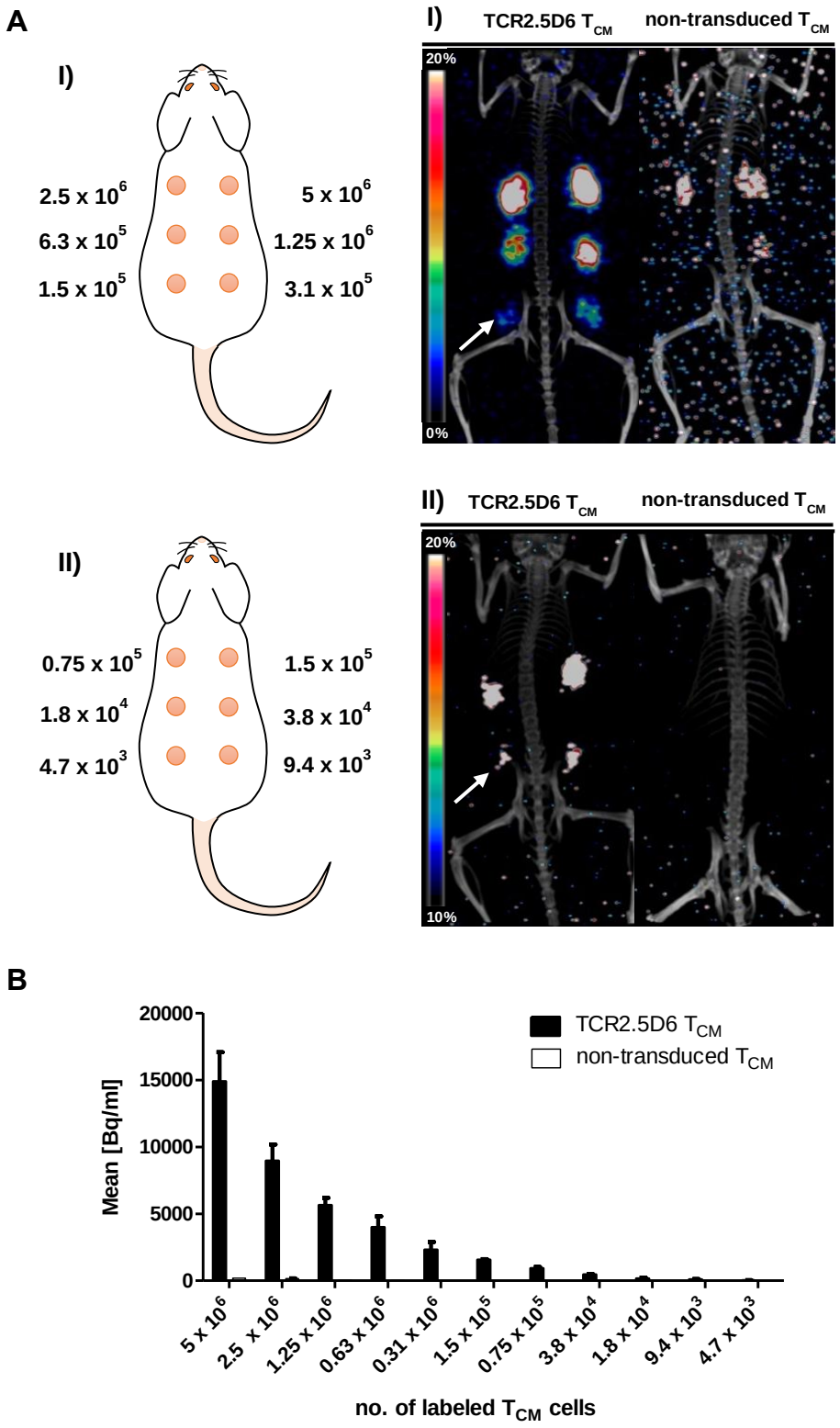

Figure 14. Detection limit of *in vitro* ^{89}Zr-Df-aTCRmu-F(ab')$_2$-labeled TCR2.5D6 T_{CM} by small animal PET/CT

(A) *In vitro* ^{89}Zr-Df-aTCRmu-F(ab')$_2$ labeled TCR2.5D6 T_{CM} and non-transduced T_{CM} were s.c. co-injected with Matrigel™ in mice in dilutions ranging from 5 x 10^6 to 1.5 x 10^5 (group I) and 1.5 x 10^5 to 4.7 x 10^3 (group II) The representative 3D-PET/CT Maximum Imaging Projection (MIP) images are

shown at the scale 0-20 % of injected dose per gram (%ID/g) for group I and 10-20 % of %ID/g for group II to allow exclusion of noise signals. White arrows indicate the highest dilution of detectable TCR2.5D6 T_{CM} in respective group. (B) Image based quantitative analysis of the cell spots (ROIs) shown as mean activity (Bq/ml) ± SD. (A-B) One representative PET/CT image of mice injected with tracer labeled TCR2.5D6 T_{CM} (n=3) in group (I) and group (II) and with non-transduced T_{CM} (n=2) in both groups is shown. Data of one out of two experiments are shown for both groups.

5.8 DETECTION LIMIT OF I.V. TRANSFERRED T CELLS IN PET/CT

5.8.1 Workflow in vivo and ex vivo for setting of the detection limit

After evaluating the sensitivity of the small animal PET device for detection of the lowest number of tracer labeled transduced T_{CM}, the aim was to find an estimation for the detection limit in the clinically relevant model described in section 5.6. To this purpose, groups of ML2-B7 and ML2-B15 bearing mice were injected i.v. with different numbers of TCR2.5D6 T_{CM} ranging from 3×10^6 to 3×10^5 transduced T cells. PET images were acquired five days after T-cell transfer and two days after ^{89}Zr-Df-aTCRmu-F(ab')$_2$ administration, followed by *ex vivo* analysis of the tumors (Figure 15A). To determine *ex vivo* the amount of infiltrated transduced T cells with the aid of quantification beads via flow cytometry, TCR2.5D6 T_{CM} cells needed to be distinguished in the single cell suspensions from ML2-B7 or ML2-B15 tumor cells. Therefore, the T_{CM} were transduced with the TCR2.5D6 gene additionally linked to the iRFP gene (TCR2.5D6 iRFP T_{CM}) (Figure 15B). The introduced HLA genes in the ML2 cell lines B7 or the irrelevant HLA-B15 were additionally expressing GFP (Figure 15C). In this way, the flow cytometric boundary of TCR2.5D6 iRFP T_{CM} is performed by the gating sequence shown in Figure 15D.

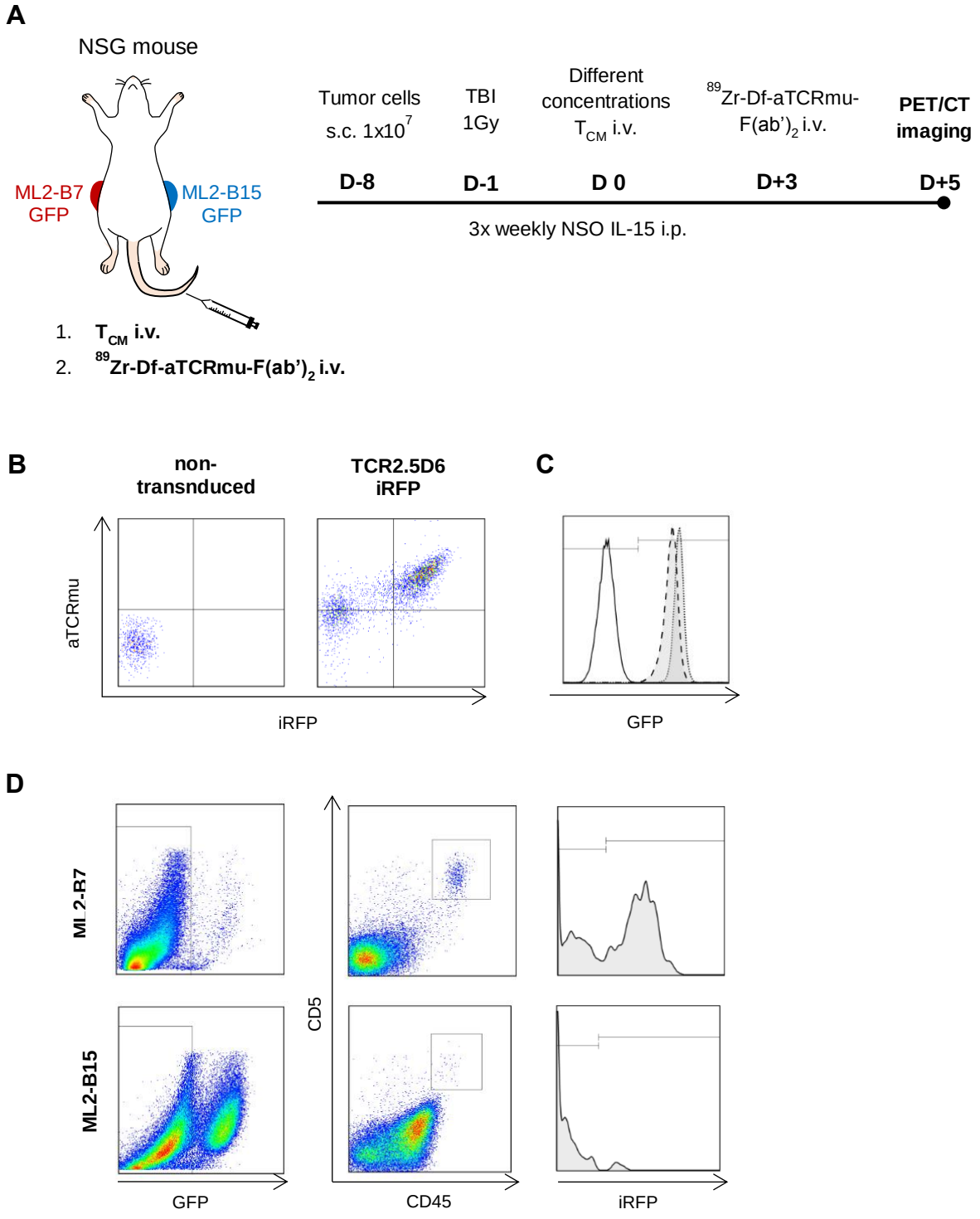

Figure 15. Workflows *in vivo* and *ex vivo* for the estimation of the detection limit of TCR2.5D6 iRFP T_{CM} after intravenious transfer.

(A) Experimental setting: NSG mice were injected s.c. with 1 x 10^7 ML2-B7 (right flank) and ML2-WT tumor cells (left flank) followed by total body irradiation (TBI) with 1 Gy one week later and adoptive transfer of different numbers of TCR2.5D6 iRFP T_{CM} or non-transduced T_{CM} (control group) i.v. IL-15 producing NSO cells were injected 3 times i.p. during the week to support T-cell engraftment. ^{89}Zr-

Df-aTCRmu-F(ab')$_2$ was administered i.v. three days later and PET/CT imaging was performed after further 48 h. (B) Expression of TCR2.5D6 (aTCRmu) and iRFP of non-transduced T_{CM} (left plot) and TCR2.5D6 iRFP T_{CM} (right plot) used for the experimental setting. (C) GFP expression of ML2-B7 (dotted line) and ML2-B15 (dashed line) compared to ML2-WT (solid line). (D) Gating sequence of single cell suspensions of T-cell infiltrated ML2-B7 (top row) and ML2-B15 tumors (lower row). Cells were pre-gated for vital cells and were excluded from GFP expressing tumor cells (left panel), followed by gating for hCD5+hCD45+ cells (middle panel) and TCR2.5D6 transduced T cells were determined within the GFP-hCD5+hCD45+ T-cell population by their iRFP expression (right panel). (B-D) Representative dot plots and histograms of flow cytometry analyses are shown.

5.8.2 In vivo and ex vivo quantification of engrafted TCR2.5D6 iRFP T_{CM} at the tumor site

In the initial experiment groups of ML2-B7 and ML2-B15 tumor bearing NSG mice were i.v. transferred with 3×10^6 (I), 1.5×10^6 (II),0.6×10^6 (III) and 0.3×10^6 (IV) TCR2.5D6 iRFP expressing $T_{CM,}$ while an additional control group received 5×10^6 non-transduced T_{CM}. After tracer injection and PET/CT acquisition a prominent signal was detected the ML2-B7 tumor site, receiving the highest T-cell number and showing strongest T-cell engraftment (Figure 16A, I). Signal intensity at the target tumor site decreased with the next injected T-cell concentration, presumably involving lowered T-cell engraftment (Figure 16A, II). Animals receiving lower T-cell concentrations (III-IV) revealed very low PET-signals at ML2-B7 indistinguishable from signals acquired at ML2-B15 or at tumors sites in the control group injected with non-transduced $T_{CM.}$ High T-cell associated tracer accumulation in ML2-B7 tumors of group I was confirmed by *ex vivo* gamma-counting with 6.55 ± 1.24 %ID/g (Figure 16B) and a tumor-to-blood ratio of 12.41 ± 2.29 (Figure 16C), compared to ML2-B15 showing only 2.9 ± 0.64 %ID/g and a ratio of 1.53 ± 0.35, respectively. Activities were decreasing with every administered T-cell concentration comparable to levels of the ML2-B15 tumor or the control group at < 2.1 %ID/g and tumor-to-blood ratios around 3.82. In flow cytometric analysis high portions of hCD5+hCD45+iRFP+ expressing cells were found in ML2-B7 tumors of group I, decreasing with every administered T-cell concentration (Figure 16D). *Ex*

vivo quantification of the absolute number of infiltrated transgenic T cells in the whole tumor tissues revealed22419 ± 2139 TCR2.5D6 iRFP T_{CM} cells in ML2-B7 tumors in group I, which is associated with a strong PET signal and high activity accumulation (%ID/g) (Figure 16E).15227 ± 2036 2139 TCR2.5D6 iRFP T_{CM} cells were determined in group II providing a marginal signal in PET. In further groups, less transgenic T-cells were found, which was associated with decreasing activity accumulation and lacking specific signal. Similarly, to the detection limit of *in vitro* tracer labeled TCR2.5D6 T_{CM} cells (section 5.7), imagings in this experimental setting approach values of approximately 1.0×10^4 to 2.0 x 104 *ex vivo* determined transgenic T cells.

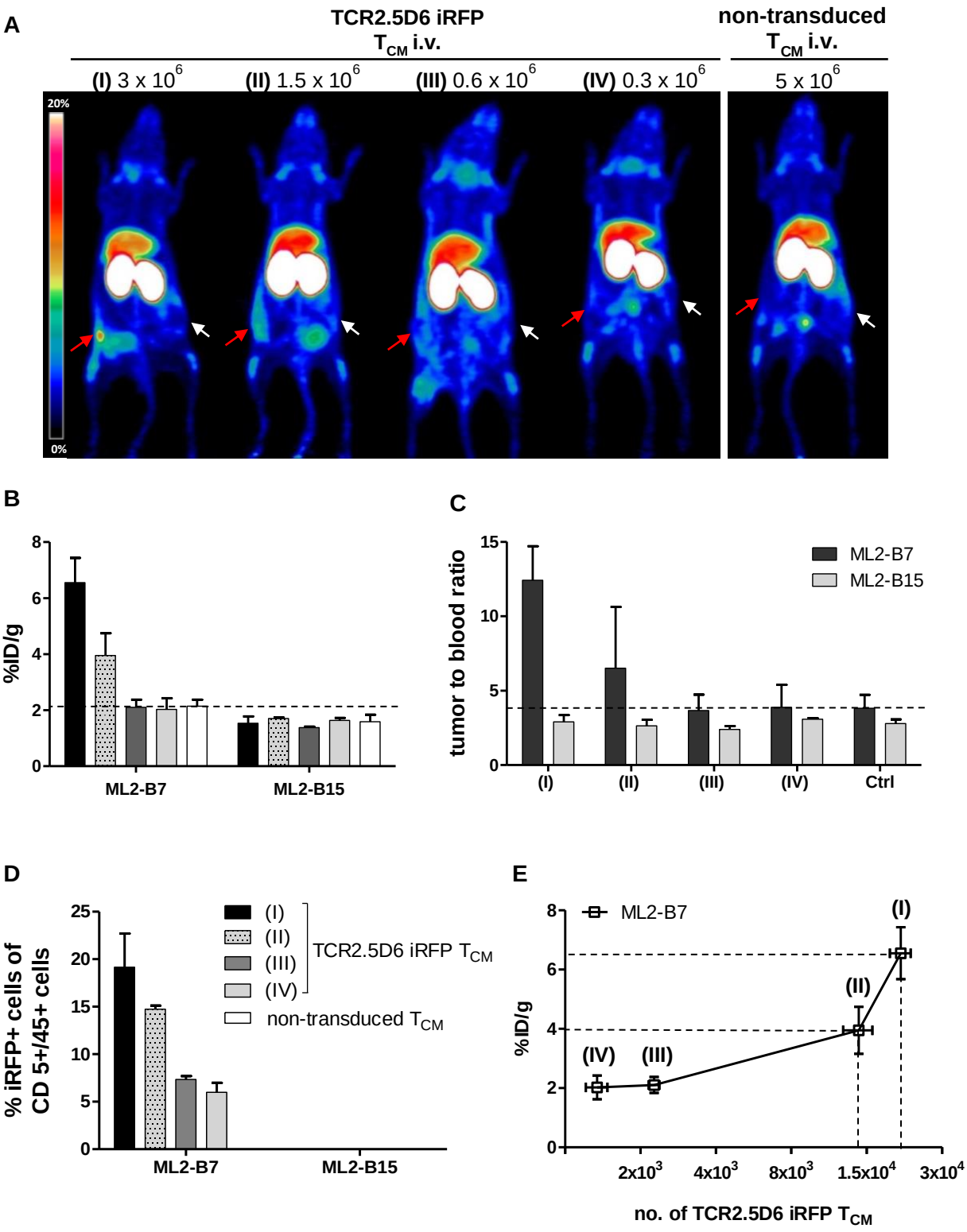

Figure 16. *In vivo* and *ex vivo* evaluation of the detection limit of intravenously transferred TCR2.5D6 iRFP T_{CM}.

(A) Representative 3D-PET (MIP) images of animal groups (I) to (IV) (n=2 for group I and IV, n=3 for group II and III) injected with different TCR2.5D6 iRFP T_{CM} concentrations (3×10^6 to 0.3×10^6) or non-transduced T_{CM} (5×10^6) (n=2). Red arrows indicate the signal at the ML2-B7 tumor and white

arrows point to the control tumor ML2-B15. Scale bar 0–20 %ID/g. (B) Activity accumulation in ML2-B7 and ML2-B15 tumors 48 h after injection of ^{89}Zr-Df-aTCRmu-F(ab')$_2$ after is shown. Mean ± SD of %ID/g are depicted for the animal groups (n=2 for group I and IV, n=3 for group II and III). The dashed line indicates background level of activity accumulation. (C) Quantitative evaluation of tumors-to-blood ratios 48 h post ^{89}Zr-Df-aTCRmu-F(ab')$_2$ injection. Mean ± SD of the ratios are depicted for the animal groups (n=2 for group I and IV, n=3 for group II and III) and n=2 treated with non-transduced T_{CM}. Dashed line indicates maximum background ratio in the groups. (D) *Ex vivo* flow cytometry analysis of engrafted TCR2.5D6 iRFP T_{CM} at ML2-B7 and ML2-B15 tumors expressed as percentage (%) of iRFP+ cells out of hCD5+hCD45+ cells is shown. Mean ± SD % of iRFP positive cells are shown for the described animal groups (n=2 for group I and IV, n=3 for group II and III). (E) Relation of detected total numbers of TCR2.5D6 iRFP T_{CM} within ML2-B7 tumors and the %ID/g in the animal groups (I) to (IV). Ranges between dashed lines indicate the detection limit of TCR2.5D6 iRFP T_{CM} and related activity uptake, where mean ± SD of %ID/g and mean ± SD of total TCR2.5D6 iRFP T_{CM} numbers detected by flow cytometry analysis are shown.

5.8.3 Quantification after different T-cell engraftments

To strengthen the findings of the study described in section 5.8.2, the experiments were repeated further three times. In all studies, similar detection limits were observed, even though T-cell engraftment rates differed in the individual experiments. Notably, in the indicated T-cell concentration groups, different total numbers of TCR2.5D6 iRFP T_{CM} were determined within the ML2-B7 tumors *ex vivo*, however they corresponded well to signal intensities of the PET-images (Figure 17 A-B). In T-cell concentration group (I) the PET signals at ML2-B7 in the individual experiments were distinctive, but of different intensities, dependent from the *ex vivo* quantified number of TCR2.5D6 iRFP T_{CM} ranging from 2.2×10^4 to 6.2×10^4 cells. In T-cell concentration group (II) less T cells were counted at the target tumor site ($< 1.9 \times 10^4$) being not related to a specific PET signal as shown in the top and middle panel, but a marginal signal at a quantified cell number of 1.9×10^4 (lower panel). As anticipated, in group (III) low detected T-cell numbers ($<6.0 \times 10^3$) didn't reveal any related specific signal, comparable to T-cell numbers and PET-signals at ML2-B15. The image-based PET-signal evaluation of ML2-B7 and ML2-B15 provided mean activity values (mean Bq/ml), which were in accordance to T-cell number and PET signal levels, as activities were

over background values (Ctrl) in group I, decreasing with poorer T-cell engraftment (Figure 17C). Setting the *ex vivo* quantified numbers of TCR2.5D6 iRFP T_{CM} cells in relation to the mean activity values in the ML2-B7 tumors, a coherence of T-cell number and signal is indicated (Figure 18A-C).

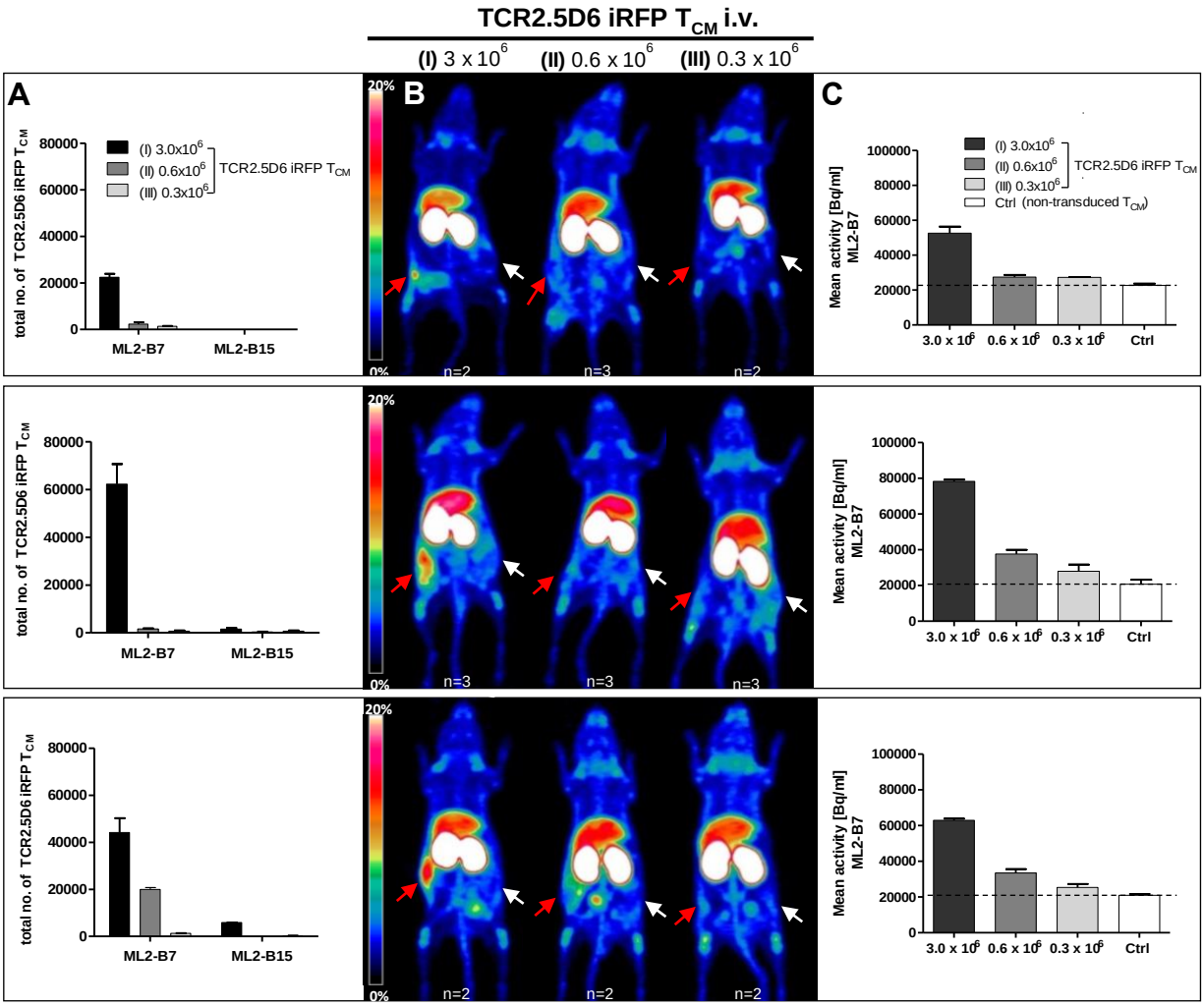

Figure 17. Relation of *ex vivo* quantified TCR2.5D6 iRFP T_{CM} numbers and PET signal *in vivo* in experiments with individual engraftment rates.

(A) Total numbers of TCR2.5D6 iRFP T_{CM} *ex vivo* quantified by flow cytometry in ML2-B7 and ML2-B15 tumors in three from four individual experiments, where groups of NSG mice were injected with (I) 3.0 x 10^6, (II) 0.6 x 10^6 and (III) 0.3 x 10^6 TCR2.5D6 iRFP T_{CM}. (B) Representative 3D-PET (MIP) images in respective three individual experiments injected with 3.0 x 10^6, 0.6 x 10^6 and 0.3 x 10^6 TCR2.5D6 iRFP T_{CM}. Red arrows indicate the PET signal at the ML2-B7 tumors and white arrows point to the control tumor ML2-B15. Scale bars 0–20 %ID/g. (C) Image-based activity evaluation of ML2-B7 tumors of the three individual experiments with the animal groups injected with (I) 3.0 x 10^6, (II) 0.6 x 10^6 and (III) 0.3 x 10^6 TCR2.5D6 iRFP T_{CM}. Mean activity [Bq/ml] of ROI analysis is shown as

mean ± SD. Dotted lines indicate the level of background activities based on the control groups (n=2) in the three experiments injected with 5.0 x 10^6 non-transduced T_{CM} (Ctrl). (A-C) The top, middle and lower panels represent one of the three individual experiments.

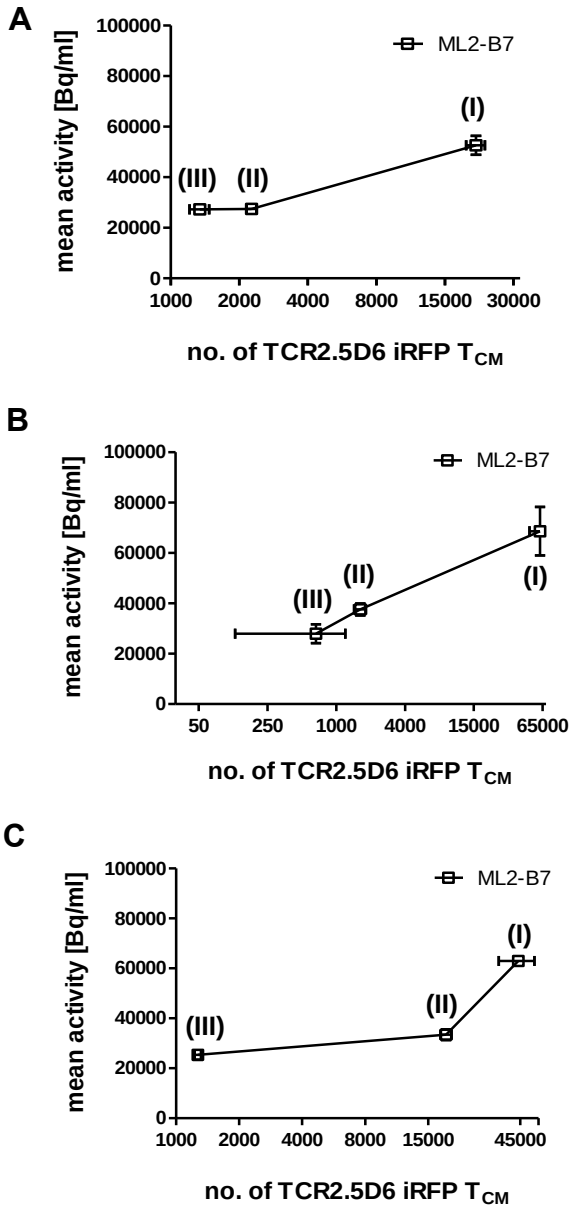

Figure 18. Relation of absolute numbers of *ex vivo* quantified TCR2.5D6 iRFP T_{CM} after adoptive T-cell transfer *in vivo* and PET-image derived activity accumulation.
(A-C) Relation of absolute numbers of TCR2.5D6 iRFP T_{CM} to mean activity at ML2-B7 tumors in animal groups injected with 3.0x10^6 (I), 0.6x10^6 (II) and 0.3x10^6 (III) TCR2.5D6 iRFP T_{CM} is shown. Total number of TCR2.5D6 iRFP T_{CM} and image-derived mean activity [Bq/ml] are shown as mean ± SD. (A-C) The top, middle and lower graph represent one of the three individual experiments.

5.8.4 Correlation of ex vivo and in vivo acquired data

In the previously described experimental setting to estimate the detection limit, it has been observed, that transgenic T cells engraft and expand differently due to variations in animal sets and T_{CM} origin. Therefore, repeating this study in order to obtain reproducible rates

remains for given reason challenging, however the connection of TCR2.5D6 iRFP T_{CM} and PET-signal described in section 5.8.4 allows to perform classifications based on strength of T-cell infiltration and corresponding tracer accumulation in the ML2-B7 tumor tissue (Figure 19A). Classified group 1 (n=9) comprising > 20.000 *ex vivo* quantified T cells corresponds to 6.18 ± 1.7 %ID/g and 60066 ± 11616 Bq/ml tracer accumulation, which is significantly higher than activities in classified group 4 (control group, non-transduced T_{CM}) with 2.09 ± 0.2 %ID/g and 20254 ± 4290 Bq/ml (Figure 19B-C). To this group strong PET signals were associated as shown in Figure 17B (group I). Classified group 2 (n=5) involved tumors infiltrated with transgenic T cells quantified in the middle range with 10.000 – 20.000 cells, where the detection limit was set. The associated tracer uptake in this group still differed significantly from the uptake in control tumors (3.52 ± 1.41 %ID/g and 34942 ± 5284 Bq/ml). Tumors revealing *ex vivo* < 10.000 infiltrated T cells were classified as group 3 (n=29) and didn't show any significant difference in activity uptake compared to the control group. Considering in this clinical relevant experimental setting the statistical evaluation of different T-cell infiltration rates versus corresponding PET images, the detection limit can be set at 10.000 - 20.000 *ex vivo* quantified T cells, being in a comparable range to the limit of visualized *in vitro* labeled cells (section 5.7).

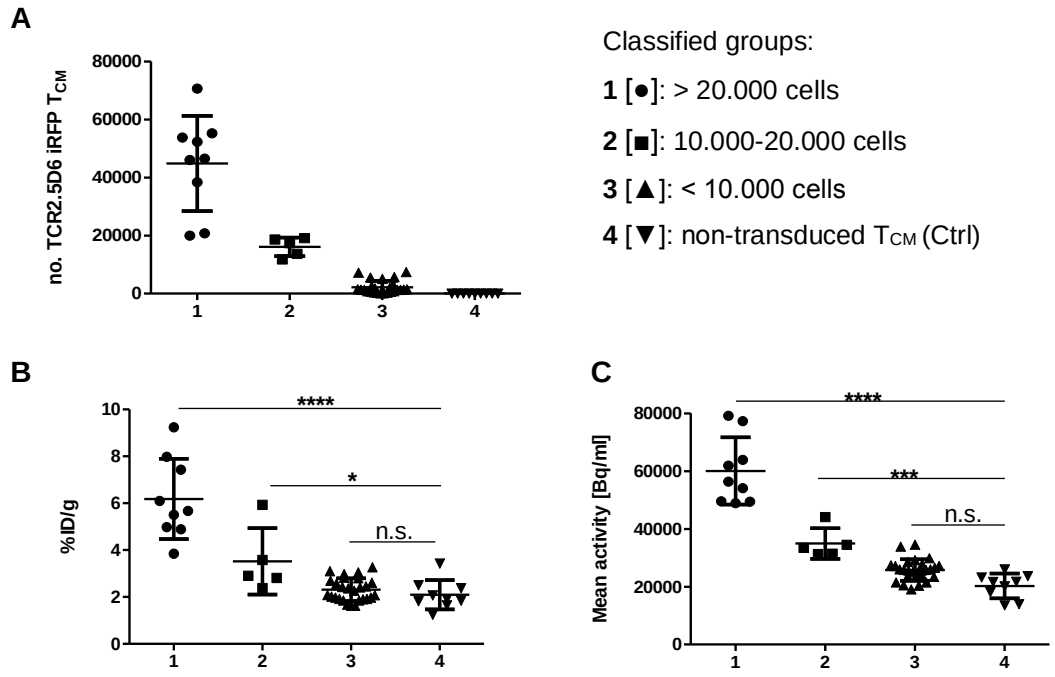

Figure 19. Correlation of TCR2.5D6 iRFP T_{CM} numbers and PET signal *in vivo* in experiments with different engraftment rates

(A) Total numbers of TCR2.5D6 iRFP T_{CM} quantified *ex vivo* by flow cytometry in ML2-B7 tumors deriving from four experiments, where 3.0 x 10^6 (I), 0.6 x 10^6 (II) and 0.3 x 10^6 (III) TCR2.5D6 iRFP T_{CM} were transferred i.v. Classified groups of total numbers of TCR2.5D6 iRFP T_{CM}: group 1 (n=9): >20.000 cells [●]; group 2 (n=5): 10.000 - 20.000 cells [■]; group 3 (n=29): <10.000 [▲] and group 4 (n=9): non-transduced T_{CM} (Control group) [▼] (B) Corresponding %ID/g to every tumor in indicated classified groups compared to the values in control group 4. (C) Corresponding image-derived activity (Bq/ml) to every tumor in indicated classified groups compared to the control group 4. Mann–Whitney test; ****, P < 0.0001; ***, P < 0.01; *, P < 0.05; n.s, non-significant.

In view of the shown relation between T-cell number, activity uptake and signal intensity in the PET images, all quantified T cells and corresponding activities (n=43) were summarized in a scatter plot and revealed after linear regresion analysis a high correlation of these parameters in the presented experimental model, as predicitive fit of the two parameters were 64 % (%ID/g) and 77 % (Bq/ml), respectively (Figure 20A-B).

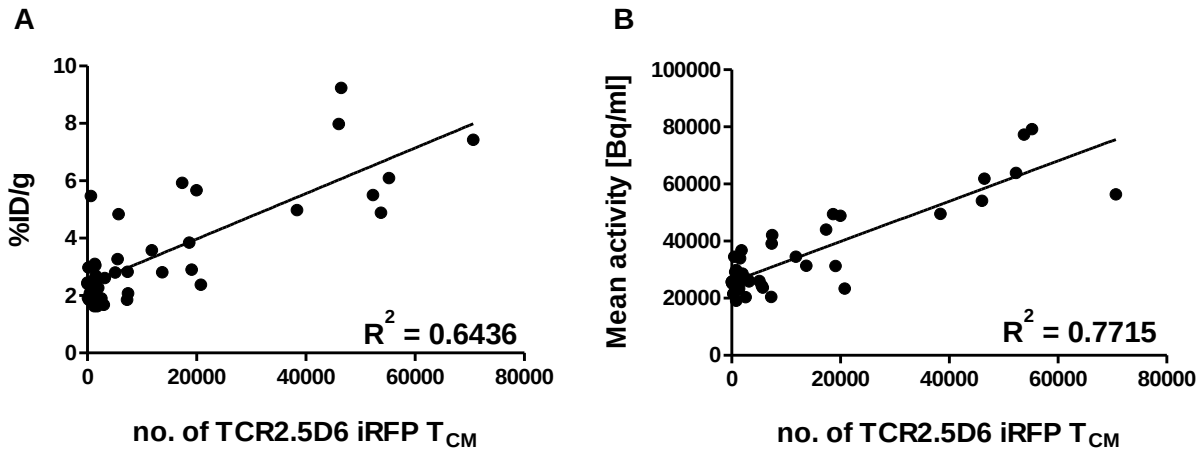

Figure 20. Correlation of number of tumor infiltrated TCR2.5D6 iRFP T_{CM} and probe accumulation.

Linear regression analysis in scatter plots showing the number of *ex vivo* detected TCR2.5D6 iRFP T_{CM} in ML2-B7 tumors and corresponding %ID/g from biodistribution (A) or image-based activity (Bq/ml) (B) deriving from four different experiments (n=43). The goodness of fir is expressed as R^2 calculated from the regression analysis.

5.8.5 Tissue based ex vivo quantification of TCR2.5D6 iRFP T_{CM}

In addition to the *ex vivo* quantification of T cells by flow cytometry, tissue analysis by IHC has been performed of T-cell infiltrated ML2-B7 tumors. This study has been performed in NSG animals bearing on both flanks the target tumor ML2-B7. The T-cell transfer and tracer injection was performed according to the experimental scheme described in Figure 15A. After PET imaging, in every animal one tumor was used for flow cytometric T-cell quantification and the other for IHC analysis. Based on the *ex vivo* determined number of TCR2.5D6 iRFP T_{CM} by flow cytometry, the animals were classified to groups according to the classification in Figure 19, where classified group 1 (n=3) included > 20.000 TCR2.5D6 iRFP T_{CM}, classified group 2 (n=3) 10.000 - 20.000 cells, classified group 3 (n=4) <10.000 cells and group 4 (n=3) non-transduced T_{CM} representing the control group. The second ML2-B7 tumor in animals of the respective groups was stained in the IHC analysis for CD3. On tissue level, the prominent PET signals of classified group 1 (Figure 21A, left panel) were associated to a high rate of CD3 positive signals (Figure 21B). The faint signals in group 2

(middle) still corresponded to CD3 positive cells in the tissue being less than in group 1 though. Non-specific PET-signals of group 3 revealed in the tissues a very low occurrence rates of T cells (right)

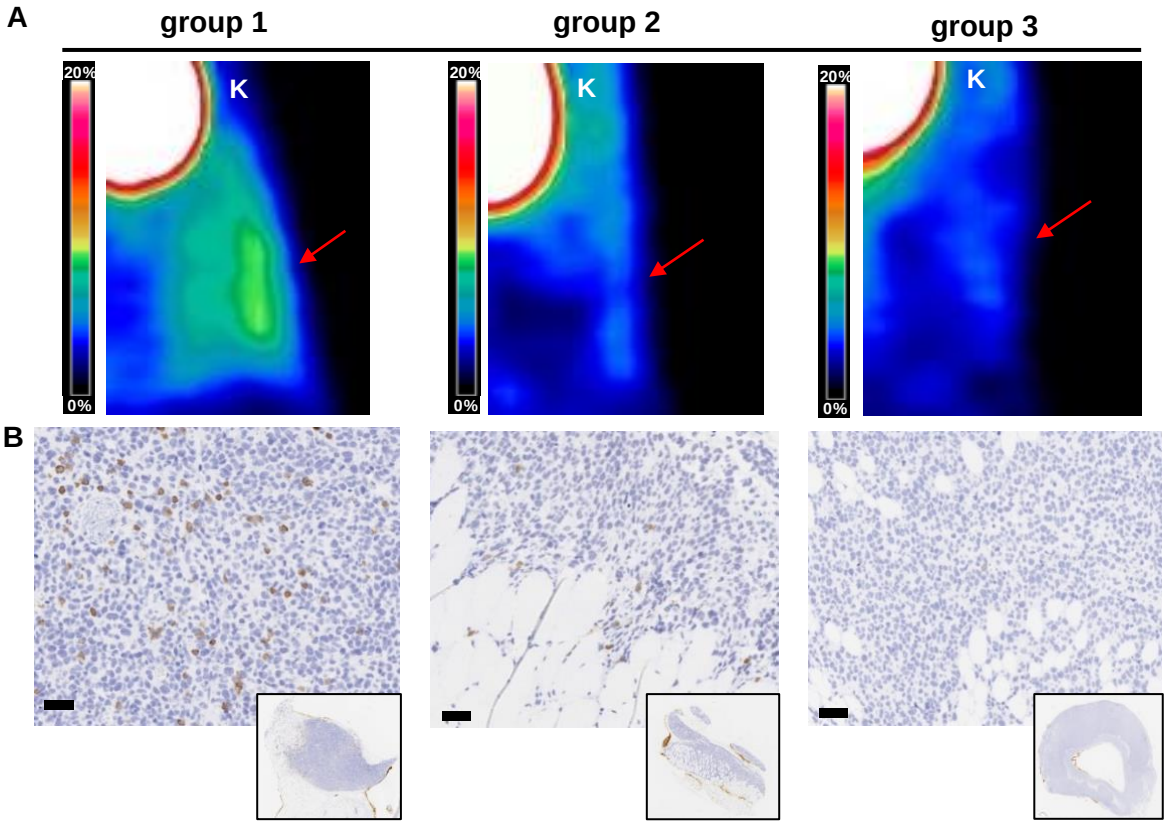

Figure 21. Immunohistochemical analysis of TCR2.5D6 iRFP T_{CM} infiltrated ML2-B7 tumors
(A) Representative 3D-PET (MIP) images of ML2-B7 tumors classified based on the strength of TCR2.5D6 iRFP T_{CM} infiltration (group 1 (n=3) >20.000 cells; group 2 (n=3): 10.000-20.000 cells; group 3 (n=4): <10.000) and (B) corresponding IHC stainings for CD3. PET scale bar 0–20 %ID/g. K=kidney. Red arrows indicate the ML2-B7 tumors. Magnification 20X, scale bar equals to 50 µm. IHC analyses were performed by Dr. Katja Steiger, Institute of pathology, Klinikum rechts der Isar.

For the quantitative evaluation of the anti-CD3 stainings of the ML2-B7 tissues, the number of positive CD3 pixels were analyzed and counted with the help of a computer-based program, which detected specific positive spots in the defined area of the respective sections (Figure 22A). The high counts of positive pixel per mm^2 in group 1 (> 100.000 pixel/mm^2) were significantly higher than counts detected in the control group 4. The pixel numbers of

group 2 and 3 didn't differ from the control group. These findings affirm the results presented in section 5.8, were quantified T-cell numbers around 20.000 were correlated to a specific PET signal and were presented as detection limit. In this study the group 2, comprising numbers between 10.000 - 20.000 cells, wasn't different than the control group despite the marginal signals in PET/CT. This might be related to the different sensitivities of the selected methods to detect T cells, however the quantitative range remains similar and the correspondence between the findings is indicated.

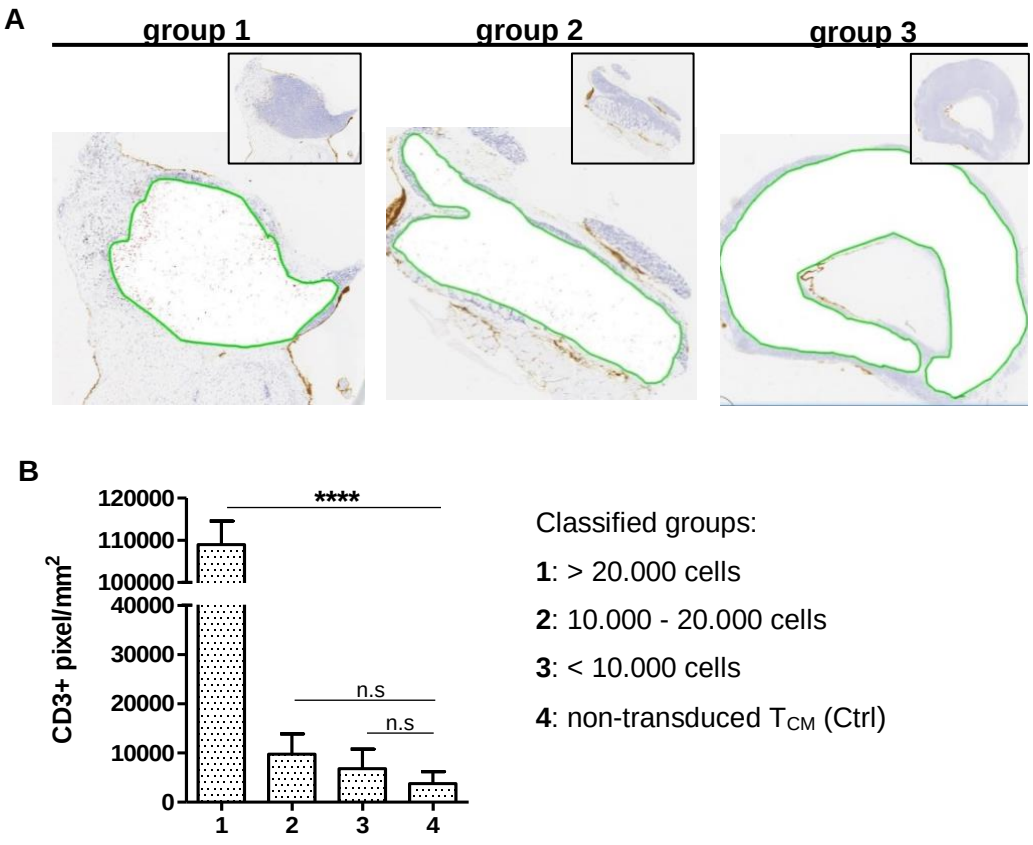

Figure 22. Quantitative analysis of CD3 positive cells in ML2-B7 tumor sections.
(A) CD3 positive pixel in ML2-B7 tumor sections deriving from classified animal groups (group 1 (n=3) >20.000 cells; group 2 (n=3): 10.000 - 20.000 cells; group 3 (n=4): <10.000). Quantitative computer-based analysis of CD3 positive pixel within green outlined tissue areas revealed (B) CD3+ pixel/mm^2 in tissues of the indicated groups (group 4 (n=3): non-transduced T_{CM}= control group). Unpaired t-test; ****, P < 0.0001; n.s, non-significant.

6 DISCUSSION

6.1 IMMUNO-PET OF TRANSGENIC T CELLS WITH ^{89}ZR-DF-ATCRMU-F(AB')$_2$

Since T-cell based immunotherapy showed in first trials clinical efficacy (Morgan et al. 2006; Johnson et al. 2009; Rapoport et al. 2015; Robbins et al. 2015), the necessity of non-invasive imaging technologies as clinical surveillance tool for the transferred T cells played in the last years a crucial role in research. Therefore, immuno-PET is supposed to represent the most appropriate method to encounter the challenging task to track trafficking T cells *in vivo*. To date, most PET imaging approaches were conducted by direct labeling of lymphocytes with radioactive labeling agents, such as ^{18}F-FDG, ^{64}Cu-PTSM or different ^{89}Zr-coupled agents (table 2). These methods have in common, that the cells are directly labelled *ex vivo* and were transferred in the preclinical model for imaging. Particularly poor labeling yields and high efflux rates of the radioactive tag, for instance as reported for the labeling with ^{18}F-FDG of leukocytes (Botti et al. 1997; Forstrom et al. 2000; Bhargava et al. 2009) contribute to low accuracy of this imaging technique. Furthermore, direct labeling with ^{18}F, ^{64}Cu and ^{89}Zr was described in the studies to reduce viability and functionality of the labeled cell type, which may be caused by either the labeling agent or the radioactivity of respective radionuclide (Botti et al. 1997; Griessinger et al. 2014; Fairclough et al. 2016). Nevertheless, the major disadvantage of direct tagging of immune cells remains the missing ability to track proliferating cells, resulting in dilution of the associated PET signal within a short time, which hampers longitudinal monitoring and quantitative evaluation of the effector cells. Likewise, the use of radioactive metabolite probes bears technical disadvantages, since signals deriving from the immune cells are difficult to distinguish to background signals from the environment, particularly from a highly metabolic active tumor environment (Gambhir 2002). Reporter genes overcome the question of monitoring dividing T cells over longer periods and recent studies using reporters based on the human derived gene deoxycytidine kinase

(hdCK) could follow CAR and TCR transgenic T cells *in vivo* (Likar et al. 2010; McCracken et al. 2015). Although reporter gene systems may provide suitable imaging data in preclinical studies, the clinical translation may be hampered by the risk of insertional oncogenesis or vector splicing due to the foreign gene loading additional to the tumor-specific TCR (Blumenthal et al. 2007).

The fact that therapeutic antibodies are currently widely used in the clinic for a variety of diseases and even more are entering in the future the clinic after approval (Ecker, Jones, and Levine 2015; Reichert 2016), demonstrate their experienced and efficacious application, which can be further exploited for diagnostic purposes in the field of non-invasive imaging. Intact antibodies and antibody based scaffolds combined with a radionuclide constitute specific tracers for antigens and epitopes, which can be targeted *in vivo* and imaged by SPECT or PET. As PET provides in the clinic better sensitivity as well as spatial resolution and wide availability of both short-lived and long-lived PET-radionuclides, the potential of immuno-PET for T-cell imaging prevails over the SPECT modality (van Dongen and Vosjan 2010).

So far, few studies were conducted to follow T cells *in vivo* via immuno-PET using intact antibodies and antibody deriving scaffolds (table 5). In the present work, we used a hamster antibody derived anti-murine TCRβ-F(ab')$_2$ fragment coupled to the PET-radionuclide ^{89}Zr, which has been applied i.v. after adoptive transfer of TCR transgenic T cells (Mall et al. 2016). We could specifically detect the human transgenic T cells *in vivo* after 48 h of tracer administration at the targeted tumor site without any non-specific accumulation of the tracer in other tissues, particularly not at the control tumor site. Furthermore, the radiotracer allowed to specifically distinguish between transgenic T cells and native non-transduced T cells, which were transferred in respective control groups.

For a clinical translation, the tested radiotracer should fulfill crucial safety criteria for clinical use, which are unchanged pharmacokinetics compared to the native scaffold, unimpaired affinity to its target and no release of ^{89}Zr (Heskamp et al. 2017). To evaluate these criteria,

in this work initially ^{89}Zr-Df-aTCRmu-F(ab')$_2$ was assessed for binding affinity to the targeted TCR, immunoreactivity, stability *in vitro* and *in vivo* after chelator conjugation and chelation with ^{89}Zr. In the quality evaluation studies ^{89}Zr-Df-aTCRmu-F(ab')$_2$ showed compared to native aTCRmu-F(ab')$_2$ and its intact antibody retained affinity and reactivity. Furthermore, the radiotracer provided solid stability *in vitro* in human serum and the storage medium over several days being consistent to stability data provided by Perk et al. (Perk et al. 2010). For the application *in vivo*, the stability of the tracer was further tested *in vivo*, showing intact tracer within the course of a day in the blood pool until specific uptake and imaging.

A characteristic of ^{89}Zr is the accumulation in the bone, when released from the radio-immunocomplex (Abou, Ku, and Smith-Jones 2011) and needs to be taken into account, when applied in the scope of bone metastases. However, the PET data imply, that ^{89}Zr-Df-aTCRmu-F(ab')$_2$ didn't release the radionuclide, since accumulation in bone and joints are not detected. In internalization studies, it has been shown, that ^{89}Zr-Df-aTCRmu-F(ab')$_2$ is increasingly taken up into the cells within the first hours after binding. This ensures additionally accuracy of image acquisition of T cells, since ^{89}Zr accumulates and residualizes in target cells after internalization allowing long-term tracking (Vugts and van Dongen 2011; Deri et al. 2013). Notably, ^{89}Zr-Df-aTCRmu-IgG showed in the comparing internalization studies higher incorporation rates than its fragment, indicating the uptake is also mediated via Fc portion binding. The use of ^{89}Zr-Df-aTCRmu-IgG might have advantages regarding ^{89}Zr accumulation into the cells, however initial *in vivo* studies in ML2-WT and ML2-B7 bearing NSG mice have shown high background signals in diverse tissues and non-specific binding to the control tumor ML2-WT (data not shown). A closer look on the surface expression of the tumor cells revealed FcR-expression, which is problematic for reliable and accurate image acquisition (performed by Sabine Mall, data not shown). The use of the F(ab')$_2$ fragment not only abolished enhanced non-specific background signaling, but also showed earlier optimal tumor-to-background ratios (48 h) in comparison to the intact antibody (>72 h). For instance, high background signal issues are apparent in the latest study from

England et al., where ^{89}Zr-labeled full antibody Nivolumab is used for immuno-PET of PD-1 expressing T cells in humanized tumor mice. Here, over the course of time strong background and very late optimal tumor-to background ratios are achieved (168 h) (England et al. 2017). Griessinger et al. used a ^{64}Cu labeled antibody to target homing of cOVA-TCRtg-Th1 cells *in vivo*, showing initially at least internalization and retained residualization of the complexed radionuclide (Griessinger et al. 2015). Background uptake from the radiotracer is not described, as the cells were directly labeled prior intraperitoneal injection, therefore this study doesn't allow quantitative evaluation of T-cell distribution over longer periods of time.

6.2 T-CELL FUNCTIONALITY AFTER RADIOTRACER BINDING

An important feature of the applied radiotracer in immuno-PET for tracking therapeutically active cells is the role as a surrogate marker, which is not altering T-cell mechanisms and functionality *in vivo*. We tested our imaging approach *in vitro* and *in vivo* with focus on IFN-γ release of the T cells and radiation induced DNA damage after binding of ^{89}Zr-Df-aTCRmu-F(ab')$_2$. Like previously reported (Kubo et al. 1989; Drobyski and Majewski 1996; Nishimura et al. 1994; Kummer et al. 2001), we showed that aTCRmu-IgG binding at higher concentrations (> 5 nmol/L) caused T-cell activation and increased apoptosis compared to aTCRmu-F(ab')$_2$ (Mall et al. 2016). Since the T-cell activation should be preserved and get triggered only by antigen binding, the structurally modified ^{89}Zr-Df-aTCRmu-F(ab')$_2$ was tested for its impact on activation capability shortly and long-termed after binding. The TCR transgenic T cells maintained their functionality after ML2-B7 stimulation by IFN-γ release directly as well as 48 h hours after radiotracer binding at concentrations up to 100 nM. This supports the use of the immuno-PET technique for T-cell imaging, as direct labeling methods with PET-tracer were reported to impair functionality or to be cytotoxic (Bhargava et al. 2009;

Botti et al. 1997; Charoenphun et al. 2015), being likely related to either the used labeling agent or the associated radionuclide.

Therefore, we aimed to assess additionally to the IFN-γ release of the T cells, the potential risk of impairment by radiation. For that γH2AX expression as DSB marker was investigated *in vitro* and *in vivo* shortly as well as 48 h after ^{89}Zr-Df-aTCRmu-F(ab')$_2$ binding. *In vitro* T cells can tolerate ^{89}Zr derived radiation up to 18.5 MBq (500 µCi) without inducing DSB or related cell death shortly after exposure or after 48 h. *In vivo* the dose of 2.2 MBq (corresponding to 15-20 µg protein), which has been applied in all imaging studies for the NSG mice, induced no yH2AX expression or apoptosis. To extrapolate these findings to the implementation in humans, allometric scaling should be consulted, where theoretically at least 7-fold of the applied activity in mice is used as human equivalent dose (HED) (USFDA 2005; Nair and Jacob 2016). For imaging, this would be approximately 15.5 MBq (420 µCi), which is within the safe activity range measured *in vitro* after ^{89}Zr-Df-aTCRmu-F(ab')$_2$ exposure. In clinical trials using ^{89}Zr labeled antibodies, such as ^{89}Zr-pertuzumab (anti-HER2) or ^{89}Zr-panitumumab (anti-EGFR), has shown that an applied dose of 74 MBq resulted in mean effective doses of 0.53-0.66 mSv/MBq (Ulaner et al. 2017; Lindenberg et al. 2017), being adequate for imaging. However this range of effective dose is still described as relatively high radiation burden, when compared to doses of ^{111}In or ^{99m}Tc based tracer used in the clinic (van de Watering et al. 2014). Still these dosimetric values are deriving from ^{89}Zr coupled intact antibodies, which have longer half-lives as their fragments, thus resulting in increased radiation burden over time. On one hand F(ab')$_2$ has shown earlier optimal signal to background ratios and faster clearance and on the other hand ^{89}Zr-Df-aTCRmu-F(ab')$_2$ is supposed to serve merely as diagnostic marker, meaning that lower activities might be sufficient for qualitative imaging. The scaled dose of around 15.5 MBq could serve as starting value for imaging and dosimetric studies, which needs to be addressed carefully for translational purposes. For immuno-PET ^{18}F and ^{64}Cu were shown after lymphocyte labeling to reduce significantly the cell viability and to decrease functionality of the cells with related

DSB in case of ^{64}Cu already with lower activities (0.7 MBq) within 48 h (Botti et al. 1997; Bhargava et al. 2009; Griessinger et al. 2015; Griessinger et al. 2014). We showed in our study, that T cells tolerate ^{89}Zr derived radiation up to 18.5 MBq up to 48 h *in vitro* and didn't show impairment of IFN-γ secretion over this period after binding of high concentrations of the radiotracer (up to 100 nM). *In vivo* the animal dose of 2.2 MBq didn't harm infiltrating T cells on DNA-level, nevertheless studies with increased doses in the range of HED need to be further investigated. All in all, ^{89}Zr provides as radionuclide and in combination with our developed targeting molecule suitable properties in view of safety for T-cell tracking *in vivo*.

6.3 RADIOTRACER DESIGN FOR T-CELL IMAGING – TRANSLATIONAL ASPECTS

For the clinical implementation of an imaging strategy a variety of factors need to be excluded to ensure the safe use, such as immunogenicity and radiation burden of the used radiotracer. The murinized constant domain of the introduced TCR in our study may constitute such a risk factor in human use. It has been reported, that a murine TCR induced antibody development against its variable domains, however this response wasn't influencing the overall clinical outcome (Davis et al. 2010). Therefore, a reduction of the murinized sequence is desirable to reduce the risk immunogenic recognition. This may be feasible according to a study, where replacing only nine amino-acids in human TCR with the murine equivalent still resulted in conserved expression of the introduced TCR and preferential pairing (Sommermeyer and Uckert 2010). It should be considered, that the epitope is included in the condensed sequence, so that the epitope needs to be identified before minimization. In combination to a minimal murinized sequence in the constant region a humanization of the antibody/F(ab')$_2$ would be advantageous for reduction of immunogenicity (Ahmadzadeh et al. 2014).

Optimal tumor-background ratios for imaging was achieved in case of ^{89}Zr-Df-aTCRmu-F(ab')$_2$ after only 48 h, being characteristic for intact antibodies and F(ab')$_2$ fragments. The long circulation half-lives from days to weeks require accordingly long-living PET-radionuclides, such as ^{124}I, ^{64}Cu or ^{89}Zr (Boswell and Brechbiel 2007). Since residualization of the radionuclide improves accuracy and supports long-term tracking, the choice is made rather in favor of radiometals, than of radiohalogens. As described in section 6.2 radiation burden deriving from the radiotracer plays an important role for safety and applicability as diagnostic marker. As shown for ^{64}Cu (Bhargava et al. 2009; Griessinger et al. 2014; Griessinger et al. 2015), toxicity and impairment of functionality of the therapeutic T cells hampers its potential for clinical use. ^{89}Zr is used so far in the clinic with suitable characteristics for diagnostic imaging, however it shows in combination with long-circulating targeting molecules relatively high effective doses (van de Watering et al. 2014). A shortened circulation time of the targeting molecules is beside for the reduced radiation burden also desirable for an undelayed handling in the clinical routine, when it comes to application and PET imaging. For preclinical T-cell imaging first approaches for this issue were undertaken by the use of minimalist biomolecules, such as minibodies or diabodies with circulation times of only 5 - 6 h (Holliger and Hudson 2005) (section 1.4.4). Studies using ^{89}Zr labeled diabodies for CD4 and CD8 imaging showed already 4 h post tracer injection specific signals of targeted immune cells (Tavare et al. 2015; Tavare et al. 2016). However optimal target-to-background ratios were still acquired 22 h later and observed aggregation of the diabodies needs to be prevented for a clinical application. F(ab')$_2$ fragments and molecules with sizes over the renal filtration cutoff of ~60 kDa are cleared through either the kidneys or liver, while scaffolds with smaller sizes, such as scFv (~25 kDa), nanobodies (~12.5 kDa) or affibodies (~6 kDa) pass predominantly the renal pathway. The use of small-sized fragments resulting in early optimal target-to-background ratios compared to intact antibodies or its derived fragments allows performing potential same-day imaging with the help of short-lived emitters, such as ^{68}Ga, ^{18}F or ^{61}Cu. The rapid procedure between application and imaging and the

related reduced ration burden make minimalist scaffolds particularly interesting for clinical translation. However, detriments in reduced target uptake of the small sized radiotracer due to their monovalent binding properties need to be considered (Holliger and Hudson 2005). It's proposed to further explore intermediate sized multivalent molecules, such as diabodies, however reduced uptake is so far described for tumor imaging and needs to be further investigated for diagnostic T-cell imaging.

Further pharmacokinetic influencing factors need to be considered for a suitable probe after choosing the appropriate protein and radionuclide based on half-life and emission data. These are the conjugation strategy of the biomolecule by the chosen chelator and the purification procedure of the final probe (McCracken et al. 2016). In our study, we conjugated the aTCRmu-F(ab')$_2$ fragment with the widely used DFO chelator according to the established protocol of Perk et al. (Perk et al. 2010). Although PET images didn't show in our studies significant accumulation of ^{89}Zr in the bone or joints, there are various reports about increased bone uptake *in vivo* of released ^{89}Zr reaching values >10 %ID/g, when ^{89}Zr-DFO-complexes were used, which may hamper a potential clinical use (Perk et al. 2005; Dijkers et al. 2009; Heskamp et al. 2010). Recently, several novel and promising alternatives to regular DFO were proposed for complexation of ^{89}Zr, as for instance DFO-Sq, DFO* or HOPO, which are showing superior stability *in vitro* and *in vivo* as well as reduced bone and liver uptake (Heskamp et al. 2017; Deri et al. 2015; Vugts et al. 2017). For an EGFR-targeting ^{89}Zr-labeled affibody, a recent study showed that fusarinine C (FSC) represents a suitable alternative for DFO, when radiolabeled at elevated temperatures resulting in considerably improved complex stability and tumor-to-organ ratios (Summer et al. 2017). Nevertheless, radiolabeling at high temperatures remains reserved for heat insensitive biomolecules and may not be advisable for intact antibodies or its fragments.

The conjugation of the bifunctional chelators is most often conducted via isothiocyanates, as performed in our study, or *N*-hydroxysuccinimide esters, binding to nucleophilic ε-amino groups of exposed lysine residues of the biomolecule. This site non-specific conjugation

approach may potentially interfere with the binding capability, when crucial lysine residues at antigen binding sites are involved. Particularly, smaller sized scaffolds are reduced in numbers of non-critical exposed lysine residues, resulting in inconsistent batches of conjugated biomolecules with different pharmacokinetics. This becomes unfavorable, when small biomolecules are intended for labeling with short-lived emitters and fast kinetics are required. Therefore, site-specific conjugation techniques become highly relevant for generation of consistent and reliable batches. For instance, latest approaches to solve this issue include introduction of engineered cysteine residues or chips for site specific click-chemistry reactions, leading to efficiently conjugated and homogenous complexes (Zeng et al. 2013; Whittenberg et al. 2017).

Taken together, the choice of protein scaffold, radionuclide and conjugation strategy with a suitable chelator need to be further explored, as there is still room for improvement of pharmacokinetics and quality of the radiotracer within the scope of T-cell imaging *in vivo*.

6.4 SENSITIVITY OF THE TRACKING TECHNIQUE IN SMALL ANIMAL PET

In this study, we aimed also to evaluate the sensitivity and accuracy of the tracking method by comparing *ex vivo* gained data, such as number of quantified T cells and tracer accumulation, to the related PET signals. We obtained in the initial study with *in vitro* tracer labeled T cells (section 5.7) a detection limit in the range of 2×10^4 TCR transgenic T cells in the used small animal PET scanner (Inveon). Subsequent *in vivo* studies in the clinical relevant tumor model (section 5.8), where T cells were adoptively transferred and the radiotracer was injected i.v., revealed detection limits in the similar range. Interestingly, this observation was independent from the engraftment behavior of the transferred T cells, being highly relevant for the accuracy of this method and reflecting the clinical situation, when different patients receive a certain dose of transgenic T cells. Classifying in different rates of tumor infiltration, the quantified T-cell numbers correlated in this study with activity

accumulation and related PET signal intensities, with significant differences in T-cell numbers and activity between specific and background signals.

When compared to detection thresholds of other imaging modalities on single cell level, BLI still represents the most sensitive modality, as shown by Mezzanotte et al., where still 5 x 10^3 s.c. implanted pTurboLuc expressing HEK-293 cells are shown to be detectable (Mezzanotte et al. 2014). However, BLI imaging remains reserved for preclinical models and is not suitable and for T-cell imaging in human whole body scans due to its low tissue penetration. As indicated in table 1, MRI provides exceptional spatial resolution, but is also characterized by its low sensitivity. Nevertheless, Kircher et al. showed to our findings comparable detection limit of 3 x 10^4 in 50µl volumes *in vitro*, when CD8+ T cells were labeled with CLIO-HD (Kircher et al. 2003). Sensitive visualization of T cells may be feasible by MRI, although its sensitivity is relatively low to PET. However, imaging techniques are so far limited to direct labeling of the therapeutic cells and only to imaging after s.c. implantation and not during *in vivo* trafficking and proliferation

To date, the described studies using radiolabeled protein scaffolds for *in vivo* T-cell PET imaging (table 5) did not provide information about the estimated amounts of targeted cells being related to the PET signals. Preclinical experiments using reporter gene systems, made attempts to quantify PET signal related amounts of cells after local injection into animals, which were in comparable or slightly higher ranges to our findings with inherent differences, dependent from the used reporter system (table 22).

Reporter gene	Reporter probe	Detection limit	Reference
HSV1-sr39TK	[^{18}F]FHBG	*in vitro*: ~10^5 cells *in vivo:* ~10^7 cells	(Su et al. 2004)
hNET	[^{124}I]FIAU [^{124}I]MIBG	*in vivo:* ~10^4 cells	(Doubrovin et al. 2007)
hNET	[^{18}F]MFBG	*in vivo:* <10^5 cells	(Moroz et al. 2015)

hdCKDM	[^{18}F]FEAU	*in vivo:* ~3 x 10^5 cells	
HSV1-TK	[^{18}F]FEAU	*in vivo:* ~3 x 10^5 cells	
hNIS	^{124}I	*in vivo:* ~10^6 cells	

Table 22. Cellular detection limits of PET reporter gene systems after s.c. implantation.

The provided detection limits in different reporter systems reveal the high sensitivity in T-cell imaging by PET and is comparable to the sensitivity described in our study via immuno-PET. Nevertheless, the results are limited to locally applied cell spots and do not refer to quantification and detection during their intravital action.

The detection limit provided by our approach may also to be considered as estimated value, as the absolute numbers of transgenic T cells are determined instantly after PET imaging *ex vivo*. Through the technical procedure of producing single cell suspensions and staining for the subsequent flow cytometric quantification, a certain amount of the transgenic T cells may get lost leading to an underestimation of quantification values. However, we have shown, that the relative T-cell numbers correlate to the associated activity, which have been gathered *ex vivo* and image based by the corresponding PET scan. This speaks for the reliability of our developed technique and provides valuable information about specific T-cell enrichment at targeted sites, when signals from PET scans or related image-based data are evaluated.

It should be noted, that the sensitivity is also dependent from the technical sensitivity of preclinical and clinical PET scanners and the used radiotracer. The used Inveon small animal PET scanner in this study differs from its predecessor mainly by improved detector blocks, increasing its peak sensitivity up to three times (Shu et al. 2009). The image reconstruction was conducted via OSEM3D/MAP, being preferable in terms of uniform, high resolution and sensitivity compared to other reconstruction methods, such as rebinning and 2D reconstruction (Visser et al. 2009). Clinical PET scanners have lower spatial resolutions than preclinical scanners, which may influence the cellular detection limit, however currently a new clinical total-body PET/CT scanner is presented, which is characterized by an increased

sensitivity by a factor of ~40 for total-body imaging or a factor of ~4 - 5 for imaging a single organ and a 10 fold decreased acquisition time (Cherry et al. 2018). These technical advances open new possibilities for sensitive T-cell imaging and facilitate the clinical translation of this application in combination with an optimized radiotracer design (section 6.3).

6.5 CONCLUSIONS AND OUTLOOK

We developed non-invasive PET imaging technology for TCR-transgenic T cells harboring a murinized region in the constant beta domain of the TCR by the aid of the ^{89}Zr-labeled aTCRmu-F(ab')$_2$ fragment recognizing this specific sequence. The developed ^{89}Zr-Df-aTCRmu-F(ab')$_2$ radiotracer was in-depth characterized for its binding affinity, immunoreactivity and stability *in vitro* as well as *in vivo* and was qualified for the application *in vivo.* Furthermore, the impact on T-cell functionality wasn't impaired by direct radiotracer binding or by the ^{89}Zr derived radiation. In myeloid sarcoma xenograft models this tracking method resulted *in vivo* in highly specific PET signals at the targeted tumor site. The T-cell associated PET signals were evaluated *ex vivo* for their accuracy and the cellular detection limit in this experimental setting was determined. The detection limit of transgenic T cells was first measured after *in vitro* labeling with the radiotracer and subcutaneous application of different dilutions. The detection threshold was set in this assay at approximately 2 x 10^4 transgenic T cells. In the clinical relevant model, after transferring the transgenic T cells and the radiotracer i.v., *ex vivo* flow cytometric quantification of the T cells were consistent with this range, when the lowest related PET signal was considered. This finding was observed in several repetitive studies, when the engraftment rates differed between the experiments, confirming the reliability and consistency of the tracking technique. The detectable cell number thresholds were additionally supported by quantitative IHC analyses of the T-cell infiltrated tissues. Moreover, activity accumulation, deriving from *ex vivo* as well as PET

image-based data, was correlating to the total amounts of T cells present in the analyzed areas. These accurate and sensitive data give insights in specific T-cell accumulation at targeted sites and provide valuable information about the homing, proliferation as well as therapeutic action state of the transferred cells.

For a clinical application, this technology is worth to be further characterized and optimized in order to improve pharmacokinetics for a safe and suitable application in the clinical routine. Particularly, accuracy and sensitivity studies may be further exploited using smaller protein scaffold vectors in the currently evolving PET scanner systems. With this tracking strategy, we can explore different tumor-directed TCRs or T-cell marker, such CD2 or CD7, being suitable candidates for pan-T cell imaging in the context of T-cell distribution during different immunotherapies.

7 REFERENCES

Abou, D. S., T. Ku, and P. M. Smith-Jones. 2011. 'In vivo biodistribution and accumulation of 89Zr in mice', *Nucl Med Biol*, 38: 675-81.

Adonai, N., K. N. Nguyen, J. Walsh, M. Iyer, T. Toyokuni, M. E. Phelps, T. McCarthy, D. W. McCarthy, and S. S. Gambhir. 2002. 'Ex vivo cell labeling with 64Cu-pyruvaldehyde-bis(N4-methylthiosemicarbazone) for imaging cell trafficking in mice with positron-emission tomography', *Proc Natl Acad Sci U S A*, 99: 3030-5.

Ahmadzadeh, V., S. Farajnia, M. A. Feizi, and R. A. Nejad. 2014. 'Antibody humanization methods for development of therapeutic applications', *Monoclon Antib Immunodiagn Immunother*, 33: 67-73.

Antonios, J. P., H. Soto, R. G. Everson, D. L. Moughon, A. C. Wang, J. Orpilla, C. Radu, B. M. Ellingson, J. T. Lee, T. Cloughesy, M. E. Phelps, J. Czernin, L. M. Liau, and R. M. Prins. 2017. 'Detection of immune responses after immunotherapy in glioblastoma using PET and MRI', *Proc Natl Acad Sci U S A*, 114: 10220-25.

Bansal, A., M. K. Pandey, Y. E. Demirhan, J. J. Nesbitt, R. J. Crespo-Diaz, A. Terzic, A. Behfar, and T. R. DeGrado. 2015. 'Novel (89)Zr cell labeling approach for PET-based cell trafficking studies', *EJNMMI Res*, 5: 19.

Barrett, D. M., D. T. Teachey, and S. A. Grupp. 2014. 'Toxicity management for patients receiving novel T-cell engaging therapies', *Curr Opin Pediatr*, 26: 43-9.

Beatty, G. L., and W. L. Gladney. 2015. 'Immune escape mechanisms as a guide for cancer immunotherapy', *Clin Cancer Res*, 21: 687-92.

Bendle, G. M., C. Linnemann, A. I. Hooijkaas, L. Bies, M. A. de Witte, A. Jorritsma, A. D. Kaiser, N. Pouw, R. Debets, E. Kieback, W. Uckert, J. Y. Song, J. B. Haanen, and T. N. Schumacher. 2010. 'Lethal graft-versus-host disease in mouse models of T cell receptor gene therapy', *Nat Med*, 16: 565-70, 1 p following 70.

Berger, C., M. E. Flowers, E. H. Warren, and S. R. Riddell. 2006. 'Analysis of transgene-specific immune responses that limit the in vivo persistence of adoptively transferred HSV-TK-modified donor T cells after allogeneic hematopoietic cell transplantation', *Blood*, 107: 2294-302.

Berger, C., M. C. Jensen, P. M. Lansdorp, M. Gough, C. Elliott, and S. R. Riddell. 2008. 'Adoptive transfer of effector CD8+ T cells derived from central memory cells establishes persistent T cell memory in primates', *J Clin Invest*, 118: 294-305.

Bhargava, K. K., R. K. Gupta, K. J. Nichols, and C. J. Palestro. 2009. 'In vitro human leukocyte labeling with (64)Cu: an intraindividual comparison with (111)In-oxine and (18)F-FDG', *Nucl Med Biol*, 36: 545-9.

Bhatnagar, P., M. Alauddin, J. A. Bankson, D. Kirui, P. Seifi, H. Huls, D. A. Lee, A. Babakhani, M. Ferrari, K. C. Li, and L. J. Cooper. 2014. 'Tumor lysing genetically engineered T cells loaded with multi-modal imaging agents', *Sci Rep*, 4: 4502.

Biasco, L., S. Scala, L. Basso Ricci, F. Dionisio, C. Baricordi, A. Calabria, S. Giannelli, N. Cieri, F. Barzaghi, R. Pajno, H. Al-Mousa, A. Scarselli, C. Cancrini, C. Bordignon, M. G. Roncarolo, E. Montini, C. Bonini, and A. Aiuti. 2015. 'In vivo tracking of T cells in humans unveils decade-long survival and activity of genetically modified T memory stem cells', *Sci Transl Med*, 7: 273ra13.

Blankenstein, T., P. G. Coulie, E. Gilboa, and E. M. Jaffee. 2012. 'The determinants of tumour immunogenicity', *Nat Rev Cancer*, 12: 307-13.

Blumenthal, M., D. Skelton, K. A. Pepper, T. Jahn, E. Methangkool, and D. B. Kohn. 2007. 'Effective suicide gene therapy for leukemia in a model of insertional oncogenesis in mice', *Mol Ther*, 15: 183-92.

Boswell, C. A., and M. W. Brechbiel. 2007. 'Development of radioimmunotherapeutic and diagnostic antibodies: an inside-out view', *Nucl Med Biol*, 34: 757-78.

Botti, C., D. R. Negri, E. Seregni, V. Ramakrishna, F. Arienti, L. Maffioli, C. Lombardo, A. Bogni, C. Pascali, F. Crippa, S. Massaron, F. Remonti, S. Nerini-Molteni, S. Canevari,

and E. Bombardieri. 1997. 'Comparison of three different methods for radiolabelling human activated T lymphocytes', *Eur J Nucl Med*, 24: 497-504.

Brentjens, R. J., M. L. Davila, I. Riviere, J. Park, X. Wang, L. G. Cowell, S. Bartido, J. Stefanski, C. Taylor, M. Olszewska, O. Borquez-Ojeda, J. Qu, T. Wasielewska, Q. He, Y. Bernal, I. V. Rijo, C. Hedvat, R. Kobos, K. Curran, P. Steinherz, J. Jurcic, T. Rosenblat, P. Maslak, M. Frattini, and M. Sadelain. 2013. 'CD19-targeted T cells rapidly induce molecular remissions in adults with chemotherapy-refractory acute lymphoblastic leukemia', *Sci Transl Med*, 5: 177ra38.

Brentjens, R. J., I. Riviere, J. H. Park, M. L. Davila, X. Wang, J. Stefanski, C. Taylor, R. Yeh, S. Bartido, O. Borquez-Ojeda, M. Olszewska, Y. Bernal, H. Pegram, M. Przybylowski, D. Hollyman, Y. Usachenko, D. Pirraglia, J. Hosey, E. Santos, E. Halton, P. Maslak, D. Scheinberg, J. Jurcic, M. Heaney, G. Heller, M. Frattini, and M. Sadelain. 2011. 'Safety and persistence of adoptively transferred autologous CD19-targeted T cells in patients with relapsed or chemotherapy refractory B-cell leukemias', *Blood*, 118: 4817-28.

Bromberg, J. S., K. D. Chavin, P. Altevogt, B. A. Kyewski, B. Guckel, A. Naji, and C. F. Barker. 1991. 'Anti-CD2 monoclonal antibodies alter cell-mediated immunity in vivo', *Transplantation*, 51: 219-25.

Burnet, F. M. 1970. 'The concept of immunological surveillance', *Prog Exp Tumor Res*, 13: 1-27.

Cameron, B. J., A. B. Gerry, J. Dukes, J. V. Harper, V. Kannan, F. C. Bianchi, F. Grand, J. E. Brewer, M. Gupta, G. Plesa, G. Bossi, A. Vuidepot, A. S. Powlesland, A. Legg, K. J. Adams, A. D. Bennett, N. J. Pumphrey, D. D. Williams, G. Binder-Scholl, I. Kulikovskaya, B. L. Levine, J. L. Riley, A. Varela-Rohena, E. A. Stadtmauer, A. P. Rapoport, G. P. Linette, C. H. June, N. J. Hassan, M. Kalos, and B. K. Jakobsen. 2013. 'Identification of a Titin-derived HLA-A1-presented peptide as a cross-reactive target for engineered MAGE A3-directed T cells', *Sci Transl Med*, 5: 197ra03.

Casucci, M., R. E. Hawkins, G. Dotti, and A. Bondanza. 2015. 'Overcoming the toxicity hurdles of genetically targeted T cells', *Cancer Immunol Immunother*, 64: 123-30.

Chapuis, A. G., G. B. Ragnarsson, H. N. Nguyen, C. N. Chaney, J. S. Pufnock, T. M. Schmitt, N. Duerkopp, I. M. Roberts, G. L. Pogosov, W. Y. Ho, S. Ochsenreither, M. Wolfl, M. Bar, J. P. Radich, C. Yee, and P. D. Greenberg. 2013. 'Transferred WT1-reactive CD8+ T cells can mediate antileukemic activity and persist in post-transplant patients', *Sci Transl Med*, 5: 174ra27.

Charo, J., C. Perez, C. Buschow, A. Jukica, M. Czeh, and T. Blankenstein. 2011. 'Visualizing the dynamic of adoptively transferred T cells during the rejection of large established tumors', *Eur J Immunol*, 41: 3187-97.

Charoenphun, P., L. K. Meszaros, K. Chuamsaamarkkee, E. Sharif-Paghaleh, J. R. Ballinger, T. J. Ferris, M. J. Went, G. E. Mullen, and P. J. Blower. 2015. '[(89)Zr]oxinate4 for long-term in vivo cell tracking by positron emission tomography', *Eur J Nucl Med Mol Imaging*, 42: 278-87.

Chen, C. L., T. Y. Siow, C. H. Chou, C. H. Lin, M. H. Lin, Y. C. Chen, W. Y. Hsieh, S. J. Wang, and C. Chang. 2017. 'Targeted Superparamagnetic Iron Oxide Nanoparticles for In Vivo Magnetic Resonance Imaging of T-Cells in Rheumatoid Arthritis', *Mol Imaging Biol*, 19: 233-44.

Cherry, S. R., T. Jones, J. S. Karp, J. Qi, W. W. Moses, and R. D. Badawi. 2018. 'Total-Body PET: Maximizing Sensitivity to Create New Opportunities for Clinical Research and Patient Care', *J Nucl Med*, 59: 3-12.

Chewning, J. H., K. J. Dugger, T. R. Chaudhuri, K. R. Zinn, and C. T. Weaver. 2009. 'Bioluminescence-based visualization of CD4 T cell dynamics using a T lineage-specific luciferase transgenic model', *BMC Immunol*, 10: 44.

Cohen, C. J., Y. Zhao, Z. Zheng, S. A. Rosenberg, and R. A. Morgan. 2006. 'Enhanced antitumor activity of murine-human hybrid T-cell receptor (TCR) in human

lymphocytes is associated with improved pairing and TCR/CD3 stability', *Cancer Res*, 66: 8878-86.

Datz, F. L. 1994. 'Indium-111-labeled leukocytes for the detection of infection: current status', *Semin Nucl Med*, 24: 92-109.

Davila, M. L., and R. Brentjens. 2013. 'Chimeric antigen receptor therapy for chronic lymphocytic leukemia: what are the challenges?', *Hematol Oncol Clin North Am*, 27: 341-53.

Davis, J. L., M. R. Theoret, Z. Zheng, C. H. Lamers, S. A. Rosenberg, and R. A. Morgan. 2010. 'Development of human anti-murine T-cell receptor antibodies in both responding and nonresponding patients enrolled in TCR gene therapy trials', *Clin Cancer Res*, 16: 5852-61.

Deri, M. A., S. Ponnala, P. Kozlowski, B. P. Burton-Pye, H. T. Cicek, C. Hu, J. S. Lewis, and L. C. Francesconi. 2015. 'p-SCN-Bn-HOPO: A Superior Bifunctional Chelator for (89)Zr ImmunoPET', *Bioconjug Chem*, 26: 2579-91.

Deri, M. A., B. M. Zeglis, L. C. Francesconi, and J. S. Lewis. 2013. 'PET imaging with (8)(9)Zr: from radiochemistry to the clinic', *Nucl Med Biol*, 40: 3-14.

Dijkers, E. C., J. G. Kosterink, A. P. Rademaker, L. R. Perk, G. A. van Dongen, J. Bart, J. R. de Jong, E. G. de Vries, and M. N. Lub-de Hooge. 2009. 'Development and characterization of clinical-grade 89Zr-trastuzumab for HER2/neu immunoPET imaging', *J Nucl Med*, 50: 974-81.

Dobrenkov, K., M. Olszewska, Y. Likar, L. Shenker, G. Gunset, S. Cai, N. Pillarsetty, H. Hricak, M. Sadelain, and V. Ponomarev. 2008. 'Monitoring the efficacy of adoptively transferred prostate cancer-targeted human T lymphocytes with PET and bioluminescence imaging', *J Nucl Med*, 49: 1162-70.

Doubrovin, M. M., E. S. Doubrovina, P. Zanzonico, M. Sadelain, S. M. Larson, and R. J. O'Reilly. 2007. 'In vivo imaging and quantitation of adoptively transferred human antigen-specific T cells transduced to express a human norepinephrine transporter gene', *Cancer Res*, 67: 11959-69.

Drobyski, W. R., and D. Majewski. 1996. 'Treatment of donor mice with an alpha beta T-cell receptor monoclonal antibody induces prolonged T-cell nonresponsiveness and effectively prevents lethal graft-versus-host disease in murine recipients of major histocompatibility complex (MHC)-matched and MHC-mismatched donor marrow grafts', *Blood*, 87: 5355-69.

Dubey, P., H. Su, N. Adonai, S. Du, A. Rosato, J. Braun, S. S. Gambhir, and O. N. Witte. 2003. 'Quantitative imaging of the T cell antitumor response by positron-emission tomography', *Proc Natl Acad Sci U S A*, 100: 1232-7.

Dudley, M. E., C. A. Gross, M. M. Langhan, M. R. Garcia, R. M. Sherry, J. C. Yang, G. Q. Phan, U. S. Kammula, M. S. Hughes, D. E. Citrin, N. P. Restifo, J. R. Wunderlich, P. A. Prieto, J. J. Hong, R. C. Langan, D. A. Zlott, K. E. Morton, D. E. White, C. M. Laurencot, and S. A. Rosenberg. 2010. 'CD8+ enriched "young" tumor infiltrating lymphocytes can mediate regression of metastatic melanoma', *Clin Cancer Res*, 16: 6122-31.

Dudley, M. E., J. C. Yang, R. Sherry, M. S. Hughes, R. Royal, U. Kammula, P. F. Robbins, J. Huang, D. E. Citrin, S. F. Leitman, J. Wunderlich, N. P. Restifo, A. Thomasian, S. G. Downey, F. O. Smith, J. Klapper, K. Morton, C. Laurencot, D. E. White, and S. A. Rosenberg. 2008. 'Adoptive cell therapy for patients with metastatic melanoma: evaluation of intensive myeloablative chemoradiation preparative regimens', *J Clin Oncol*, 26: 5233-9.

Ecker, D. M., S. D. Jones, and H. L. Levine. 2015. 'The therapeutic monoclonal antibody market', *MAbs*, 7: 9-14.

England, C. G., D. Jiang, E. B. Ehlerding, B. T. Rekoske, P. A. Ellison, R. Hernandez, T. E. Barnhart, D. G. McNeel, P. Huang, and W. Cai. 2017. '89Zr-labeled nivolumab for imaging of T-cell infiltration in a humanized murine model of lung cancer', *Eur J Nucl Med Mol Imaging*.

Ertl, H. C., J. Zaia, S. A. Rosenberg, C. H. June, G. Dotti, J. Kahn, L. J. Cooper, J. Corrigan-Curay, and S. E. Strome. 2011. 'Considerations for the clinical application of chimeric antigen receptor T cells: observations from a recombinant DNA Advisory Committee Symposium held June 15, 2010', *Cancer Res*, 71: 3175-81.

Fairclough, M., C. Prenant, B. Ellis, H. Boutin, A. McMahon, G. Brown, P. Locatelli, and A. K. Jones. 2016. 'A new technique for the radiolabelling of mixed leukocytes with zirconium-89 for inflammation imaging with positron emission tomography', *J Labelled Comp Radiopharm*, 59: 270-6.

Ferlay, J., I. Soerjomataram, R. Dikshit, S. Eser, C. Mathers, M. Rebelo, D. M. Parkin, D. Forman, and F. Bray. 2015. 'Cancer incidence and mortality worldwide: sources, methods and major patterns in GLOBOCAN 2012', *Int J Cancer*, 136: E359-86.

Fesnak, A. D., C. H. June, and B. L. Levine. 2016. 'Engineered T cells: the promise and challenges of cancer immunotherapy', *Nat Rev Cancer*, 16: 566-81.

Forstrom, L. A., B. P. Mullan, J. C. Hung, V. J. Lowe, and L. M. Thorson. 2000. '18F-FDG labelling of human leukocytes', *Nucl Med Commun*, 21: 691-4.

Freise, A. C., K. A. Zettlitz, F. B. Salazar, X. Lu, R. Tavare, and A. M. Wu. 2017. 'ImmunoPET Imaging of Murine CD4+ T Cells Using Anti-CD4 Cys-Diabody: Effects of Protein Dose on T Cell Function and Imaging', *Mol Imaging Biol*, 19: 599-609.

Gambhir, S. S. 2002. 'Molecular imaging of cancer with positron emission tomography', *Nat Rev Cancer*, 2: 683-93.

Gattinoni, L., S. E. Finkelstein, C. A. Klebanoff, P. A. Antony, D. C. Palmer, P. J. Spiess, L. N. Hwang, Z. Yu, C. Wrzesinski, D. M. Heimann, C. D. Surh, S. A. Rosenberg, and N. P. Restifo. 2005. 'Removal of homeostatic cytokine sinks by lymphodepletion enhances the efficacy of adoptively transferred tumor-specific CD8+ T cells', *J Exp Med*, 202: 907-12.

Gattinoni, L., E. Lugli, Y. Ji, Z. Pos, C. M. Paulos, M. F. Quigley, J. R. Almeida, E. Gostick, Z. Yu, C. Carpenito, E. Wang, D. C. Douek, D. A. Price, C. H. June, F. M. Marincola, M. Roederer, and N. P. Restifo. 2011. 'A human memory T cell subset with stem cell-like properties', *Nat Med*, 17: 1290-7.

Gattinoni, L., D. J. Powell, Jr., S. A. Rosenberg, and N. P. Restifo. 2006. 'Adoptive immunotherapy for cancer: building on success', *Nat Rev Immunol*, 6: 383-93.

Gattinoni, L., X. S. Zhong, D. C. Palmer, Y. Ji, C. S. Hinrichs, Z. Yu, C. Wrzesinski, A. Boni, L. Cassard, L. M. Garvin, C. M. Paulos, P. Muranski, and N. P. Restifo. 2009. 'Wnt signaling arrests effector T cell differentiation and generates CD8+ memory stem cells', *Nat Med*, 15: 808-13.

Gonzales, C., H. A. Yoshihara, N. Dilek, J. Leignadier, M. Irving, P. Mieville, L. Helm, O. Michielin, and J. Schwitter. 2016. 'In-Vivo Detection and Tracking of T Cells in Various Organs in a Melanoma Tumor Model by 19F-Fluorine MRS/MRI', *PLoS One*, 11: e0164557.

Griessinger, C. M., R. Kehlbach, D. Bukala, S. Wiehr, R. Bantleon, F. Cay, A. Schmid, H. Braumuller, B. Fehrenbacher, M. Schaller, M. Eichner, J. L. Sutcliffe, W. Ehrlichmann, O. Eibl, G. Reischl, S. R. Cherry, M. Rocken, B. J. Pichler, and M. Kneilling. 2014. 'In vivo tracking of Th1 cells by PET reveals quantitative and temporal distribution and specific homing in lymphatic tissue', *J Nucl Med*, 55: 301-7.

Griessinger, C. M., A. Maurer, C. Kesenheimer, R. Kehlbach, G. Reischl, W. Ehrlichmann, D. Bukala, M. Harant, F. Cay, J. Bruck, R. Nordin, U. Kohlhofer, H. G. Rammensee, L. Quintanilla-Martinez, M. Schaller, M. Rocken, B. J. Pichler, and M. Kneilling. 2015. '64Cu antibody-targeting of the T-cell receptor and subsequent internalization enables in vivo tracking of lymphocytes by PET', *Proc Natl Acad Sci U S A*, 112: 1161-6.

Grupp, S. A., M. Kalos, D. Barrett, R. Aplenc, D. L. Porter, S. R. Rheingold, D. T. Teachey, A. Chew, B. Hauck, J. F. Wright, M. C. Milone, B. L. Levine, and C. H. June. 2013. 'Chimeric antigen receptor-modified T cells for acute lymphoid leukemia', *N Engl J Med*, 368: 1509-18.

Gschweng, E. H., M. N. McCracken, M. L. Kaufman, M. Ho, R. P. Hollis, X. Wang, N. Saini, R. C. Koya, T. Chodon, A. Ribas, O. N. Witte, and D. B. Kohn. 2014. 'HSV-sr39TK positron emission tomography and suicide gene elimination of human hematopoietic stem cells and their progeny in humanized mice', *Cancer Res*, 74: 5173-83.

Harris, D. T., and D. M. Kranz. 2016. 'Adoptive T Cell Therapies: A Comparison of T Cell Receptors and Chimeric Antigen Receptors', *Trends Pharmacol Sci*, 37: 220-30.

Hart, D. P., S. A. Xue, S. Thomas, M. Cesco-Gaspere, A. Tranter, B. Willcox, S. P. Lee, N. Steven, E. C. Morris, and H. J. Stauss. 2008. 'Retroviral transfer of a dominant TCR prevents surface expression of a large proportion of the endogenous TCR repertoire in human T cells', *Gene Ther*, 15: 625-31.

Heemskerk, M. H., M. Hoogeboom, R. A. de Paus, M. G. Kester, M. A. van der Hoorn, E. Goulmy, R. Willemze, and J. H. Falkenburg. 2003. 'Redirection of antileukemic reactivity of peripheral T lymphocytes using gene transfer of minor histocompatibility antigen HA-2-specific T-cell receptor complexes expressing a conserved alpha joining region', *Blood*, 102: 3530-40.

Herschman, H. R. 2004. 'PET reporter genes for noninvasive imaging of gene therapy, cell tracking and transgenic analysis', *Crit Rev Oncol Hematol*, 51: 191-204.

Heskamp, S., R. Raave, O. Boerman, M. Rijpkema, V. Goncalves, and F. Denat. 2017. '(89)Zr-Immuno-Positron Emission Tomography in Oncology: State-of-the-Art (89)Zr Radiochemistry', *Bioconjug Chem*, 28: 2211-23.

Heskamp, S., H. W. van Laarhoven, J. D. Molkenboer-Kuenen, G. M. Franssen, Y. M. Versleijen-Jonkers, W. J. Oyen, W. T. van der Graaf, and O. C. Boerman. 2010. 'ImmunoSPECT and immunoPET of IGF-1R expression with the radiolabeled antibody R1507 in a triple-negative breast cancer model', *J Nucl Med*, 51: 1565-72.

Hildebrandt, I. J., and S. S. Gambhir. 2004. 'Molecular imaging applications for immunology', *Clin Immunol*, 111: 210-24.

Hitchens, T. K., L. Liu, L. M. Foley, V. Simplaceanu, E. T. Ahrens, and C. Ho. 2015. 'Combining perfluorocarbon and superparamagnetic iron-oxide cell labeling for improved and expanded applications of cellular MRI', *Magn Reson Med*, 73: 367-75.

Holliger, P., and P. J. Hudson. 2005. 'Engineered antibody fragments and the rise of single domains', *Nat Biotechnol*, 23: 1126-36.

Hoos, A. 2012. 'Evolution of end points for cancer immunotherapy trials', *Ann Oncol*, 23 Suppl 8: viii47-52.

Hu, Q., J. Peng, W. Liu, X. He, L. Cui, X. Chen, M. Yang, H. Liu, S. Liu, and H. Wang. 2014. 'Elevated cleaved caspase-3 is associated with shortened overall survival in several cancer types', *Int J Clin Exp Pathol*, 7: 5057-70.

Hughes, D. K. 2003. 'Nuclear medicine and infection detection: the relative effectiveness of imaging with 111In-oxine-, 99mTc-HMPAO-, and 99mTc-stannous fluoride colloid-labeled leukocytes and with 67 Ga-citrate', *J Nucl Med Technol*, 31: 196-201; quiz 03-4.

Irmler, I. M., T. Opfermann, P. Gebhardt, M. Gajda, R. Brauer, H. P. Saluz, and T. Kamradt. 2010. 'In vivo molecular imaging of experimental joint inflammation by combined (18)F-FDG positron emission tomography and computed tomography', *Arthritis Res Ther*, 12: R203.

Jin, W. N., X. Yang, Z. Li, M. Li, S. X. Shi, K. Wood, Q. Liu, Y. Fu, W. Han, Y. Xu, F. D. Shi, and Q. Liu. 2016. 'Non-invasive tracking of CD4+ T cells with a paramagnetic and fluorescent nanoparticle in brain ischemia', *J Cereb Blood Flow Metab*, 36: 1464-76.

Johnson, L. A., R. A. Morgan, M. E. Dudley, L. Cassard, J. C. Yang, M. S. Hughes, U. S. Kammula, R. E. Royal, R. M. Sherry, J. R. Wunderlich, C. C. Lee, N. P. Restifo, S. L. Schwarz, A. P. Cogdill, R. J. Bishop, H. Kim, C. C. Brewer, S. F. Rudy, C. VanWaes, J. L. Davis, A. Mathur, R. T. Ripley, D. A. Nathan, C. M. Laurencot, and S. A. Rosenberg. 2009. 'Gene therapy with human and mouse T-cell receptors mediates cancer regression and targets normal tissues expressing cognate antigen', *Blood*, 114: 535-46.

Kakarla, S., and S. Gottschalk. 2014. 'CAR T cells for solid tumors: armed and ready to go?', *Cancer J*, 20: 151-5.

Kalos, M., B. L. Levine, D. L. Porter, S. Katz, S. A. Grupp, A. Bagg, and C. H. June. 2011. 'T cells with chimeric antigen receptors have potent antitumor effects and can establish memory in patients with advanced leukemia', *Sci Transl Med*, 3: 95ra73.

Khong, H. T., and N. P. Restifo. 2002. 'Natural selection of tumor variants in the generation of "tumor escape" phenotypes', *Nat Immunol*, 3: 999-1005.

Kircher, M. F., J. R. Allport, E. E. Graves, V. Love, L. Josephson, A. H. Lichtman, and R. Weissleder. 2003. 'In vivo high resolution three-dimensional imaging of antigen-specific cytotoxic T-lymphocyte trafficking to tumors', *Cancer Res*, 63: 6838-46.

Kircher, M. F., S. S. Gambhir, and J. Grimm. 2011. 'Noninvasive cell-tracking methods', *Nat Rev Clin Oncol*, 8: 677-88.

Klar, R., S. Schober, M. Rami, S. Mall, J. Merl, S. M. Hauck, M. Ueffing, A. Admon, J. Slotta-Huspenina, M. Schwaiger, S. Stevanovic, R. A. Oostendorp, D. H. Busch, C. Peschel, and A. M. Krackhardt. 2014. 'Therapeutic targeting of naturally presented myeloperoxidase-derived HLA peptide ligands on myeloid leukemia cells by TCR-transgenic T cells', *Leukemia*, 28: 2355-66.

Klebanoff, C. A., S. E. Finkelstein, D. R. Surman, M. K. Lichtman, L. Gattinoni, M. R. Theoret, N. Grewal, P. J. Spiess, P. A. Antony, D. C. Palmer, Y. Tagaya, S. A. Rosenberg, T. A. Waldmann, and N. P. Restifo. 2004. 'IL-15 enhances the in vivo antitumor activity of tumor-reactive CD8+ T cells', *Proc Natl Acad Sci U S A*, 101: 1969-74.

Klebanoff, C. A., L. Gattinoni, and N. P. Restifo. 2006. 'CD8+ T-cell memory in tumor immunology and immunotherapy', *Immunol Rev*, 211: 214-24.

———. 2012. 'Sorting through subsets: which T-cell populations mediate highly effective adoptive immunotherapy?', *J Immunother*, 35: 651-60.

Klebanoff, C. A., L. Gattinoni, P. Torabi-Parizi, K. Kerstann, A. R. Cardones, S. E. Finkelstein, D. C. Palmer, P. A. Antony, S. T. Hwang, S. A. Rosenberg, T. A. Waldmann, and N. P. Restifo. 2005. 'Central memory self/tumor-reactive CD8+ T cells confer superior antitumor immunity compared with effector memory T cells', *Proc Natl Acad Sci U S A*, 102: 9571-6.

Klebanoff, C. A., H. T. Khong, P. A. Antony, D. C. Palmer, and N. P. Restifo. 2005. 'Sinks, suppressors and antigen presenters: how lymphodepletion enhances T cell-mediated tumor immunotherapy', *Trends Immunol*, 26: 111-7.

Kochenderfer, J. N., M. E. Dudley, S. A. Feldman, W. H. Wilson, D. E. Spaner, I. Maric, M. Stetler-Stevenson, G. Q. Phan, M. S. Hughes, R. M. Sherry, J. C. Yang, U. S. Kammula, L. Devillier, R. Carpenter, D. A. Nathan, R. A. Morgan, C. Laurencot, and S. A. Rosenberg. 2012. 'B-cell depletion and remissions of malignancy along with cytokine-associated toxicity in a clinical trial of anti-CD19 chimeric-antigen-receptor-transduced T cells', *Blood*, 119: 2709-20.

Koehne, G., M. Doubrovin, E. Doubrovina, P. Zanzonico, H. F. Gallardo, A. Ivanova, J. Balatoni, J. Teruya-Feldstein, G. Heller, C. May, V. Ponomarev, S. Ruan, R. Finn, R. G. Blasberg, W. Bornmann, I. Riviere, M. Sadelain, R. J. O'Reilly, S. M. Larson, and J. G. Tjuvajev. 2003. 'Serial in vivo imaging of the targeted migration of human HSV-TK-transduced antigen-specific lymphocytes', *Nat Biotechnol*, 21: 405-13.

Kuball, J., M. L. Dossett, M. Wolfl, W. Y. Ho, R. H. Voss, C. Fowler, and P. D. Greenberg. 2007. 'Facilitating matched pairing and expression of TCR chains introduced into human T cells', *Blood*, 109: 2331-8.

Kuball, J., B. Hauptrock, V. Malina, E. Antunes, R. H. Voss, M. Wolfl, R. Strong, M. Theobald, and P. D. Greenberg. 2009. 'Increasing functional avidity of TCR-redirected T cells by removing defined N-glycosylation sites in the TCR constant domain', *J Exp Med*, 206: 463-75.

Kubo, R. T., W. Born, J. W. Kappler, P. Marrack, and M. Pigeon. 1989. 'Characterization of a monoclonal antibody which detects all murine alpha beta T cell receptors', *J Immunol*, 142: 2736-42.

Kummer, U., U. Zengerle, J. Pischel, B. Trautmann, R. Mailhammer, and N. Sidell. 2001. 'Increased in vivo mitogenicity of anti-TCR/CD3 monoclonal antibody through reduced interaction with Fcgamma receptors', *Immunol Lett*, 75: 153-8.

Lacroix, S., D. Egrise, G. Van Simaeys, G. Doumont, M. Monclus, F. Sherer, T. Herbaux, D. Leroy, and S. Goldman. 2013. '[18F]-FBEM, a tracer targeting cell-surface protein thiols for cell trafficking imaging', *Contrast Media Mol Imaging*, 8: 409-16.

Lamers, C. H., S. Sleijfer, S. van Steenbergen, P. van Elzakker, B. van Krimpen, C. Groot, A. Vulto, M. den Bakker, E. Oosterwijk, R. Debets, and J. W. Gratama. 2013. 'Treatment of metastatic renal cell carcinoma with CAIX CAR-engineered T cells: clinical evaluation and management of on-target toxicity', *Mol Ther*, 21: 904-12.

Lamers, C. H., S. Sleijfer, A. G. Vulto, W. H. Kruit, M. Kliffen, R. Debets, J. W. Gratama, G. Stoter, and E. Oosterwijk. 2006. 'Treatment of metastatic renal cell carcinoma with autologous T-lymphocytes genetically retargeted against carbonic anhydrase IX: first clinical experience', *J Clin Oncol*, 24: e20-2.

Latinne, D., B. De La Parra, Y. Nizet, A. Cornet, V. Giovino-Barry, R. L. Monroy, M. E. White-Scharf, and H. Bazin. 1996. 'An anti-CD2 mAb induces immunosuppression and hyporesponsiveness of CD2+ human T cells in vitro', *Int Immunol*, 8: 1113-9.

Lee, D. W., J. N. Kochenderfer, M. Stetler-Stevenson, Y. K. Cui, C. Delbrook, S. A. Feldman, T. J. Fry, R. Orentas, M. Sabatino, N. N. Shah, S. M. Steinberg, D. Stroncek, N. Tschernia, C. Yuan, H. Zhang, L. Zhang, S. A. Rosenberg, A. S. Wayne, and C. L. Mackall. 2015. 'T cells expressing CD19 chimeric antigen receptors for acute lymphoblastic leukaemia in children and young adults: a phase 1 dose-escalation trial', *Lancet*, 385: 517-28.

Leech, J. M., E. Sharif-Paghaleh, J. Maher, L. Livieratos, R. I. Lechler, G. E. Mullen, G. Lombardi, and L. A. Smyth. 2013. 'Whole-body imaging of adoptively transferred T cells using magnetic resonance imaging, single photon emission computed tomography and positron emission tomography techniques, with a focus on regulatory T cells', *Clin Exp Immunol*, 172: 169-77.

Li, A., Y. Wu, F. Tang, W. Li, X. Feng, and Z. Yao. 2016. 'In Vivo Magnetic Resonance Imaging of CD8+ T Lymphocytes Recruiting to Glioblastoma in Mice', *Cancer Biother Radiopharm*, 31: 317-23.

Likar, Y., J. Zurita, K. Dobrenkov, L. Shenker, S. Cai, A. Neschadim, J. A. Medin, M. Sadelain, H. Hricak, and V. Ponomarev. 2010. 'A new pyrimidine-specific reporter gene: a mutated human deoxycytidine kinase suitable for PET during treatment with acycloguanosine-based cytotoxic drugs', *J Nucl Med*, 51: 1395-403.

Lin, J., K. D. Chavin, L. Qin, Y. Ding, and J. S. Bromberg. 1996. 'Anti-CD2 monoclonal antibody-induced receptor changes. II. Interaction of CD2 and CD3', *Cell Immunol*, 167: 249-58.

Lin, J., R. W. Yon, K. D. Chavin, L. Qin, J. Woodward, Y. Ding, H. Yagita, and J. S. Bromberg. 1995. 'Anti-CD2 monoclonal antibody-induced receptor changes: down modulation of cell surface CD2', *Transplantation*, 59: 1162-71.

Lindenberg, L., S. Adler, I. B. Turkbey, F. Mertan, A. Ton, K. Do, S. Kummar, E. M. Gonzalez, S. Bhattacharyya, P. M. Jacobs, and P. Choyke. 2017. 'Dosimetry and first human experience with (89)Zr-panitumumab', *Am J Nucl Med Mol Imaging*, 7: 195-203.

Lindmo, T., E. Boven, F. Cuttitta, J. Fedorko, and P. A. Bunn, Jr. 1984. 'Determination of the immunoreactive fraction of radiolabeled monoclonal antibodies by linear extrapolation to binding at infinite antigen excess', *J Immunol Methods*, 72: 77-89.

Linette, G. P., E. A. Stadtmauer, M. V. Maus, A. P. Rapoport, B. L. Levine, L. Emery, L. Litzky, A. Bagg, B. M. Carreno, P. J. Cimino, G. K. Binder-Scholl, D. P. Smethurst, A. B. Gerry, N. J. Pumphrey, A. D. Bennett, J. E. Brewer, J. Dukes, J. Harper, H. K.

Tayton-Martin, B. K. Jakobsen, N. J. Hassan, M. Kalos, and C. H. June. 2013. 'Cardiovascular toxicity and titin cross-reactivity of affinity-enhanced T cells in myeloma and melanoma', *Blood*, 122: 863-71.

Liu, P. F., Y. C. Hu, B. H. Kang, Y. K. Tseng, P. C. Wu, C. C. Liang, Y. Y. Hou, T. Y. Fu, H. H. Liou, I. C. Hsieh, L. P. Ger, and C. W. Shu. 2017. 'Expression levels of cleaved caspase-3 and caspase-3 in tumorigenesis and prognosis of oral tongue squamous cell carcinoma', *PLoS One*, 12: e0180620.

Liu, Z., and Z. Li. 2014. 'Molecular imaging in tracking tumor-specific cytotoxic T lymphocytes (CTLs)', *Theranostics*, 4: 990-1001.

Lomax, M. E., L. K. Folkes, and P. O'Neill. 2013. 'Biological consequences of radiation-induced DNA damage: relevance to radiotherapy', *Clin Oncol (R Coll Radiol)*, 25: 578-85.

Lundin, J., E. Kimby, M. Bjorkholm, P. A. Broliden, F. Celsing, V. Hjalmar, L. Mollgard, P. Rebello, G. Hale, H. Waldmann, H. Mellstedt, and A. Osterborg. 2002. 'Phase II trial of subcutaneous anti-CD52 monoclonal antibody alemtuzumab (Campath-1H) as first-line treatment for patients with B-cell chronic lymphocytic leukemia (B-CLL)', *Blood*, 100: 768-73.

Macedo, C., J. T. Walters, E. A. Orkis, K. Isse, B. D. Elinoff, S. P. Fedorek, J. M. McMichael, G. Chalasani, P. Randhawa, A. J. Demetris, A. Zeevi, H. Tan, R. Shapiro, D. Landsittel, F. G. Lakkis, and D. Metes. 2012. 'Long-term effects of alemtuzumab on regulatory and memory T-cell subsets in kidney transplantation', *Transplantation*, 93: 813-21.

Maher, J. 2012. 'Immunotherapy of malignant disease using chimeric antigen receptor engrafted T cells', *ISRN Oncol*, 2012: 278093.

Mall, S., N. Yusufi, R. Wagner, R. Klar, H. Bianchi, K. Steiger, M. Straub, S. Audehm, I. Laitinen, M. Aichler, C. Peschel, S. Ziegler, M. Mustafa, M. Schwaiger, C. D'Alessandria, and A. M. Krackhardt. 2016. 'Immuno-PET Imaging of Engineered Human T Cells in Tumors', *Cancer Res*.

Matsui, T., N. Nakata, S. Nagai, A. Nakatani, M. Takahashi, T. Momose, K. Ohtomo, and S. Koyasu. 2009. 'Inflammatory cytokines and hypoxia contribute to 18F-FDG uptake by cells involved in pannus formation in rheumatoid arthritis', *J Nucl Med*, 50: 920-6.

Maude, S. L., N. Frey, P. A. Shaw, R. Aplenc, D. M. Barrett, N. J. Bunin, A. Chew, V. E. Gonzalez, Z. Zheng, S. F. Lacey, Y. D. Mahnke, J. J. Melenhorst, S. R. Rheingold, A. Shen, D. T. Teachey, B. L. Levine, C. H. June, D. L. Porter, and S. A. Grupp. 2014. 'Chimeric antigen receptor T cells for sustained remissions in leukemia', *N Engl J Med*, 371: 1507-17.

Maus, M. V., S. A. Grupp, D. L. Porter, and C. H. June. 2014. 'Antibody-modified T cells: CARs take the front seat for hematologic malignancies', *Blood*, 123: 2625-35.

McCracken, M. N., E. H. Gschweng, E. Nair-Gill, J. McLaughlin, A. R. Cooper, M. Riedinger, D. Cheng, C. Nosala, D. B. Kohn, and O. N. Witte. 2013. 'Long-term in vivo monitoring of mouse and human hematopoietic stem cell engraftment with a human positron emission tomography reporter gene', *Proc Natl Acad Sci U S A*, 110: 1857-62.

McCracken, M. N., R. Tavare, O. N. Witte, and A. M. Wu. 2016. 'Advances in PET Detection of the Antitumor T Cell Response', *Adv Immunol*, 131: 187-231.

McCracken, M. N., D. N. Vatakis, D. Dixit, J. McLaughlin, J. A. Zack, and O. N. Witte. 2015. 'Noninvasive detection of tumor-infiltrating T cells by PET reporter imaging', *J Clin Invest*, 125: 1815-26.

Mezzanotte, L., V. Blankevoort, C. W. Lowik, and E. L. Kaijzel. 2014. 'A novel luciferase fusion protein for highly sensitive optical imaging: from single-cell analysis to in vivo whole-body bioluminescence imaging', *Anal Bioanal Chem*, 406: 5727-34.

Milenic, D. E., E. D. Brady, and M. W. Brechbiel. 2004. 'Antibody-targeted radiation cancer therapy', *Nat Rev Drug Discov*, 3: 488-99.

Morgan, R. A., N. Chinnasamy, D. Abate-Daga, A. Gros, P. F. Robbins, Z. Zheng, M. E. Dudley, S. A. Feldman, J. C. Yang, R. M. Sherry, G. Q. Phan, M. S. Hughes, U. S. Kammula, A. D. Miller, C. J. Hessman, A. A. Stewart, N. P. Restifo, M. M. Quezado, M. Alimchandani, A. Z. Rosenberg, A. Nath, T. Wang, B. Bielekova, S. C. Wuest, N. Akula, F. J. McMahon, S. Wilde, B. Mosetter, D. J. Schendel, C. M. Laurencot, and S. A. Rosenberg. 2013. 'Cancer regression and neurological toxicity following anti-MAGE-A3 TCR gene therapy', *J Immunother*, 36: 133-51.

Morgan, R. A., M. E. Dudley, J. R. Wunderlich, M. S. Hughes, J. C. Yang, R. M. Sherry, R. E. Royal, S. L. Topalian, U. S. Kammula, N. P. Restifo, Z. Zheng, A. Nahvi, C. R. de Vries, L. J. Rogers-Freezer, S. A. Mavroukakis, and S. A. Rosenberg. 2006. 'Cancer regression in patients after transfer of genetically engineered lymphocytes', *Science*, 314: 126-9.

Moroz, M. A., H. Zhang, J. Lee, E. Moroz, J. Zurita, L. Shenker, I. Serganova, R. Blasberg, and V. Ponomarev. 2015. 'Comparative Analysis of T Cell Imaging with Human Nuclear Reporter Genes', *J Nucl Med*, 56: 1055-60.

Nair, A. B., and S. Jacob. 2016. 'A simple practice guide for dose conversion between animals and human', *J Basic Clin Pharm*, 7: 27-31.

Nair-Gill, E., S. M. Wiltzius, X. X. Wei, D. Cheng, M. Riedinger, C. G. Radu, and O. N. Witte. 2010. 'PET probes for distinct metabolic pathways have different cell specificities during immune responses in mice', *J Clin Invest*, 120: 2005-15.

Nguyen, Q. T., and R. Y. Tsien. 2013. 'Fluorescence-guided surgery with live molecular navigation--a new cutting edge', *Nat Rev Cancer*, 13: 653-62.

Nishimura, Y., M. Eto, T. Maeda, K. Hiromatsu, N. Kobayashi, K. Nomoto, Y. Y. Kong, and K. Nomoto. 1994. 'Inhibition of skin xenograft rejection by depleting T-cell receptor alpha beta-bearing cells without T-cell receptor gamma delta-bearing cells or natural killer cells by monoclonal antibody', *Immunology*, 83: 196-204.

Nizet, Y., A. A. Chentoufi, X. Havaux, I. Kinet, F. Cormont, H. Bazin, and D. Latinne. 1999. 'Apoptosis of human naive NK cells mediated by a rat IgG2b anti CD2 mAb through a fractricidal ADCC reaction', *Immunol Lett*, 68: 229-35.

Ogino, S., J. Galon, C. S. Fuchs, and G. Dranoff. 2011. 'Cancer immunology--analysis of host and tumor factors for personalized medicine', *Nat Rev Clin Oncol*, 8: 711-9.

Parente-Pereira, A. C., J. Burnet, D. Ellison, J. Foster, D. M. Davies, S. van der Stegen, S. Burbridge, L. Chiapero-Stanke, S. Wilkie, S. Mather, and J. Maher. 2011. 'Trafficking of CAR-engineered human T cells following regional or systemic adoptive transfer in SCID beige mice', *J Clin Immunol*, 31: 710-8.

Park, J. R., D. L. Digiusto, M. Slovak, C. Wright, A. Naranjo, J. Wagner, H. B. Meechoovet, C. Bautista, W. C. Chang, J. R. Ostberg, and M. C. Jensen. 2007. 'Adoptive transfer of chimeric antigen receptor re-directed cytolytic T lymphocyte clones in patients with neuroblastoma', *Mol Ther*, 15: 825-33.

Parkhurst, M. R., J. C. Yang, R. C. Langan, M. E. Dudley, D. A. Nathan, S. A. Feldman, J. L. Davis, R. A. Morgan, M. J. Merino, R. M. Sherry, M. S. Hughes, U. S. Kammula, G. Q. Phan, R. M. Lim, S. A. Wank, N. P. Restifo, P. F. Robbins, C. M. Laurencot, and S. A. Rosenberg. 2011. 'T cells targeting carcinoembryonic antigen can mediate regression of metastatic colorectal cancer but induce severe transient colitis', *Mol Ther*, 19: 620-6.

Paulos, C. M., C. Wrzesinski, A. Kaiser, C. S. Hinrichs, M. Chieppa, L. Cassard, D. C. Palmer, A. Boni, P. Muranski, Z. Yu, L. Gattinoni, P. A. Antony, S. A. Rosenberg, and N. P. Restifo. 2007. 'Microbial translocation augments the function of adoptively transferred self/tumor-specific CD8+ T cells via TLR4 signaling', *J Clin Invest*, 117: 2197-204.

Perez, C., A. Jukica, J. J. Listopad, K. Anders, A. A. Kuhl, C. Loddenkemper, T. Blankenstein, and J. Charo. 2015. 'Permissive expansion and homing of adoptively transferred T cells in tumor-bearing hosts', *Int J Cancer*, 137: 359-71.

Perk, L. R., G. W. Visser, M. J. Vosjan, M. Stigter-van Walsum, B. M. Tijink, C. R. Leemans, and G. A. van Dongen. 2005. '(89)Zr as a PET surrogate radioisotope for scouting biodistribution of the therapeutic radiometals (90)Y and (177)Lu in tumor-bearing nude mice after coupling to the internalizing antibody cetuximab', *J Nucl Med*, 46: 1898-906.

Perk, L. R., M. J. Vosjan, G. W. Visser, M. Budde, P. Jurek, G. E. Kiefer, and G. A. van Dongen. 2010. 'p-Isothiocyanatobenzyl-desferrioxamine: a new bifunctional chelate for facile radiolabeling of monoclonal antibodies with zirconium-89 for immuno-PET imaging', *Eur J Nucl Med Mol Imaging*, 37: 250-9.

Peters, A. M. 1994. 'The utility of [99mTc]HMPAO-leukocytes for imaging infection', *Semin Nucl Med*, 24: 110-27.

Phelps, M. E. 2000. 'Positron emission tomography provides molecular imaging of biological processes', *Proc Natl Acad Sci U S A*, 97: 9226-33.

Pinzon-Charry, A., T. Maxwell, and J. A. Lopez. 2005. 'Dendritic cell dysfunction in cancer: a mechanism for immunosuppression', *Immunol Cell Biol*, 83: 451-61.

Pittet, M. J., J. Grimm, C. R. Berger, T. Tamura, G. Wojtkiewicz, M. Nahrendorf, P. Romero, F. K. Swirski, and R. Weissleder. 2007. 'In vivo imaging of T cell delivery to tumors after adoptive transfer therapy', *Proc Natl Acad Sci U S A*, 104: 12457-61.

Porter, D. L., B. L. Levine, M. Kalos, A. Bagg, and C. H. June. 2011. 'Chimeric antigen receptor-modified T cells in chronic lymphoid leukemia', *N Engl J Med*, 365: 725-33.

Prins, R. M., C. J. Shu, C. G. Radu, D. D. Vo, H. Khan-Farooqi, H. Soto, M. Y. Yang, M. S. Lin, S. Shelly, O. N. Witte, A. Ribas, and L. M. Liau. 2008. 'Anti-tumor activity and trafficking of self, tumor-specific T cells against tumors located in the brain', *Cancer Immunol Immunother*, 57: 1279-89.

Pule, M. A., B. Savoldo, G. D. Myers, C. Rossig, H. V. Russell, G. Dotti, M. H. Huls, E. Liu, A. P. Gee, Z. Mei, E. Yvon, H. L. Weiss, H. Liu, C. M. Rooney, H. E. Heslop, and M. K. Brenner. 2008. 'Virus-specific T cells engineered to coexpress tumor-specific receptors: persistence and antitumor activity in individuals with neuroblastoma', *Nat Med*, 14: 1264-70.

Rabinovich, B. A., Y. Ye, T. Etto, J. Q. Chen, H. I. Levitsky, W. W. Overwijk, L. J. Cooper, J. Gelovani, and P. Hwu. 2008. 'Visualizing fewer than 10 mouse T cells with an enhanced firefly luciferase in immunocompetent mouse models of cancer', *Proc Natl Acad Sci U S A*, 105: 14342-6.

Rabinovich, G. A., D. Gabrilovich, and E. M. Sotomayor. 2007. 'Immunosuppressive strategies that are mediated by tumor cells', *Annu Rev Immunol*, 25: 267-96.

Radu, C. G., C. J. Shu, E. Nair-Gill, S. M. Shelly, J. R. Barrio, N. Satyamurthy, M. E. Phelps, and O. N. Witte. 2008. 'Molecular imaging of lymphoid organs and immune activation by positron emission tomography with a new [18F]-labeled 2'-deoxycytidine analog', *Nat Med*, 14: 783-8.

Radu, C. G., C. J. Shu, S. M. Shelly, M. E. Phelps, and O. N. Witte. 2007. 'Positron emission tomography with computed tomography imaging of neuroinflammation in experimental autoimmune encephalomyelitis', *Proc Natl Acad Sci U S A*, 104: 1937-42.

Rahmim, A., and H. Zaidi. 2008. 'PET versus SPECT: strengths, limitations and challenges', *Nucl Med Commun*, 29: 193-207.

Rapoport, A. P., E. A. Stadtmauer, G. K. Binder-Scholl, O. Goloubeva, D. T. Vogl, S. F. Lacey, A. Z. Badros, A. Garfall, B. Weiss, J. Finklestein, I. Kulikovskaya, S. K. Sinha, S. Kronsberg, M. Gupta, S. Bond, L. Melchiori, J. E. Brewer, A. D. Bennett, A. B. Gerry, N. J. Pumphrey, D. Williams, H. K. Tayton-Martin, L. Ribeiro, T. Holdich, S. Yanovich, N. Hardy, J. Yared, N. Kerr, S. Philip, S. Westphal, D. L. Siegel, B. L. Levine, B. K. Jakobsen, M. Kalos, and C. H. June. 2015. 'NY-ESO-1-specific TCR-engineered T cells mediate sustained antigen-specific antitumor effects in myeloma', *Nat Med*, 21: 914-21.

Reichert, J. M. 2016. 'Antibodies to watch in 2016', *MAbs*, 8: 197-204.

Restifo, N. P., M. E. Dudley, and S. A. Rosenberg. 2012. 'Adoptive immunotherapy for cancer: harnessing the T cell response', *Nat Rev Immunol*, 12: 269-81.

Ribas, A., M. R. Benz, M. S. Allen-Auerbach, C. Radu, B. Chmielowski, E. Seja, J. L. Williams, J. Gomez-Navarro, T. McCarthy, and J. Czernin. 2010. 'Imaging of CTLA4 blockade-induced cell replication with (18)F-FLT PET in patients with advanced melanoma treated with tremelimumab', *J Nucl Med*, 51: 340-6.

Robbins, P. F., M. E. Dudley, J. Wunderlich, M. El-Gamil, Y. F. Li, J. Zhou, J. Huang, D. J. Powell, Jr., and S. A. Rosenberg. 2004. 'Cutting edge: persistence of transferred lymphocyte clonotypes correlates with cancer regression in patients receiving cell transfer therapy', *J Immunol*, 173: 7125-30.

Robbins, P. F., S. H. Kassim, T. L. Tran, J. S. Crystal, R. A. Morgan, S. A. Feldman, J. C. Yang, M. E. Dudley, J. R. Wunderlich, R. M. Sherry, U. S. Kammula, M. S. Hughes, N. P. Restifo, M. Raffeld, C. C. Lee, Y. F. Li, M. El-Gamil, and S. A. Rosenberg. 2015. 'A pilot trial using lymphocytes genetically engineered with an NY-ESO-1-reactive T-cell receptor: long-term follow-up and correlates with response', *Clin Cancer Res*, 21: 1019-27.

Roddie, M. E., A. M. Peters, H. J. Danpure, S. Osman, B. L. Henderson, J. P. Lavender, M. J. Carroll, R. D. Neirinckx, and J. D. Kelly. 1988. 'Inflammation: imaging with Tc-99m HMPAO-labeled leukocytes', *Radiology*, 166: 767-72.

Rogakou, E. P., D. R. Pilch, A. H. Orr, V. S. Ivanova, and W. M. Bonner. 1998. 'DNA double-stranded breaks induce histone H2AX phosphorylation on serine 139', *J Biol Chem*, 273: 5858-68.

Rosenberg, S. A., B. S. Packard, P. M. Aebersold, D. Solomon, S. L. Topalian, S. T. Toy, P. Simon, M. T. Lotze, J. C. Yang, C. A. Seipp, and et al. 1988. 'Use of tumor-infiltrating lymphocytes and interleukin-2 in the immunotherapy of patients with metastatic melanoma. A preliminary report', *N Engl J Med*, 319: 1676-80.

Rosenberg, S. A., and N. P. Restifo. 2015. 'Adoptive cell transfer as personalized immunotherapy for human cancer', *Science*, 348: 62-8.

Rosenberg, S. A., J. C. Yang, R. M. Sherry, U. S. Kammula, M. S. Hughes, G. Q. Phan, D. E. Citrin, N. P. Restifo, P. F. Robbins, J. R. Wunderlich, K. E. Morton, C. M. Laurencot, S. M. Steinberg, D. E. White, and M. E. Dudley. 2011. 'Durable complete responses in heavily pretreated patients with metastatic melanoma using T-cell transfer immunotherapy', *Clin Cancer Res*, 17: 4550-7.

Ruffell, B., A. Au, H. S. Rugo, L. J. Esserman, E. S. Hwang, and L. M. Coussens. 2012. 'Leukocyte composition of human breast cancer', *Proc Natl Acad Sci U S A*, 109: 2796-801.

Sakaguchi, S., N. Sakaguchi, J. Shimizu, S. Yamazaki, T. Sakihama, M. Itoh, Y. Kuniyasu, T. Nomura, M. Toda, and T. Takahashi. 2001. 'Immunologic tolerance maintained by CD25+ CD4+ regulatory T cells: their common role in controlling autoimmunity, tumor immunity, and transplantation tolerance', *Immunol Rev*, 182: 18-32.

Sallusto, F., and A. Lanzavecchia. 2011. 'Memory in disguise', *Nat Med*, 17: 1182-3.

Sato, N., H. Wu, K. O. Asiedu, L. P. Szajek, G. L. Griffiths, and P. L. Choyke. 2015. '(89)Zr-Oxine Complex PET Cell Imaging in Monitoring Cell-based Therapies', *Radiology*, 275: 490-500.

Schmid, T. E., G. Dollinger, W. Beisker, V. Hable, C. Greubel, S. Auer, A. Mittag, A. Tarnok, A. A. Friedl, M. Molls, and B. Roper. 2010. 'Differences in the kinetics of gamma-H2AX fluorescence decay after exposure to low and high LET radiation', *Int J Radiat Biol*, 86: 682-91.

Schmitt, T. M., G. B. Ragnarsson, and P. D. Greenberg. 2009. 'T cell receptor gene therapy for cancer', *Hum Gene Ther*, 20: 1240-8.

Scholten, K. B., D. Kramer, E. W. Kueter, M. Graf, T. Schoedl, C. J. Meijer, M. W. Schreurs, and E. Hooijberg. 2006. 'Codon modification of T cell receptors allows enhanced functional expression in transgenic human T cells', *Clin Immunol*, 119: 135-45.

Schreiber, R. D., L. J. Old, and M. J. Smyth. 2011. 'Cancer immunoediting: integrating immunity's roles in cancer suppression and promotion', *Science*, 331: 1565-70.

Serdons, K., A. Verbruggen, and G. M. Bormans. 2009. 'Developing new molecular imaging probes for PET', *Methods*, 48: 104-11.

Shu, C. J., C. G. Radu, S. M. Shelly, D. D. Vo, R. Prins, A. Ribas, M. E. Phelps, and O. N. Witte. 2009. 'Quantitative PET reporter gene imaging of CD8+ T cells specific for a melanoma-expressed self-antigen', *Int Immunol*, 21: 155-65.

Sommermeyer, D., J. Neudorfer, M. Weinhold, M. Leisegang, B. Engels, E. Noessner, M. H. Heemskerk, J. Charo, D. J. Schendel, T. Blankenstein, H. Bernhard, and W. Uckert. 2006. 'Designer T cells by T cell receptor replacement', *Eur J Immunol*, 36: 3052-9.

Sommermeyer, D., and W. Uckert. 2010. 'Minimal amino acid exchange in human TCR constant regions fosters improved function of TCR gene-modified T cells', *J Immunol*, 184: 6223-31.

Steward, B. W., Wild,C.P. . 2014. *World Cancer Report 2014.*

Su, H., A. Forbes, S. S. Gambhir, and J. Braun. 2004. 'Quantitation of cell number by a positron emission tomography reporter gene strategy', *Mol Imaging Biol*, 6: 139-48.

Summer, D., J. Garousi, M. Oroujeni, B. Mitran, K. G. Andersson, A. Vorobyeva, J. Lofblom, A. Orlova, V. Tolmachev, and C. Decristoforo. 2017. 'Cyclic versus Noncyclic Chelating Scaffold for (89)Zr-Labeled ZEGFR:2377 Affibody Bioconjugates Targeting Epidermal Growth Factor Receptor Overexpression', *Mol Pharm*.

Tavare, R., H. Escuin-Ordinas, S. Mok, M. N. McCracken, K. A. Zettlitz, F. B. Salazar, O. N. Witte, A. Ribas, and A. M. Wu. 2016. 'An Effective Immuno-PET Imaging Method to Monitor CD8-Dependent Responses to Immunotherapy', *Cancer Res*, 76: 73-82.

Tavare, R., M. N. McCracken, K. A. Zettlitz, S. M. Knowles, F. B. Salazar, T. Olafsen, O. N. Witte, and A. M. Wu. 2014. 'Engineered antibody fragments for immuno-PET imaging of endogenous CD8+ T cells in vivo', *Proc Natl Acad Sci U S A*, 111: 1108-13.

Tavare, R., M. N. McCracken, K. A. Zettlitz, F. B. Salazar, T. Olafsen, O. N. Witte, and A. M. Wu. 2015. 'Immuno-PET of Murine T Cell Reconstitution Postadoptive Stem Cell Transplantation Using Anti-CD4 and Anti-CD8 Cys-Diabodies', *J Nucl Med*, 56: 1258-64.

Tawara, I., S. Kageyama, Y. Miyahara, H. Fujiwara, T. Nishida, Y. Akatsuka, H. Ikeda, K. Tanimoto, S. Terakura, M. Murata, Y. Inaguma, M. Masuya, N. Inoue, T. Kidokoro, S. Okamoto, D. Tomura, H. Chono, I. Nukaya, J. Mineno, T. Naoe, N. Emi, M. Yasukawa, N. Katayama, and H. Shiku. 2017. 'Safety and persistence of WT1-specific T-cell receptor gene-transduced lymphocytes in patients with AML and MDS', *Blood*.

Teachey, D. T., S. F. Lacey, P. A. Shaw, J. J. Melenhorst, S. L. Maude, N. Frey, E. Pequignot, V. E. Gonzalez, F. Chen, J. Finklestein, D. M. Barrett, S. L. Weiss, J. C. Fitzgerald, R. A. Berg, R. Aplenc, C. Callahan, S. R. Rheingold, Z. Zheng, S. Rose-John, J. C. White, F. Nazimuddin, G. Wertheim, B. L. Levine, C. H. June, D. L. Porter, and S. A. Grupp. 2016. 'Identification of Predictive Biomarkers for Cytokine Release Syndrome after Chimeric Antigen Receptor T-cell Therapy for Acute Lymphoblastic Leukemia', *Cancer Discov*, 6: 664-79.

Teachey, D. T., S. R. Rheingold, S. L. Maude, G. Zugmaier, D. M. Barrett, A. E. Seif, K. E. Nichols, E. K. Suppa, M. Kalos, R. A. Berg, J. C. Fitzgerald, R. Aplenc, L. Gore, and S. A. Grupp. 2013. 'Cytokine release syndrome after blinatumomab treatment related to abnormal macrophage activation and ameliorated with cytokine-directed therapy', *Blood*, 121: 5154-7.

Thomas, L. 1982. 'On immunosurveillance in human cancer', *Yale J Biol Med*, 55: 329-33.

Thomas, S., S. A. Xue, M. Cesco-Gaspere, E. San Jose, D. P. Hart, V. Wong, R. Debets, B. Alarcon, E. Morris, and H. J. Stauss. 2007. 'Targeting the Wilms tumor antigen 1 by TCR gene transfer: TCR variants improve tetramer binding but not the function of gene modified human T cells', *J Immunol*, 179: 5803-10.

Thu, M. S., L. H. Bryant, T. Coppola, E. K. Jordan, M. D. Budde, B. K. Lewis, A. Chaudhry, J. Ren, N. R. Varma, A. S. Arbab, and J. A. Frank. 2012. 'Self-assembling nanocomplexes by combining ferumoxytol, heparin and protamine for cell tracking by magnetic resonance imaging', *Nat Med*, 18: 463-7.

Toy, G., W. R. Austin, H. I. Liao, D. Cheng, A. Singh, D. O. Campbell, T. O. Ishikawa, L. W. Lehmann, N. Satyamurthy, M. E. Phelps, H. R. Herschman, J. Czernin, O. N. Witte, and C. G. Radu. 2010. 'Requirement for deoxycytidine kinase in T and B lymphocyte development', *Proc Natl Acad Sci U S A*, 107: 5551-6.

Traversari, C., S. Marktel, Z. Magnani, P. Mangia, V. Russo, F. Ciceri, C. Bonini, and C. Bordignon. 2007. 'The potential immunogenicity of the TK suicide gene does not prevent full clinical benefit associated with the use of TK-transduced donor lymphocytes in HSCT for hematologic malignancies', *Blood*, 109: 4708-15.

Ulaner, G. A., S. K. Lyashchenko, C. Riedl, S. Ruan, P. B. Zanzonico, D. Lake, K. Jhaveri, B. Zeglis, J. S. Lewis, and J. A. O'Donoghue. 2017. 'First-in-human HER2-targeted imaging using (89)Zr-pertuzumab PET/CT: Dosimetry and clinical application in patients with breast cancer', *J Nucl Med*.

USFDA. 2005. 'Guidance for Industry: Estimating the Maximum Safe Starting Dose in Adult Healthy Volunteer', *Rockville, MD: US Food and Drug Administration*.

Uttenthal, B. J., I. Chua, E. C. Morris, and H. J. Stauss. 2012. 'Challenges in T cell receptor gene therapy', *J Gene Med*, 14: 386-99.

van de Watering, F. C., M. Rijpkema, L. Perk, U. Brinkmann, W. J. Oyen, and O. C. Boerman. 2014. 'Zirconium-89 labeled antibodies: a new tool for molecular imaging in cancer patients', *Biomed Res Int*, 2014: 203601.

van Dongen, G. A., G. W. Visser, M. N. Lub-de Hooge, E. G. de Vries, and L. R. Perk. 2007. 'Immuno-PET: a navigator in monoclonal antibody development and applications', *Oncologist*, 12: 1379-89.

van Dongen, G. A., and M. J. Vosjan. 2010. 'Immuno-positron emission tomography: shedding light on clinical antibody therapy', *Cancer Biother Radiopharm*, 25: 375-85.

Vatakis, D. N., R. C. Koya, C. C. Nixon, L. Wei, S. G. Kim, P. Avancena, G. Bristol, D. Baltimore, D. B. Kohn, A. Ribas, C. G. Radu, Z. Galic, and J. A. Zack. 2011. 'Antitumor activity from antigen-specific CD8 T cells generated in vivo from genetically engineered human hematopoietic stem cells', *Proc Natl Acad Sci U S A*, 108: E1408-16.

Visser, E. P., J. A. Disselhorst, M. Brom, P. Laverman, M. Gotthardt, W. J. Oyen, and O. C. Boerman. 2009. 'Spatial resolution and sensitivity of the Inveon small-animal PET scanner', *J Nucl Med*, 50: 139-47.

Vosjan, M. J., L. R. Perk, G. W. Visser, M. Budde, P. Jurek, G. E. Kiefer, and G. A. van Dongen. 2010. 'Conjugation and radiolabeling of monoclonal antibodies with zirconium-89 for PET imaging using the bifunctional chelate p-isothiocyanatobenzyl-desferrioxamine', *Nat Protoc*, 5: 739-43.

Voss, R. H., J. Kuball, R. Engel, P. Guillaume, P. Romero, C. Huber, and M. Theobald. 2006. 'Redirection of T cells by delivering a transgenic mouse-derived MDM2 tumor antigen-specific TCR and its humanized derivative is governed by the CD8 coreceptor and affects natural human TCR expression', *Immunol Res*, 34: 67-87.

Vugts, D. J., C. Klaver, C. Sewing, A. J. Poot, K. Adamzek, S. Huegli, C. Mari, G. W. Visser, I. E. Valverde, G. Gasser, T. L. Mindt, and G. A. van Dongen. 2017. 'Comparison of the octadentate bifunctional chelator DFO*-pPhe-NCS and the clinically used hexadentate bifunctional chelator DFO-pPhe-NCS for (89)Zr-immuno-PET', *Eur J Nucl Med Mol Imaging*, 44: 286-95.

Vugts, D. J., and G. A. van Dongen. 2011. '(89)Zr-labeled compounds for PET imaging guided personalized therapy', *Drug Discov Today Technol*, 8: e53-61.

Wagner, M., U. Seitz, A. Buck, B. Neumaier, S. Schultheiss, M. Bangerter, M. Bommer, F. Leithauser, E. Wawra, G. Munzert, and S. N. Reske. 2003. '3'-[18F]fluoro-3'-deoxythymidine ([18F]-FLT) as positron emission tomography tracer for imaging

proliferation in a murine B-Cell lymphoma model and in the human disease', *Cancer Res*, 63: 2681-7.

Wang, X., C. Berger, C. W. Wong, S. J. Forman, S. R. Riddell, and M. C. Jensen. 2011. 'Engraftment of human central memory-derived effector CD8+ T cells in immunodeficient mice', *Blood*, 117: 1888-98.

Whittenberg, J. J., H. Li, H. Zhou, J. Koziol, A. V. Desai, D. E. Reichert, and P. J. A. Kenis. 2017. '"Click Chip" Conjugation of Bifunctional Chelators to Biomolecules', *Bioconjug Chem*, 28: 986-94.

Wolchok, J. D., A. Hoos, S. O'Day, J. S. Weber, O. Hamid, C. Lebbe, M. Maio, M. Binder, O. Bohnsack, G. Nichol, R. Humphrey, and F. S. Hodi. 2009. 'Guidelines for the evaluation of immune therapy activity in solid tumors: immune-related response criteria', *Clin Cancer Res*, 15: 7412-20.

Wu, A. M. 2014. 'Engineered antibodies for molecular imaging of cancer', *Methods*, 65: 139-47.

Yaghoubi, S. S., M. C. Jensen, N. Satyamurthy, S. Budhiraja, D. Paik, J. Czernin, and S. S. Gambhir. 2009. 'Noninvasive detection of therapeutic cytolytic T cells with 18F-FHBG PET in a patient with glioma', *Nat Clin Pract Oncol*, 6: 53-8.

Zeng, D., B. M. Zeglis, J. S. Lewis, and C. J. Anderson. 2013. 'The growing impact of bioorthogonal click chemistry on the development of radiopharmaceuticals', *J Nucl Med*, 54: 829-32.

8 ABBREVIATIONS

%ID	Percent injected dose
%ID/g	Percent injected dose per gram
^{111}In	Indium-111
^{124}I	Iodine-124
^{18}F	Fluor-18
^{64}Cu	Copper-64
^{68}Ga	Gallium-68
^{89}Zr	Zirconium-89
^{99m}Tc	Technetium-99m
AML	Acute myeloid leukemia
aTCRmu	Anti-murine TCR antibody
BLI	Bioluminescence imaging
CAIX	Carboxy-anhydrase-IX
CAR	Chimeric antigen receptors
CD	Cluster of differentiation
CEA	Carcinoembryonic antigen
CLIO-HD	Highly derivatized cross-linked iron oxide nanoparticle
cOVA	cloned chicken ovalbumin cells
CPM	Counts per minute
CRS	Cytokine release syndrome
CT	X-ray computed tomography
CTLA-4	Cytotoxic T-lymphocyte antigen-4
Da	Dalton
Db	Diabody
DBN	Desferrioxamine-NCS
DC	Dendritic cell
dCK	Deoxycytidine kinase
DFO*	Extended DFO derivate
DFO-Bz-NCS	p-isothiocanatobenzyl derivate of desferrioxamine
DFO-Sq	squaramide ester derivative of DFO
DNA	Deoxyribonucleic acid
DOTA	1,4,7,10-tetraazacyclododecane-1,4,7,10-tetraacetic acid
DSB	Double-strand break
DTPA	Diethylenetriaminepentaacetic acid

EBV	Epstein-Barr virus
EGFR	Epithelial growth factor receptor
EGFR	Epidermal growth factor receptor
ELISA	Enzyme linked immunosorbent Assay
FAC	1-(2'-deoxy-2'-fluoroarabinofuranosyl)cytosine
FBEM	4-fluorobenzamido-N-ethylamino-maleimide
FcR	Fc-Receptor
FDA	Food and Drug administration USA
FDG	Fludeoxyglucose
FLI	Fluorescence imaging
FLT	3'-Deoxy-3'-fluorothymidine
GFP	Green fluorescent protein
gp100	Glycoprotein 100
hdCK3mut	human deoxycytidine kinase triple mutant
HED	Human equivalent dose
hIL	Human interleukin
HLA	Human leukocyte antigen
HMPAO	hexamethylpropyleneamine oxime
hNET	human norepinephrine transporter
hNIS	human sodium iodide transporter
HOPO	3,4,3-(LI-1,2-HOPO) derivate of DFO
HPLC	High performace liquid chromatography
HRP	horseradish peroxidase
HSC	hematopoietic stem cells
HSV1-tk	herpes simplex virus1-thymidine kinase
i.t.	Intratumoral
i.v.	Intravenous
IFN-γ	Interferon gamma
IgG	Immunoglobuline G
IHC	Immunohistochemistry
iRFP	near-infrared fluorescent protein
ITLC	Instant thin layer chromatography
K_d	Dissociation constant
kDa	Kilodalton
mAb	Monoclonal antibody
MAGE-A3	Melanoma associated antigen A3

MART-1	Melanoma antigen recognized by T cells 1
MAS	Macrophage activation syndrome
Mb	Minibody
MDSC	Myeloid-derived suppressor cells
MFI	Mean fluorescence intensity
MHC	Major histocompatibility complex
MIP	Maximal intensity projection
MPO	Myeloperoxidase
MRI	Magnetic resonance imaging
NK	Natural killer cells
NOTA	1,4,7-triazacyclononane-triacetic acid
NY-ESO1	New York esophageal squamous cell carcinoma-1
p.i.	Post injection
PBMC	Peripheral blood mononuclear cells
PBMC	Peripheral blood mononuclear cells
PD-1	Programmed cell death 1 protein
PD-L1	Programmed cell death 1 protein ligand
PET	Positron emission tomography
PFC	Perfluorocarbon
PSMA	Human prostate specific membrane antigen
PTSM	Pyruvaldehyde- bis(N(4)-methylthiosemicarbazone
qPCR	Real-time quantitative polymerase chain reaction
RCP	Radiochemical purity
R_f	Retardation factor
RIT	Radioimmunotherapy
ROI	Region of interest
s.c.	Subcutaneous
scFv	single-chain variable fragment
SD	Standard deviation
SPECT	Single photon emission computed tomography
SPION	Superparamagnetic iron oxide nanoparticle
TBI	Total body irradiation
T_{CM}	Central memory T cells
TCR	T-cell receptor
T_{EM}	Effector memory T cells
TGF-β	Transforming growth factor beta

Th1	Type 1 T helper cells
TIL	Tumor infiltrating lymphocytes
T_N	Naïve T cells
T_{reg}	Regulatory T cells
T_{SCM}	T memory stem cells
WC	Working concentration
WHO	World health organization
WT	Wild type

9 PUBLICATIONS

Key Features Relevant to Select Antigens and TCR from the MHC-Mismatched Repertoire to Treat Cancer.
Audehm S, Glaser M, Pecoraro M, Bräunlein E, Mall S, Klar R, Effenberger M, Albers J, Bianchi HO, Peper Ja, **Yusufi N**, Busch DH, Stevanović S, Mann M, Antes I, Krackhardt AM. *Front. Immunol.*, 2019 Jun 28;10:1485. doi: 10.3389/fimmu.2019.01485.

T-cell functionality testing is highly relevant to developing novel immuno-tracers monitoring T cells in the context of immunotherapies and revealed CD7 as an attractive target.
Mayer KE, Mall S, **Yusufi N**, Gosmann D, Steiger K, Russelli L, Bianchi HO, Audehm S, Wagner R, Bräunlein E, Stelzl A, Bassermann F, Weichert W, Weber W, Schwaiger M, D'Alessandria C, Krackhardt AM.
Theranostics. 2018 Nov 28;8(21):6070-6087. doi: 10.7150/thno.27275. eCollection 2018.

In-depth Characterization of a TCR-specific Tracer for Sensitive Detection of Tumor-directed Transgenic T Cells by Immuno-PET.
Yusufi N, Mall S, Bianchi HO, Steiger K, Reder S, Klar R, Audehm S, Mustafa M, Nekolla S, Peschel C, Schwaiger M, Krackhardt AM, D'Alessandria C.
Theranostics. 2017 Jun 15;7(9):2402-2416. doi: 10.7150/thno.17994. eCollection 2017.

Immuno-PET Imaging of Engineered Human T Cells in Tumors.
Mall S, **Yusufi N**, Wagner R, Klar R, Bianchi H, Steiger K, Straub M, Audehm S, Laitinen I, Aichler M, Peschel C, Ziegler S, Mustafa M, Schwaiger M, D'Alessandria C, Krackhardt AM. *Cancer Res.* 2016 Jul 15;76(14):4113-23. doi: 10.1158/0008-5472.CAN-15-2784. Epub 2016 Jun 28.

10 ACKNOWLEDGEMENTS

Foremost, I would like to thank Prof. Dr. Markus Schwaiger for giving me the opportunity to do my doctorate at the Department of Nuclear Medicine within the SFB824 network and for the supervision and support during my PhD. Further, I would like to thank Dr. Calogero D'Alessandria, Prof. Dr. Angela Krackhardt and Prof. Dr. Markus Essler for providing me this interesting research project and their guidance throughout my work. I want to thank Prof. Dr. Gabrielle Multhoff for being in my thesis committee and her availability for inquiries.

Many thanks to Dr. Sabine Mall for introducing me in my work and the close co-working in all the animal experiments.

Thanks also to the members of Krackhardt's lab sharing the lab space and providing me technical support for my experiments: Henrique Bianchi, Dr. Stefan Audehm, Dr. Richard Klar for helping me out in my *in vivo* studies; Eva Bräunlein and Ricarda Wagner for blood drawings for the T-cell isolations. Many thanks also to Stephanie Rämisch and Irina Fuchs for supporting me in the lab.

I am grateful for the contributions to the IHC analyses done by Dr. Katja Steiger and her group as well as for the excellent work in performing PET/CT scans by Sybille Reder, Markus Mittelhäuser and Marco Lehmann.

Many thanks to Birgit Blechert and Michael Michalik for organizational and technical support in the labs of the Nuclear Medicine as well as to Dr. Christof Seidl for his experimental advice and giving me the opportunity to participate in the German-Australian Network on Personalized Cancer Medicine.

For making my days bright and cheerful, I am happy I shared my office space with Dr. Hans-Richard Demel, Dr. Kim Muñoz-Álvarez, Eugen Kuballa, Dr. Andreas Poschenrieder and the "think tank" Dr. Christian Hundshammer, Dr. Stephan Düwel and Dr. Zoreh Varasteh.

Finally, I would like to express my most profound gratitude to my beloved family and friends for their encouragement and care for me over the course of these years. ⌛